

PhD Thesis



# PhD Thesis

## this is a subtitle

by Oliver Matonoha



LUND  
UNIVERSITY

Thesis for the degree of Doctorate  
Thesis advisors: Prof. Doktor Professorsson, Prof. Knirk Gnork  
Faculty opponent: Prof. Gammal och Grå

To be presented, with the permission of the Faculty of Natural Sciences of Lund University, for public criticism at LINXS (Delta 5, floor 5, IDEON building) on friday, the 30th of October 2023 at 10:15.

Organization <b>LUND UNIVERSITY</b>	Document name <b>LICENTIATE THESIS</b>	
Department of Physics Box 124 SE-221 00 LUND Sweden	Date of disputation <b>2020-10-30</b>	
Author(s) Oliver Matonoha	Sponsoring organization	
Title and subtitle PhD Thesis this is a subtitle		
<b>Abstract</b> <p> Lorem ipsum dolor sit amet, consectetur adipiscing elit. Etiam lobortis facilisis sem. Nullam nec mi et neque pharetra sollicitudin. Praesent imperdiet mi nec ante. Donec ullamcorper, felis non sodales commodo, lectus velit ultrices augue, a dignissim nibh lectus placerat pede. Vivamus nunc nunc, molestie ut, ultricies vel, semper in, velit. Ut porttitor. Praesent in sapien. Lorem ipsum dolor sit amet, consectetur adipiscing elit. Duis fringilla tristique neque. Sed interdum libero ut metus. Pellentesque placerat. Nam rutrum augue a leo. Morbi sed elit sit amet ante lobortis sollicitudin. Praesent blandit blandit mauris. Praesent lectus tellus, aliquet aliquam, luctus a, egestas a, turpis. Mauris lacinia lorem sit amet ipsum. Nunc quis urna dictum turpis accumsan semper.</p>		
Key words quantum chromodynamics, quark-gluon plasma		
Classification system and/or index terms (if any)		
Supplementary bibliographical information	Language <b>English</b>	
ISSN and key title	ISBN <b>123456789 (print)</b> <b>123456789 (pdf)</b>	
Recipient's notes	Number of pages <b>153</b>	Price
	Security classification	

I, the undersigned, being the copyright owner of the abstract of the above-mentioned dissertation, hereby grant to all reference sources the permission to publish and disseminate the abstract of the above-mentioned dissertation.

Signature \_\_\_\_\_

Date **2020-09-18**

# PhD Thesis

this is a subtitle

by Oliver Matonoha



LUND  
UNIVERSITY

A licentiate thesis at a university in Sweden takes either the form of a single, cohesive research study (monograph) or a summary of research papers (compilation thesis), which the licentiate student has written alone or together with one or several other author(s).

In the latter case the thesis consists of two parts. An introductory text puts the research work into context and summarizes the main points of the papers. Then, the research publications themselves are reproduced, together with a description of the individual contributions of the authors. The research papers may either have been already published or are manuscripts at various stages (in press, submitted, or in draft).

**Cover illustration front:** Cool figure by bla and bla.

**Cover illustration back:** Another cool image by bla.

**Funding information:** The thesis work was financially supported by the Swedish Research Council.

© Oliver Matonoha 2023

Faculty of Natural Sciences, Department of Physics

ISBN: 123456789 (print)

ISBN: 123456789 (pdf)

Printed in Sweden by Media-Tryck, Lund University, Lund 2023



Media-Tryck is a Nordic Swan Ecolabel certified provider of printed material.  
Read more about our environmental work at [www.mediathyck.lu.se](http://www.mediathyck.lu.se)

MADE IN SWEDEN

*Dedicated to  
Humpty – Dumpty  
bla bla blat*



# Contents

List of publications . . . . .	v
Acknowledgements . . . . .	vi
Populärvetenskaplig sammanfattning på svenska . . . . .	vii
PhD Thesis this is a subtitle	i
<b>I Fundamental theory</b>	<b>3</b>
<b>1 Introduction to quantum chromodynamics</b>	<b>5</b>
1.1 Standard Model of elementary particles . . . . .	5
1.1.1 Quantum Electrodynamics . . . . .	7
1.2 Coordinate systems and kinematic observables . . . . .	7
1.3 Processes involving gluons . . . . .	8
1.3.1 Running coupling constant . . . . .	8
1.3.2 Perturbative QCD . . . . .	8
1.4 From partons to hadrons . . . . .	8
1.4.1 Initial and Final State Radiation . . . . .	8
1.4.2 Factorisation theorem . . . . .	9
1.4.3 Parton distribution functions . . . . .	10
1.4.4 Parton fragmentation and the Lund string . . . . .	11
1.5 Multiple partonic interactions . . . . .	13
1.5.1 Color reconnection . . . . .	15
1.6 Underlying event . . . . .	16
1.7 Lattice QCD . . . . .	16
1.8 QCD phase diagram . . . . .	17
1.8.1 Phase transition . . . . .	17
1.8.2 Chiral symmetry restoration . . . . .	17
1.9 Implications of high-activity QCD research . . . . .	17
<b>2 QCD phenomena in high energy hadronic collisions</b>	<b>19</b>
2.1 Collisions of heavy nuclei . . . . .	19
2.1.1 Collision geometry, Centrality, multiplicity . . . . .	19
2.1.2 MC Glauber model . . . . .	21

2.2	Quark-gluon plasma . . . . .	22
2.2.1	Quarkonium dissociation and sequential suppression . . . . .	24
2.2.2	Strangeness enhancement . . . . .	25
2.2.3	Collective flow . . . . .	26
2.2.4	Jet quenching . . . . .	26
2.2.5	Cold nuclear matter effects . . . . .	27
2.3	QGP phenomena in small systems . . . . .	27
	Strangeness and charm enhancement . . . . .	27
	Anisotropic flow . . . . .	28
	Radial flow . . . . .	29
	Sequential suppression of $\Upsilon$ states . . . . .	30
	Other QGP signatures . . . . .	31
2.3.1	Role of multiplicity . . . . .	31
2.4	Phenomenological models . . . . .	32
2.4.1	Pythia . . . . .	32
	String interactions and Ropes . . . . .	33
2.4.2	Epos LHC . . . . .	33
<b>II</b>	<b>Experimental Setup and Methodology</b>	<b>35</b>
<b>3</b>	<b>Large Hadron Collider</b>	<b>37</b>
3.1	European Organisation for Nuclear Research . . . . .	37
3.2	Large Hadron Collider (LHC) . . . . .	37
<b>4</b>	<b>The ALICE Detector</b>	<b>41</b>
<b>5</b>	<b>Events, Vertices, Tracks, and Particles</b>	<b>43</b>
<b>III</b>	<b>Author's measurements</b>	<b>45</b>
<b>6</b>	<b>Reconstruction of neutral strange particles with ALICE</b>	<b>47</b>
6.1	Analysed datasets . . . . .	47
6.2	Identification of $V^0$ 's using ALICE . . . . .	48
6.3	Signal extraction . . . . .	48
6.3.1	Validation using simulations . . . . .	50
6.4	Normalisation . . . . .	51
6.5	Corrections to the reconstructed production . . . . .	52
6.5.1	Secondary contribution correction . . . . .	52
6.5.2	Reconstruction efficiency . . . . .	54
6.6	Transverse momentum spectra . . . . .	55
6.6.1	Comparisons with previously published results . . . . .	55
6.7	Systematic uncertainties . . . . .	56
6.7.1	Variation of selection criteria . . . . .	58

6.7.2	Feeddown correction . . . . .	59
<b>7</b>	<b>Transverse Spherocity</b>	<b>63</b>
7.1	Transverse spherocity . . . . .	63
7.1.1	Motivation for studying event topology . . . . .	63
7.1.2	$S_O$ and $S_O^{(p_T=1.0)}$ as experimental observables . . . . .	64
7.1.3	Relationship between $S_O^{(p_T=1.0)}$ and $S_O$ . . . . .	67
7.1.4	Track and event selection . . . . .	67
7.1.5	Multiplicity selection and its interplay with $S_O^{(p_T=1.0)}$ . . . . .	68
7.1.6	Comparison of $V^0$ production with MC generators . . . . .	72
7.2	Systematic uncertainties . . . . .	72
7.2.1	Variations in alternative methods . . . . .	72
7.2.2	Experimental bias . . . . .	74
7.2.3	Correlation of uncertainties with $S_O^{(p_T=1.0)}$ . . . . .	74
7.2.4	Summary . . . . .	75
7.3	Transverse momentum spectra vs. $S_O^{(p_T=1.0)}$ . . . . .	77
7.3.1	Ratios of neutral kaons to charged kaons . . . . .	78
7.4	Mean transverse momenta and integrated yields . . . . .	79
7.5	Ratios to pions . . . . .	81
7.6	Baryon-to-meson ratio . . . . .	81
7.7	Ratio of integrated yields vs. $S_O^{(p_T=1.0)}$ . . . . .	82
<b>8</b>	<b>Underlying Event Activity</b>	<b>85</b>
8.1	Motivation for studying event sub-structure . . . . .	85
8.1.1	Underlying event . . . . .	85
8.1.2	Hard process–multiplicity bias . . . . .	85
8.1.3	Azimuthal regions and transverse activity . . . . .	86
8.2	$R_T$ as an experimental observable . . . . .	87
8.2.1	Proxy to $n_{\text{MPI}}$ . . . . .	88
8.2.2	Extension to $R_{T,\min}$ , $R_{T,\max}$ . . . . .	88
	Charged particle $p_T$ spectra . . . . .	89
8.2.3	Track and event selection . . . . .	89
8.2.4	$R_T$ measurements of neutral particles vs. charged particles .	91
8.3	Bayesian unfolding procedure . . . . .	92
8.3.1	One-dimensional unfolding . . . . .	92
8.3.2	Propagation of statistical uncertainties . . . . .	96
8.3.3	Unfolding of $K_S^0$ , $\Lambda$ , and $\bar{\Lambda}$ $p_T$ spectra . . . . .	96
8.4	$R_T$ , $R_{T,\min}$ , $R_{T,\max}$ distributions . . . . .	99
8.5	Systematic uncertainties . . . . .	100
8.5.1	Uncertainties from the unfolding procedure . . . . .	103
8.5.2	Uncorrelated uncertainties . . . . .	104

8.6	Description of regions and mean transverse momentum . . . . .	104
8.7	Transverse momentum spectra . . . . .	107
8.8	Baryon-to-meson ratio . . . . .	112
8.9	Integrated yields . . . . .	115
<b>9</b>	<b>Discussion of Results and Conclusions</b>	<b>117</b>
<b>IV</b>	<b>Appendices</b>	<b>119</b>
<b>A</b>	<b>List of Acronyms</b>	<b>121</b>
<b>B</b>	<b>Mathematical Derivations</b>	<b>123</b>
<b>C</b>	<b>Complementary Material</b>	<b>125</b>
<b>D</b>	<b>Scientific Publications</b>	<b>127</b>
	Author contributions . . . . .	127
	Paper I: Title paper 1 . . . . .	127
	Paper II: Title paper 2 . . . . .	127
	Paper I: Title paper 1 . . . . .	129
	Paper II: Title paper 2 . . . . .	133
	<b>References</b>	<b>137</b>

## List of publications

This thesis is based on the following publications, referred to by their Roman numerals:

I    Title paper 1

S. Doctor, B. Someone

*The Journal of Physical Chemistry A*, 2020, 124(19), pp. 3943-3946

II    Title paper 2

S. Doctor, B. Someone, C Another

*Physical Chemistry Chemical Physics*, 2020, 22(24), pp. 13659-13665

All papers are reproduced with permission of their respective publishers.

## Acknowledgements

Lorem ipsum dolor sit amet, consectetuer adipiscing elit. Etiam lobortis facilisis sem. Nullam nec mi et neque pharetra sollicitudin. Praesent imperdiet mi nec ante. Donec ullamcorper, felis non sodales commodo, lectus velit ultrices augue, a dignissim nibh lectus placerat pede. Vivamus nunc nunc, molestie ut, ultricies vel, semper in, velit. Ut porttitor. Praesent in sapien. Lorem ipsum dolor sit amet, consectetuer adipiscing elit. Duis fringilla tristique neque. Sed interdum libero ut metus. Pellentesque placerat. Nam rutrum augue a leo. Morbi sed elit sit amet ante lobortis sollicitudin. Praesent blandit blandit mauris. Praesent lectus tellus, aliquet aliquam, luctus a, egestas a, turpis. Mauris lacinia lorem sit amet ipsum. Nunc quis urna dictum turpis accumsan semper.

## **Populärvetenskaplig sammanfattning på svenska**

Lore ipsum dolor sit amet, consectetuer adipiscing elit. Etiam lobortis facilisis sem. Nullam nec mi et neque pharetra sollicitudin. Praesent imperdiet mi nec ante. Donec ullamcorper, felis non sodales commodo, lectus velit ultrices augue, a dignissim nibh lectus placerat pede. Vivamus nunc nunc, molestie ut, ultricies vel, semper in, velit. Ut porttitor. Praesent in sapien. Lore ipsum dolor sit amet, consectetuer adipiscing elit. Duis fringilla tristique neque. Sed interdum libero ut metus. Pellentesque place-  
rat. Nam rutrum augue a leo. Morbi sed elit sit amet ante lobortis sollicitudin. Prae-  
sent blandit blandit mauris. Praesent lectus tellus, aliquet aliquam, luctus a, egestas a,  
turpis. Mauris lacinia lorem sit amet ipsum. Nunc quis urna dictum turpis accumsan  
semper.



# PhD Thesis this is a subtitle



# Part I

# Fundamental theory



# Chapter I

## Introduction to quantum chromodynamics

This chapter serves as an introduction to particle physics, QCD, and phenomenology of high energy QCD interactions, with the focus on multiple partonic interactions and string formations.

### I.1 Standard Model of elementary particles

One paragraph QFT

One paragraph description

One paragraph successes and drawbacks

## Quarks

$2.2^{+0.5}_{-0.4} \text{ MeV}$	$1.28 \pm 0.03 \text{ GeV}/c^2$	$172.76 \text{ GeV}/c^2$
<b>u</b> <i>up</i> $+\frac{2}{3}e$	<b>c</b> <i>charm</i> $+\frac{2}{3}e$	<b>t</b> <i>top</i> $+\frac{2}{3}e$
1964 - GIM mechanism	1974 - $J/\psi$ meson	1995 - Tevatron
$4.7^{+0.5}_{-0.4} \text{ MeV}/c^2$	$4.7^{+0.5}_{-0.4} \text{ MeV}/c^2$	$4.7^{+0.5}_{-0.4} \text{ MeV}/c^2$
<b>d</b> <i>down</i> $-\frac{1}{3}e$	<b>s</b> <i>strange</i> $-\frac{1}{3}e$	<b>b</b> <i>bottom</i> $-\frac{1}{3}e$
1964 - GIM mechanism	1964 - kaon decay	1977 - Upsilon meson

## Leptons

$0.511 \text{ MeV}/c^2$	$105.66 \text{ MeV}/c^2$	$1.77686 \text{ GeV}/c^2$
<b>e</b> <i>electron</i> $-1e$	<b><math>\mu</math></b> <i>muon</i> $-1e$	<b><math>\tau</math></b> <i>tau</i> $-1e$
1895 - X-rays	1936 - cosmic ray	1975 - SLAC
$< 2.2 \text{ eV}/c^2$	$< 0.17 \text{ MeV}/c^2$	$< 18.2 \text{ MeV}/c^2$
<b><math>\nu_e</math></b> <i>electron neutrino</i> 0	<b><math>\nu_\mu</math></b> <i>muon neutrino</i> 0	<b><math>\nu_\tau</math></b> <i>tau neutrino</i> 0
1956 - nuclear reactor	1962 - Brookhaven	2000 - Fermilab

## Gauge Bosons

$0$	$0$	$80.379 \text{ GeV}/c^2$
<b><math>\gamma</math></b> <i>photon</i> 0	<b>g</b> <i>gluon</i> 0	<b>W</b> $W^\pm$ $\pm 1e$
1900 - Max Planck's quanta	1979 - PETRA	1983 - UA1, UA2
$91.1876 \text{ GeV}/c^2$	$125.10 \text{ GeV}/c^2$	
<b>Z</b> $Z^0$ 0	<b>H</b> <i>Higgs</i> 0	2012 - ATLAS, CMS
1983 - UA1, UA2		

Figure 1.1: Standard model. VALUES NEED TO BE FIXED.

### 1.1.1 Quantum Electrodynamics

One paragraph

## 1.2 Coordinate systems and kinematic observables

Particles in HEP processes are described by their Lorentz-invariant four-vectors,  $\mathbf{x} = (ct, x, y, z)$  and  $\mathbf{p} = (E/c, p_x, p_y, p_z) = (E/c, p_T, p_z)$ . In LHC experiments, the coordinate system is defined such that the  $x$ -axis points in the direction of the LHC, and the  $z$ -axis points in the direction of the beam, as shown in Fig. 1.2. In addition to the standard Cartesian coordinates, two observables,  $\varphi$  (azimuthal angle) and  $\eta$  (pseudorapidity), are used to describe the position and momentum of particles relative to the interaction point, which is located at  $x = y = z = 0$ . Pseudorapidity is defined as a function of the polar angle  $\theta$ , where

$$\eta = -\ln(\tan(\theta/2)) \quad . \quad (1.1)$$

For high-momentum particles ( $p \geq mc$ ), pseudorapidity is an approximation of the rapidity relative to the beam, given by

$$y = \frac{1}{2} \ln \frac{E + p_z c}{E - p_z c} \quad . \quad (1.2)$$

Rapidity is a convenient quantity to use because it transforms additively under Lorentz boosts, unlike velocity. In these coordinates, the following relations hold:

$$p_x = |\vec{p}_T| \cos \varphi, \quad p_y = |\vec{p}_T| \sin \varphi, \quad p_z = |\vec{p}| \sinh \eta. \quad (1.3)$$

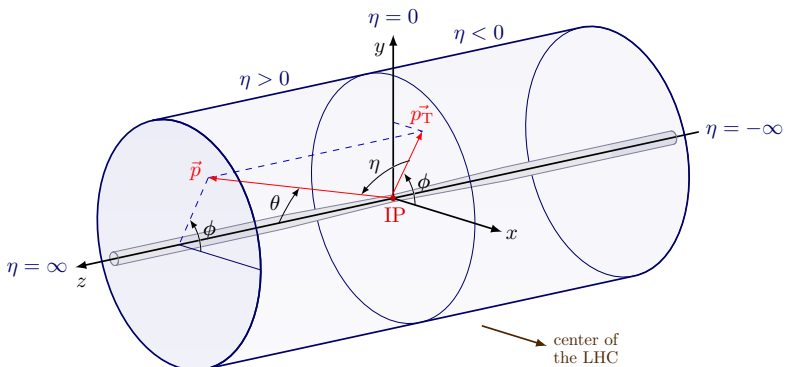


**Figure 1.2:** Coordinate system of an LHC experiment.

## 1.3 Processes involving gluons

Diagrams, screening(?), divergences

### 1.3.1 Running coupling constant

One paragraph, one figure

### 1.3.2 Perturbative QCD

One paragraph

## 1.4 From partons to hadrons

### 1.4.1 Initial and Final State Radiation

In quantum field theory, charged particles are surrounded by a cloud of virtual particles, which can be thought of as fluctuations in the particle's field. For example, the electron state can be described as a superposition of the bare electron plus additional massless bosons:

$$|e\rangle_{\text{phys}} = |e\rangle + |e\gamma\rangle + |e\gamma\gamma\rangle + \dots \quad (1.4)$$

and, at higher orders, pairs of virtual electrons. The fluctuations continuously form and recombine, with their lifetime depending on their energy and momentum. Specifically, the lifetime of a fluctuation with energy  $\omega$  and transverse momentum  $k_T$  can be approximated as:

$$\tau \approx \frac{\omega}{k_T} \quad . \quad (1.5)$$

This implies that fluctuations with smaller- $k_T$  live longer.

As illustrated in Fig. 1.3, the coherent mixed state of the bare charge and the field fluctuations can be disturbed by the presence of an interaction. Intuitively, this interaction can change the energy and momentum of the fluctuations, their formation and recombination, and lead to the emission of radiation in two ways:

- i. a fluctuation is kicked on-shell by the interaction and part of the field continues in its original direction, which leads to Initial State Radiation (ISR);

- as a result of the field of the scattered particle rearranging itself , which can be a source of Final State Radiation (FSR).

In both of the cases, a larger momentum transfer implies more radiation. *For hard, wide angle emissions, cross sections can be calculated perturbatively at fixed orders.*

Soft and collinear emissions, however, lead to infra-red divergences ( $\propto \frac{1}{\omega}, \propto \frac{1}{k_T^2}$ ) and thus, need to be factorised away from the amplitudes or the cross sections and then described using resummation techniques. Without any emissions, the probabilities of finding electrons and photons of fractional momentum  $x$  with respect to the whole system are:

$$f_e(x) = \delta(1 - x), \quad f_\gamma(x) = 0, \quad (1.6)$$

When considering the emissions above some scales parametrised by the resolution parameter  $Q^2$ , these probabilities, however, evolve according to the DGLAP equation:

$$\frac{\partial}{\partial \ln Q^2} \begin{pmatrix} f_e(x, Q^2) \\ f_\gamma(x, Q^2) \end{pmatrix} = \frac{\alpha_{\text{em}}}{2\pi} \int_x^1 \frac{dz}{z} \begin{pmatrix} P_{ee}(z) & P_{e\gamma}(z) \\ P_{\gamma e}(z) & P_{\gamma\gamma}(z) \end{pmatrix} \begin{pmatrix} f_e\left(\frac{x}{z}, Q^2\right) \\ f_\gamma\left(\frac{x}{z}, Q^2\right) \end{pmatrix}, \quad (1.7)$$

where  $P_{ij}(z)$  are the splitting probability functions of a particle  $i$  emitting a particle  $j$ .

In QCD, the behaviour is analogous, with  $\alpha_{\text{em}} \rightarrow \alpha_s$ ,  $e \rightarrow q$ , and  $\gamma \rightarrow g$ .

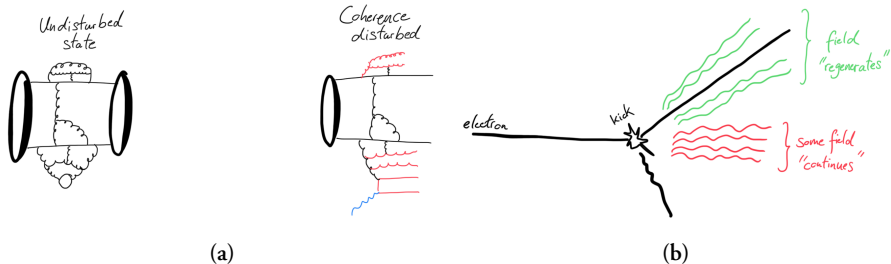


**Figure 1.3:** Illustration of the field fluctuations and emmissions of radiation in a scattering process.

### 1.4.2 Factorisation theorem

The evolution equations 1.7 imply that the probabilities of observing emissions with a fractional momentum  $x$  depend on the resolution  $Q^2$ . In QCD,

1. when applied to the initial state, they are known as parton distribution functions (PDFs) and determine the probabilities of finding partons<sup>1</sup> in the composite hadronic state.
2. When applied to the final state, they are called fragmentation functions, and determine the probabilities of measuring fragments of the outgoing particles.

This leads to the factorisation theorem for processes involving collisions of two hadrons, which separates the perturbatively calculable partonic cross section from the non-perturbative partonic evolution and hadronisation. The theorem can be expressed as follows:

$$\sigma = f_i^A(x_i, \mu_F) f_j^B(x_j, \mu_F) \otimes \hat{\sigma}_{ij \rightarrow n}(\mu_F, \mu_R) \otimes D_{n \rightarrow n'} . \quad (1.8)$$

Here,  $i$  and  $j$  are the initial partons,  $\hat{\sigma}_{ij \rightarrow n}$  is the partonic cross section,  $D_{n \rightarrow n'}$  is the process-specific fragmentation function for evolving the partons  $n$  into the particles' final state  $n'$ , and  $\mu_F$  and  $\mu_R$  are the factorisation and renormalisation scales, respectively. The factorisation scale,  $\mu_F$ , determines the scale below which the emissions are absorbed into the PDFs. The theorem is depicted in Fig. 1.4.

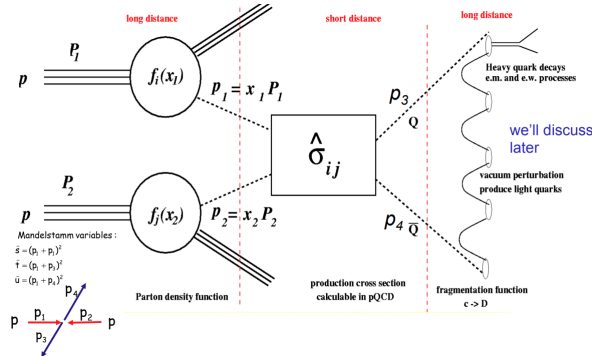


Figure 1.4: Illustration of the factorisation theorem. (NEEDS TO BE REMADE).

### 1.4.3 Parton distribution functions

The PDFs defining the probabilities of finding quarks and gluons in nucleons can be determined experimentally at hadron-electron colliders such as HERA. They are determined from measurements of deep inelastic scatterings in a range of energies and momentum transfers. They are displayed in Fig. 1.5 as a function of the fractional momentum  $x$  (also called Björken  $x$ ).

---

<sup>1</sup>Partons refer to the valence quarks, sea quarks, and gluons inside hadrons.

According to collider kinematics,  $x \propto \frac{1}{\sqrt{se^y}}$ , therefore, the partonic composition of ultra-relativistic hadrons is dominated by gluons. Following unitarity principles and BK evolution equation, it is expected that gluons start recombining and the gluonic content saturates as  $x \rightarrow 0$ . This is actively researched, however, not directly measured yet. Additionally, it should be noted that in ultra-relativistic heavy nuclei, the partons are modified in the contracted nuclear environment and the PDFs are referred to as nPDFs.

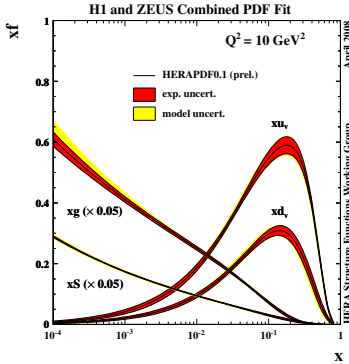


**Figure 1.5:** Parton distribution functions determined at HERA. TBA

#### 1.4.4 Parton fragmentation and the Lund string

After the scattering process, the produced partons continue to fragment by emitting more partons in a process called the parton shower. Since the coupling strength in QCD increases with decreasing the energy scale of the splitting, this leads to the production of many soft, collimated emissions known as jets. The partonic evolution continues until the virtuality of the partons reaches the hadronization scale ( $\approx \Lambda_{\text{QCD}}$ ). There are multiple frameworks within QCD to describe the evolution of partons into their final state, such as using the DGLAP equations or the so-called dipole formalism.

Once the partonic final state is reached, the partons hadronise into the observable mesons and baryons. The hadronisation process is not calculable in QCD and requires phenomenological models to describe it. One such model is the Lund String model, which describes hadronisation as the breaking of a color string between the quarks in the final state. In this model, the energy stored in the color string is converted into the mass of new hadrons.

According to confinement, hadronisation should involve at least two partons with

complementary colours. In QCD, the  $q\bar{q}$  potential takes the shape of

$$V_{q\bar{q}} \approx -\frac{4}{3} \frac{\alpha_s \hbar c}{r} + \kappa r , \quad (1.9)$$

where  $\kappa$  is a parameter with value around  $1\text{GeV}/\text{fm}$ . In the non-perturbative regime (long distances), the potential is dominated by the linear part, which is reminiscent of a system bound by a string with tension  $\kappa$ . This is taken advantage of by the Lund string model – a  $q$  and  $\bar{q}$  pair separated by distance  $\Delta x$  is bound by a color field (string) with energy  $\kappa\Delta x$ .

If the  $q$  and  $\bar{q}$  continue separating as a result of the scattering, the energy stored in the color field increases. At some point, it can become energetically favourable to produce a new  $q\bar{q}$  pair out of vacuum, which is a quantum mechanics tunnelling phenomenon characterised by the probability:

$$\frac{dP}{dm_T} \propto \exp\left(-\frac{\pi m_T^2}{\kappa}\right) , \quad (1.10)$$

where  $m_T$  is the transverse mass of the produced quarks. Otherwise, the  $q\bar{q}$  system starts contracting and oscillates with a period  $T = 2E_{\text{kin}}/\kappa$ , where  $E_{\text{kin}}$  is its maximum kinetic energy. The produced  $q$  and  $\bar{q}$  then connect by new color fields to the original pair. This process repeats itself resulting in cascade of many  $q\bar{q}$  pairs connected by many color strings. In this description, baryons can also be created by double tunnelling of a  $qq\bar{q}\bar{q}$  pair. The process is illustrated in Fig. ??.

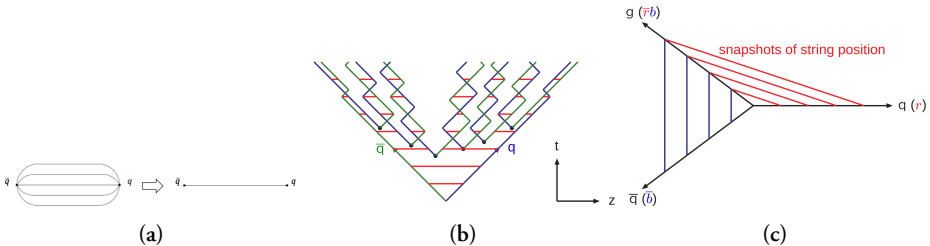


**Figure 1.6:** Illustration of the color field between two quarks and its simplified representation with a string. Illustration of the string splitting by producing new  $q\bar{q}$  in the  $t-z$  plane. Illustration of the treatment of gluons in the Lund string model.

Equation 1.10 also implies that production of strange quarks is suppressed by a factor of

$$\rho = \exp\left(-\frac{\pi(m_s^2 - m_{u,d}^2)}{\kappa}\right) . \quad (1.11)$$

This parameter is typically tuned to data, as substituting constituent ( $m_s \approx 0.5 \text{ GeV}/c^2$ ,  $m_{u,d} \approx 0.33 \text{ GeV}/c^2$ ) versus current masses ( $m_s \approx 0.1 \text{ GeV}/c^2$ ,  $m_{u,d} \approx 0$ ) leads to considerable differences underestimating and overestimating data, respectively.

For a  $q\bar{q}g$  system, in this model, the gluon connects to the quark and antiquark and is effectively treated as a “kink” on the color field, adding energy and momentum to the  $q\bar{q}$  string (stretching it in its direction), as visualised in Fig. ??.

It should be noted that in the paradigm of AA collisions, hadron production can be alternatively modelled by hadronisation at the QGP’s phase boundary by *coalescing* free quarks.

## 1.5 Multiple partonic interactions

Results from Sp $\bar{p}$ S in the 1980s sparked motivations for considering interactions of multiple partons between the two composite protons. For example, the AFS experiment observed an abundance of 4-jet events, displayed in Fig. 1.7, that could not be explained by calculations considering a double gluon bremsstrahlung from a single partonic scattering? . Furthermore, UA5 measurements studying energy dependence of multiplicity distributions  $P(N_{\text{ch}})$  from revealed a significant broadening when increasing  $\sqrt{s}$ , and saw the so-called KNO scaling? , where  $P(N_{\text{ch}})/\langle N_{\text{ch}} \rangle$  remains constant, which was not reproducible in the context of  $N_{\text{ch}}$  being produced from a single string? . This further suggested at the presence of multiple production sources.

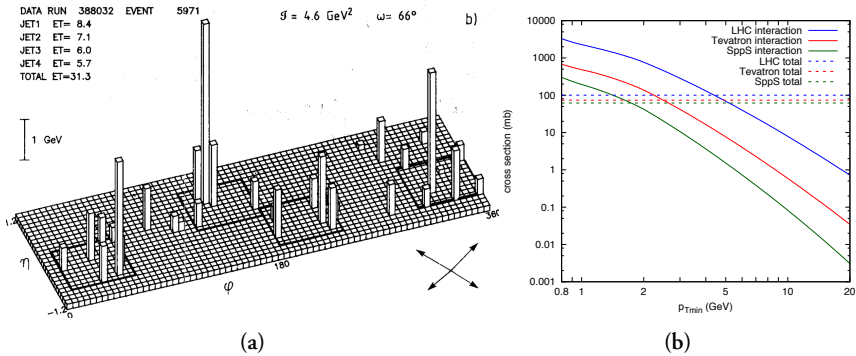


**Figure 1.7:** TBA.

These findings prompted further development of Regge theory and approaches that incorporated multiple pomerons, which were successful in describing the  $N_{\text{ch}}$  distributions. However, this approach is fully decoupled from descriptions of the per-

turbative primary scattering. Subsequently, much of the phenomenology related to multiple partonic interactions was developed within the framework of the Pythia MC event generator, which is discussed individually in Section X. However, nowadays, the relevance of the concept of MPIs in hadronic collisions extends beyond this generator. A scattering with double partonic interactions is illustrated in Fig. 1.8.

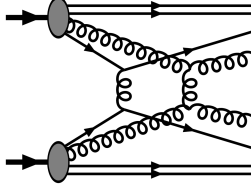


**Figure 1.8:** TBA.

In the Pythia approach, MPI are treated as additional perturbative scatterings. In QCD, the  $2 \rightarrow 2$  cross section (dominated by the gluon exchange t-channel) diverges as  $\propto \alpha_S^2(k_\perp^2)/k_\perp^4$ , so a cutoff parameter  $k_{\perp/\min}$  must be introduced, and using (??) leads to:

$$\frac{d\sigma}{dk_\perp^2} = \sum_{ij} \int dx_1 dx_2 f_i(x_1, \mu_F^2) f_j(x_2, \mu_F^2) \frac{d\hat{\sigma}_{ij}^H}{dk_\perp^2}, \quad (1.12)$$

$$\sigma_{\text{int}}(k_{\perp,\min}) = \int_{k_{\perp,\min}^2}^{s/4} \frac{d\sigma}{dk_\perp^2} dk_\perp^2. \quad (1.13)$$

The choice of cutoff can be tuned to experimental data, and for the SppS energy of  $\sqrt{s} = 630$  GeV, a value of around 1.6 GeV/c was typical. The dependence of this parton-parton scattering cross section is shown in Fig. 1.7.

The total pp cross-section, which is on the order of 100 mb at  $\sqrt{s} = 13$  TeV, is given by

$$\sigma_{\text{pp}} = \sigma_{\text{elastic}} + \sigma_{\text{single dif.}} + \sigma_{\text{double dif.}} + \sigma_{\text{non-dif.}}, \quad (1.14)$$

where the inelastic cross sections  $\sigma_{\text{inel}} \approx \sigma_{\text{double dif.}} + \sigma_{\text{non-dif.}}$  corresponds to approximately 60% of the total. The mean number of MPIs,  $\langle n_{\text{MPI}} \rangle$ , can be estimated using:

$$\langle n_{\text{MPI}} \rangle(k_{\perp,\min}) = \frac{\sigma_{\text{int}}(k_{\perp,\min})}{\sigma_{\text{inel}}} \quad (1.15)$$

However, the actual treatment is more complex and involves considerations of other parameters such as the dampening factor  $k_\perp^0$  to account for the confinement nature of

partons, modifications of multiparton PDFs, energy-momentum conservation effects,  $x$ -dependent source geometry, and the intertwinedness of partonic evolutions.

In summary, MPIs represent several subcollisions that take place in an average pp collision with  $p_T$  scales of a few GeV. They are colour-connected to the beam remnants, which in the Lund model are represented by strings. Since a string with  $\kappa = 1\text{GeV}/\text{fm}$  yields, as a rule of thumb, approximately one hadron per unit rapidity, and the average pp collision at the LHC at  $\sqrt{s} = 13\text{ TeV}$  has  $\langle dN_{\text{ch}}/dy \rangle \approx 6$ , the typical number of partonic interactions is around six.

Finally, the observation of QGP-like phenomena in pp collisions at the LHC has renewed interest in MPI phenomenology, as discussed in the following chapter. Such observations do not contradict the concept of MPIs; rather, they suggest the possibility of incorporating collective behavior among the MPIs, such as interactions between strings, local modifications of string tensions, or, alternatively, the formation of a multipartonic state with QGP-like properties.

### 1.5.1 Color reconnection

The incorporation of MPIs improved the description of the  $N_{\text{ch}}$  distributions and their dependence on  $\sqrt{n}$ . However, there were also observations of  $\langle p_T \rangle(N_{\text{ch}})$  increasing as a function of  $N_{\text{ch}}$ , which could not be explained. More MPIs lead to more strings, which in turn leads to the production of more particles, but the  $p_T$  is mostly unaffected. This would predict a weaker dependence of  $\langle p_T \rangle$  on  $N_{\text{ch}}$ , contrary to the data. The issue was resolved by implementing a possible color reconnection mechanism, which rearranges the color fields between partons.

TBA Insert diagrams of the processes!

One can envision the following process:

$$e^+ e^- \rightarrow W^+ W^- \rightarrow q_1 \bar{q}_2 q_3 \bar{q}_4.$$

In this scenario, a color reconnection mechanism could rearrange the colour-connected  $q_1 \bar{q}_2$  and  $q_3 \bar{q}_4$  into  $q_1 \bar{q}_4$  and  $q_3 \bar{q}_2$  if it were energetically favourable, depending on the phase-space configurations. Measurements at LEP of this process have indeed shown that such final-state corrections must be taken into account to explain the data on  $W$  masses and widths. They also reported that the reconnection probabilities for such events are on the order of 50%, further indicating that colour reconnection is an important factor to consider.

Pythia implements CR by minimizing the total length of strings in the system, analogous to minimising potential energy. This mechanism, illustrated in Fig. 1.9, explains

the rising trend of  $\langle p_T \rangle (N_{\text{ch}})$ : shorter strings imply fewer hadrons to split the transverse boost across, and the more MPI, the bigger this effect. Moreover, CR also helped describe the absolute value of  $\langle p_T \rangle$ . With this approach, no further modifications of fragmentation parameters were necessary, in line with the concept of jet universality. However, it should be noted that there are various CR implementations and all rely on parameters obtained from tuning to data.

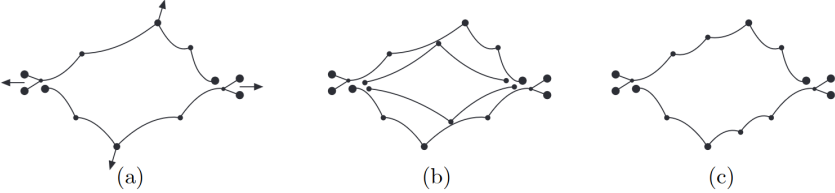


**Figure 1.9:** a) In a hard parton subcollision, the outgoing gluons are connected to the beam remnants through colour. Additional gluon kinks may occur through initial state radiation, which are ordered by rapidity. (b) A second hard scattering should theoretically result in two new strings connected to the remnants. (c) In order to minimise the total string length, gluons are colour reconnected.

It is also worth noting that the  $p_T$  boost acquired through color reconnection may depend on mass and whether a hadron is a baryon or meson, which somewhat mimics the hydrodynamic signatures of collective flow observed in AA collisions.

## 1.6 Underlying event

The underlying event (UE) in high-energy collisions refers to the additional hadronic activity that accompanies the primary hard scattering process, but is not directly related to it. This includes the fragmentation products of the beam remnants, ISR and FSR, as well as the effects of the previously discussed MPIs. The UE is typically characterized by the distribution of softer particles around and far outside of the hard process.

It is important to note that the UE is different from the MB production, as it is biased by the presence of hard scattering. Additionally, the magnitude of the UE can fluctuate from event to event.

TBA Maybe some illustration/plot

## 1.7 Lattice QCD

One paragraph

## 1.8 QCD phase diagram

One paragraph, figure

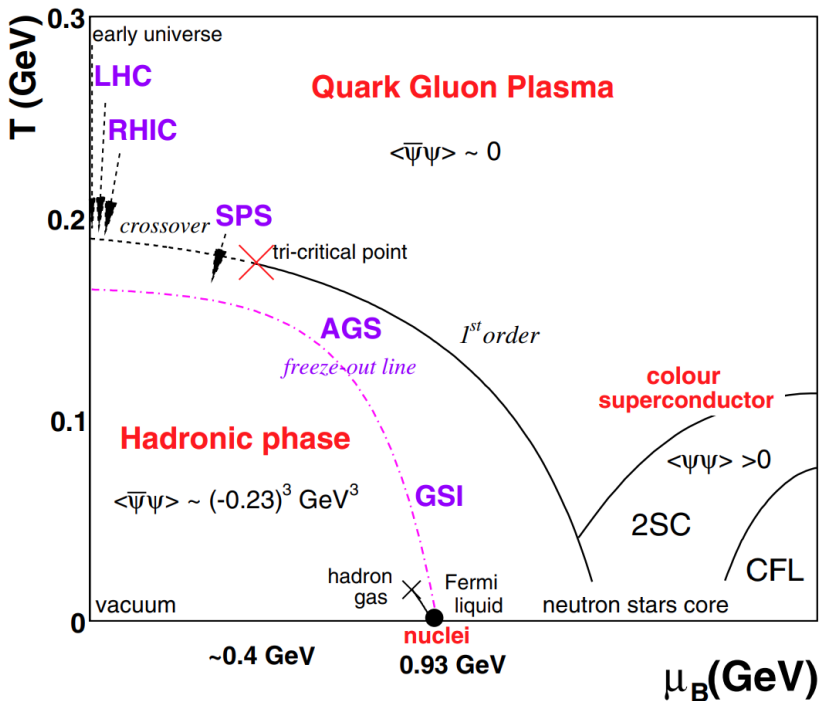


Figure 1.10: TBA

### 1.8.1 Phase transition

One paragraph, bag model derivation of  $T$

### 1.8.2 Chiral symmetry restoration

One paragraph, figure

## 1.9 Implications of high-activity QCD research

One paragraph



# Chapter 2

## QCD phenomena in high energy hadronic collisions

The aim of this chapter is to give an introduction to the physics of heavy ions and the various phenomena related with the quark-gluon plasma QGP. Furthermore, a detailed summary of the findings of QGP phenomena in small systems, i.e. pp and pA collisions, is given.

### 2.1 Collisions of heavy nuclei

#### 2.1.1 Collision geometry, Centrality, multiplicity

Collisions of heavy nuclei, composed of many fluctuating nucleons, may occur under various initial state configurations. Some quantities used to describe them are the impact parameter  $b$ , defined as the distance between the two nuclei centers, number of participating (scattered) nucleons  $N_{\text{part}}$ , and the number of binary nucleonic collisions  $N_{\text{coll}}$ .

Determining these quantities is important because:

1. Soft processes, such as light flavor particle production, are expected to scale with the interaction volume, which  $\propto N_{\text{part}}$ .
2. Hard processes, such as jet and heavy flavor production, are expected to scale with the number of large momentum transfer interactions given by  $N_{\text{coll}}$ .

3.  $b$ , disregarding the fluctuations of nucleonic positions, defines the shape and anisotropy of the overlap region, which are important initial state conditions.

Since these quantities cannot be directly measured, they need to be modelled. The charged particle *multiplicity* is commonly used for this purpose, as  $\langle N_{\text{ch}} \rangle$  increases monotonically with  $N_{\text{part}}$ ,  $N_{\text{coll}}$ , and decreasing  $b$ . Multiplicity  $N_{\text{ch}}$  can be measured experimentally, e.g. with tracking detectors. The concept of *centrality* is also used, which is defined as quantiles of the total nuclear cross-section. For example, a centrality of 0 – 5% refers to low  $b$  values and the top 5% of  $N_{\text{ch}}$  values (central events), while 95 – 100% centrality refers to high  $b$  values and the bottom 5% of  $N_{\text{ch}}$  values (peripheral events). Centrality can also be inferred from other *event activity* classifiers, such as amplitudes of scintillators at forward rapidity, transverse energy in calorimeters, or energy from beam remnants in zero-degree-calorimeters.

In AA collisions, these relationships are well-defined, and thus the models perform well. The most popular model is the MC Glauber model. Other models include MC-KLN and IP Glasma.

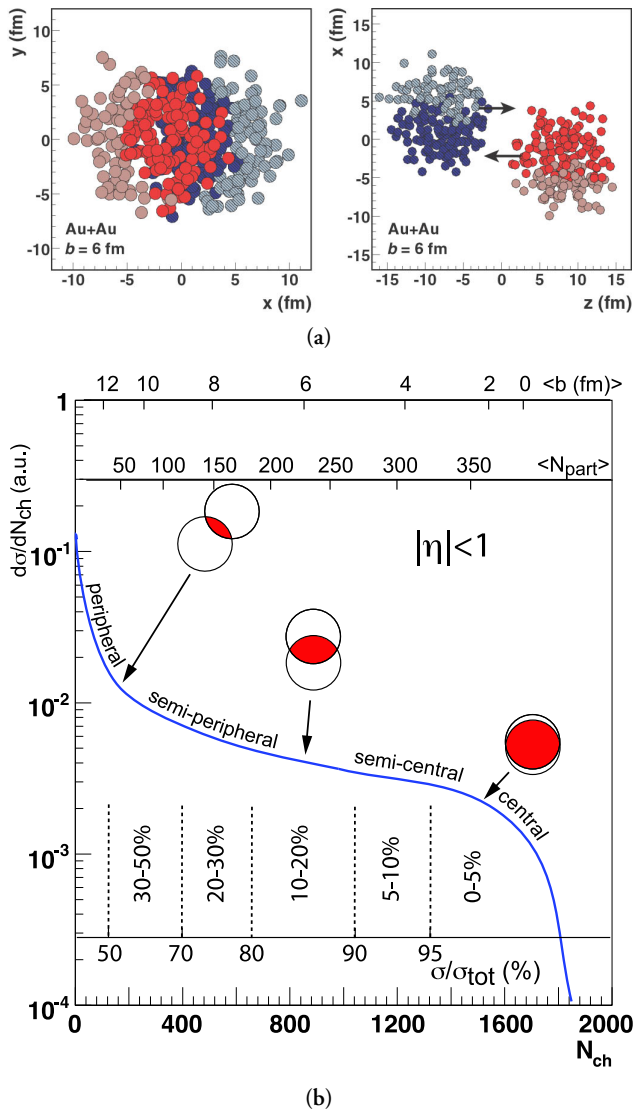
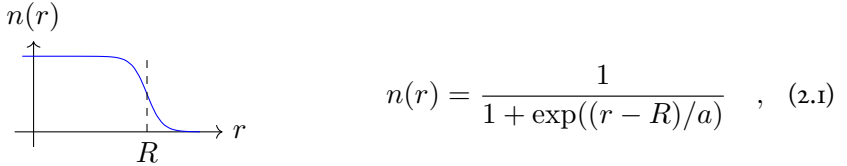


Figure 2.1: TBA

### 2.1.2 MC Glauber model

The MC Glauber model takes on a very simple albeit powerful approach. The two nuclei are simulated in three dimensions in a way that satisfies their respective nuclear density profiles, usually modelled by sampling the positions of nucleons from the Wood-Saxon distribution:



where  $R$  is the nuclear radius and  $a$  the nuclear skin thickness.

The nucleonic densities can be represented by uniform disks, or more accurately by Fermi-distributions or Gaussian profiles to account for fluctuations of their densities. Their parameters are left free and are tuned to the data.

A random impact parameter is then chosen or sampled. The collision is then treated as a sequence of independent binary nucleon-nucleon collisions, where

1. nucleons remain travelling in straight lines,
2. the inelastic nucleon-nucleon cross section  $\sigma_{\text{NN}}$  does not depend on the number of interactions,
3. two nucleons are considered to interact if their transverse relative distance  $d \leq \sqrt{\sigma_{\text{NN}}/\pi}$ .

Fig. 2.1 illustrates an example of a Glauber Monte Carlo event for a Au+Au collision. By simulating numerous collisions, the average  $N_{\text{part}}$  and  $N_{\text{coll}}$  are determined<sup>1</sup>, and their relations to centrality and event activity observables are determined by fitting to experimental data.

Recent studies have extended the MC Glauber model to include sub-nucleonic structures. Such efforts show that the production of charged hadrons at mid-rapidity scales linearly with the number of participating partons. Comparisons with LHC data at  $\sqrt{s_{\text{NN}}} = 5.02 \text{ TeV}$  suggest that the number of sub-nucleonic degrees of freedom ranges from 3 to 5? .

## 2.2 Quark-gluon plasma

In agreement with lattice QCD predictions, the QGP has been measured in ultra-relativistic collisions of heavy nuclei at RHIC?, LHC?, and even SPS?. Although it

---

<sup>1</sup>It also shows the scaling between the numbers of participants and binary collisions, which is approximately  $N_{\text{coll}} \approx 0.35 N_{\text{part}}^{4/3}$ .

cannot be observed directly, a wealth of evidence from three decades of research combining various observables reveals the effects of the produced QGP medium. Whilst somewhat context-dependent, the following features make QGP the most extreme phenomena observed phenomena in terms of its:

- *Temperature*: QGP temperatures reach values on the order of hundreds of MeV, which corresponds to approximately  $2 \times 10^{12}$  K.<sup>2</sup>
- *Viscosity*: the shear viscosity to entropy density ratio  $\eta/s$  reaches the minimum quantum limits of  $1/4\pi$ , making it an almost perfect liquid.
- *Vorticity*: in semi-peripheral collisions, the rotating plasma reaches a vorticity parameter of approximately  $0.4 \text{ fm}^{-1}$ .
- *Magnetic field*: in non-central collisions, the magnetic fields of the heavy nuclei may peak at  $\sim 10^{19}$  T.

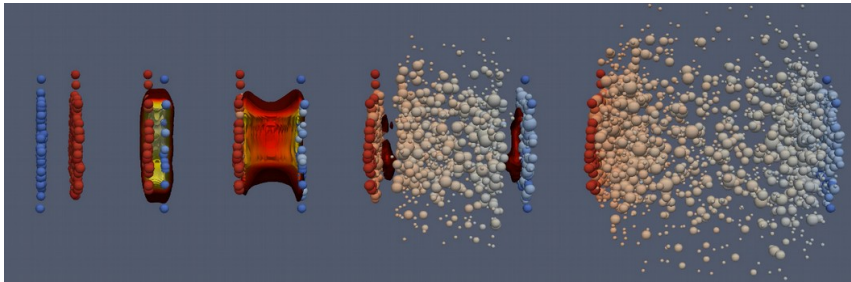


**Figure 2.2: TBA**

Figure 2.2 illustrates the mainstream paradigm of a heavy nuclei collisions evolution:

1. The Lorentz-contracted heavy nuclei approach each other at ultra-relativistic speeds.
2. *Pre-hydrodynamisation stage* ( $\tau \equiv \sqrt{t^2 - z^2} \leq 1 \text{ fm}/c$ ): “hard” particles are produced in scatterings with the highest momentum transfer  $Q^2$ , produced matter expands rapidly in longitudinal directions and starts expanding in radial direction.
3. *Hydrodynamisation* ( $1 \leq \tau \leq 10 \text{ fm}/c$ ): partons are abundantly produced, creating a deconfining medium and allowing the system to be described by hydrodynamic equations.

---

<sup>2</sup>Contrasting some of the lowest temperatures required for the super-conducting magnets of the LHC,  $T \approx 1.9 \text{ K}$ .

4. *Chemical freeze-out* ( $\tau \sim 20$  fm/c): the cools down, hadronises, produced hadrons then stop interacting inelastically and the system's chemical content is stabilised.
5. *Thermal freeze-out*: hadrons no longer interact elastically and their kinematics stabilize.

The following subsections outline some of the essential phenomena related to the production of QGP.

### 2.2.1 Quarkonium dissociation and sequential suppression

Heavy quarkonia are vector mesons of  $c\bar{c}$  and  $b\bar{b}$ . They include  $J/\psi$ ,  $\psi(2S)$ ,  $\Upsilon(1S)$ ,  $\Upsilon(2S)$ ,  $\Upsilon(3S)$ , which can be relatively easily measured in LHC experiments via their di-lepton decay channels. They are created solely in the first phases of the collision and then experience the entire evolution of the QGP medium:

$$t_{\text{creation}}^{Q\bar{Q}} < t_{\text{creation}}^{\text{QGP}} < t_{\text{lifetime}}^{\text{QGP}} \ll t_{\text{lifetime}}^{Q\bar{Q}} . \quad (2.2)$$

Additionally, due to their large binding energies, their radii may remain smaller than the plasma screening radius  $r_D(T)$ , and thus, survive the dissociation. For instance, considering their in-vacuum radii determined from the  $q\bar{q}$  potential,  $r_{\Upsilon(1S)} \sim 0.14$  fm,  $r_{\Upsilon(2S)} \sim 0.28$  fm,  $r_{\Upsilon(3S)} \sim 0.39$  fm, which contrast the  $r_\pi \sim 0.7$  fm. This implies that different temperatures result in the dissociation of different states, and measuring the production of different states can help infer QGP temperature, as illustrated in Fig. 2.3.

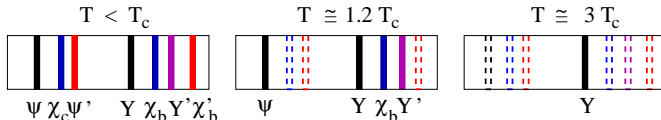


**Figure 2.3:** TBA

The production of heavy quarkonia in AA collisions is compared to that in pp collisions through the nuclear modification factor,  $R_{AA}$ . This factor is widely used in various other AA measurements and is defined as:

$$R_{AA} = \frac{dN_{AA}/dp_T}{\langle N_{\text{coll}} \rangle dN_{pp}/dp_T} . \quad (2.3)$$

$R_{AA}$  can take on the following values:

- i.  $R_{AA} = 1$ : There is no net effect on the production, corresponding to the absence of the QGP medium and other nuclear effects.
- ii.  $R_{AA} < 1$ : The production is overall suppressed, for example, due to dissociation.
- iii.  $R_{AA} > 1$ : The plasma and nuclear effects systematically enhance the measured production.

At LHC energies, the abundance of charm quarks in the QGP is high enough that charmonia can be reformed after dissociation, which somewhat complicates the interpretation of their suppression. However, the  $\Upsilon(3S)$  bottomonium has  $R_{AA}$  consistent with 0 at  $\sqrt{s_{NN}} = 5.02$  TeV, as shown in Figure 2.4. This complete suppression is a clear signature of the QGP and can be used together with models to estimate the QGP temperature at these energies as  $T \approx 630$  MeV.

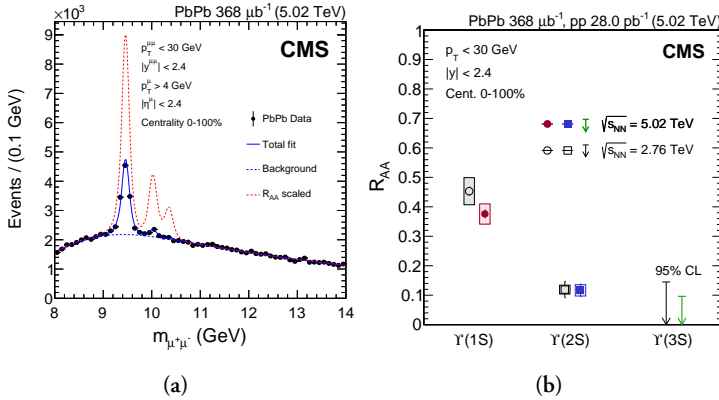


**Figure 2.4:** TBA

### 2.2.2 Strangeness enhancement

In vacuum hadronisation, production of strangeness is suppressed not only due to the higher current mass of the strange quark ( $m_s \approx 0.1 \text{ GeV}/c^2$ ), but especially due to the much higher constituent mass ( $m_K \approx 5 \text{ GeV}/c^2$ ). On the other hand, in the QGP, due to high gluon densities and  $T \sim m_s$ , production of strangeness is may equilibrate with  $u$  and  $d$  through gluon fusion:

$$gg \rightarrow s\bar{s} \quad .$$

Indeed, one observes an enhancement in production of strange hadrons in AA collisions, one that is dependent on the event-activity, and also increases with increasing

the strangeness content of the hadron. These results can be seen in Fig. 2.5. In the context of AA collisions, such observations are well described by statistical hadronisation models assuming...and have been consider an important signature of a QGP formation.

Also can be described in terms of a canonical/grand-canonical system – TBA.

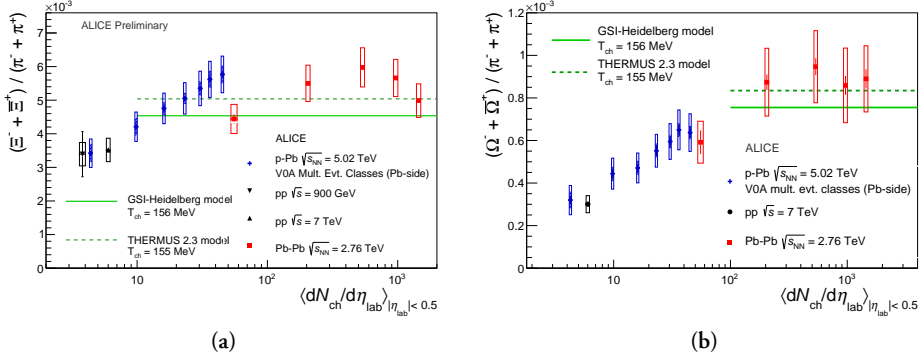


Figure 2.5: TBA

## 2.2.3 Collective flow

TBA Two paragraphs

## 2.2.4 Jet quenching

TBA One paragraph

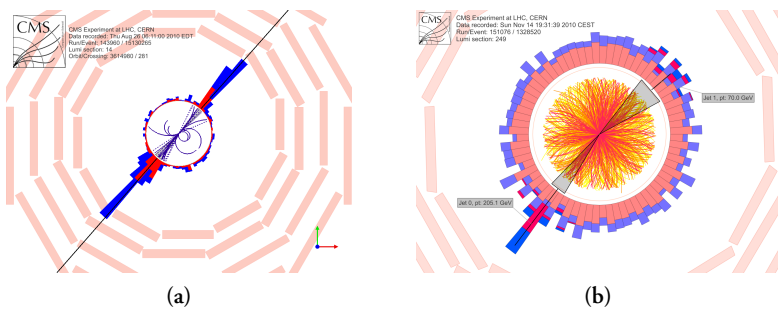


Figure 2.6: TBA

## 2.2.5 Cold nuclear matter effects

It should be noted that apart from the QGP, other effects come into play due to the fact that the collision involves two nuclei instead of two protons. These effects are important caveats to bear in mind and include:

1. Nuclear (anti-)shadowing: Reflects the modification in production due to differences in nPDFs and PDFs.
2. Cronin effect: Describes the initial parton energy loss due to scatterings in the nuclear medium and broadens measured  $p_T$  spectra.
3. Nuclear absorption: Describes the dissociation of particles due to their interactions with the passing-by nuclear remnants. It is generally negligible at LHC energies.
4. Co-mover absorption: This is the effect of inelastic interactions with the hadron gas.

These effects can be isolated and quantified in pA or very peripheral AA collisions.

## 2.3 QGP phenomena in small systems

Measurements within the last decade have shown that certain QGP phenomena can also be observed in high-multiplicity events of pp collisions at LHC energies, which challenges the traditional assumption that QGP is only produced in AA collisions. This has sparked debates about the existence of QGP in pp collisions and, to a lesser degree, about the absence of QGP in AA collisions, despite the extensive experimental evidence.

Furthermore, the observed behavior of these phenomena indicates that the role of event multiplicity  $N_{\text{ch}}$  may be more significant than system size. This has led to ongoing efforts to establish a consistent and seamless link between the paradigms of pp and AA collisions.

### Strangeness and charm enhancement

ALICE measurements on  $\Lambda/\pi$ ,  $\Xi/\pi$ , and  $\Omega/\pi$  ratios demonstrate that the production rates of particles containing strange quarks increase faster with multiplicity than those

containing only u and d quarks. This also depends on the strangeness content – the effect is the strongest for  $\Omega$  and vanishes for protons. Furthermore, the evolution to larger systems seems to be continuous with respect to  $N_{\text{ch}}$ . The measurements can be seen in Fig. 2.7.

To contrast the strangeness measurements with heavier flavour, the  $J/\psi / \pi$  ratio also shows a clear increase in yield with increasing  $N_{\text{ch}}$  in pp collisions, as is shown in Fig. 2.7. However, this comes with an important caveat: high-multiplicity events are biased to have enhanced hard processes, as discussed further in Chapter X. Moreover, the evolution of this phenomenon is also not continuous with  $N_{\text{ch}}$  when going from pp collisions at  $\sqrt{s} = 13$  TeV to  $\sqrt{s_{\text{NN}}} = 5.02$  TeV, which can also be explained by the fact that charm quarks are produced solely in hard scattering processes, the rates of which depend on the collision system and center-of-mass energy.

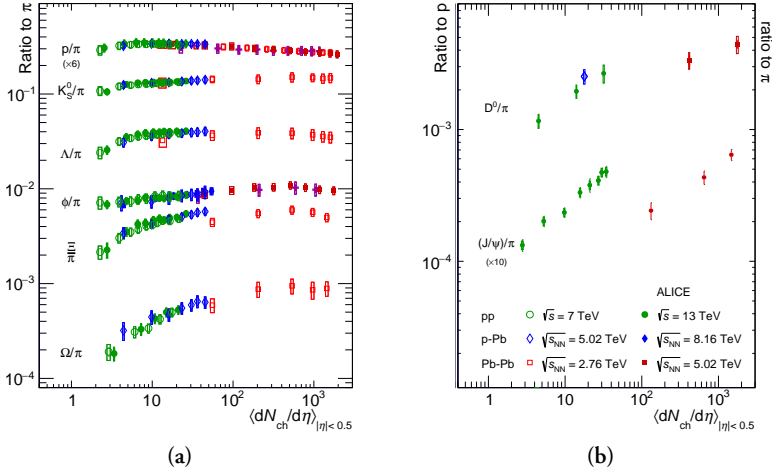


Figure 2.7: TBA

## Anisotropic flow

Azimuthal correlations and anisotropic flow measurements in small collision systems exhibit features similar to those observed in AA collisions, hinting at the presence of collective expansion. However, in small systems, these measurements are particularly challenging due to their large sensitivity to non-flow effects, such as jet fragmentation or resonance decays, which can mimic the features of collective flow.

While models using hydrodynamic-like descriptions seem to be able to describe the data, especially at high multiplicities, the interpretation of the results in small systems is still under investigation. The values of elliptic flow  $v_2$  seem to be comparable to

those in low-multiplicity Pb-Pb collisions, although the evolution of  $v_2$  across different system sizes does not appear to be smooth. The measurements from CMS displaying a clear ridge in high-multiplicity events and the  $v_2$  results from ALICE can be seen in Fig. 2.8.

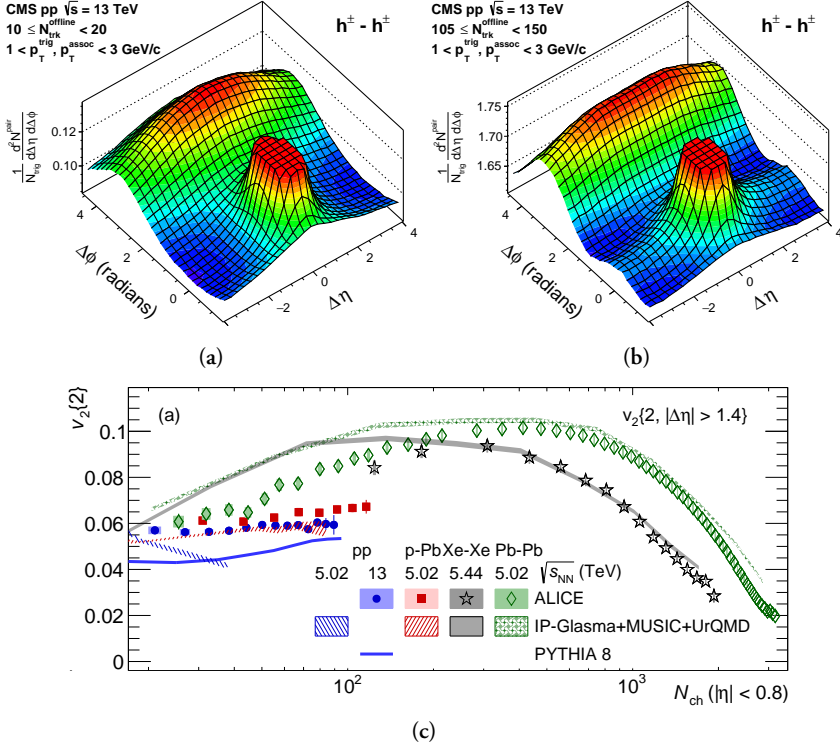


Figure 2.8: TBA

## Radial flow

Measurements of the ratio of  $\Lambda$  to  $K_S^0$   $p_T$  spectra ratio were also studied in pp collisions with differing  $N_{\text{ch}}$ . The boost of a collectively expanding system, as expected in the context of radial flow, should have a greater impact on heavier hadrons, leading to an enhancement of the baryon-to-meson ratio at intermediate  $p_T$ . This enhancement is observed in the  $(\Lambda^0 + \bar{\Lambda}^0)/(2K_S^0)$  ratio, its magnitude increases with increasing  $N_{\text{ch}}$  and the peak position shifts towards higher values collisions, consistent with the hydrodynamic picture. The increase at intermediate momenta leads to a corresponding depletion at low  $p_T$ . Integrated (or high- $p_T$ )  $(\Lambda^0 + \bar{\Lambda}^0)/(2K_S^0)$  ratios exhibit essentially no (or minor) multiplicity dependence. This observation also applies to

proton-to-pion ratios.

Recent studies have also investigated the charmed baryon-to-meson ratio  $\Lambda_c/D^0$ , with similar findings, although measurements with smaller uncertainties are still required. Fig. 2.9 presents the corresponding results.

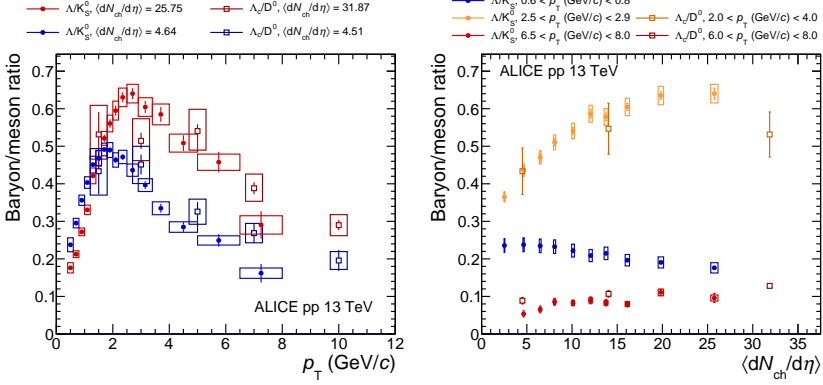


**Figure 2.9:** TBA

### Sequential suppression of $\Upsilon$ states

While defining  $R_{AA}$  to compare high-multiplicity and low-multiplicity events is unclear, and measuring yields as a function of  $N_{ch}$  is complicated by its biases related to the hardness of primary scatterings, it is worthwhile to investigate the ratio of excited-to-ground states of quarkonia as a function of  $N_{ch}$ .

Interestingly, these results exhibit a decrease with increasing  $N_{ch}$ , resembling the pattern of sequential suppression due to QGP deconfinement. Even more remarkable, this dependence disappears in low-sphericity, jet-dominated, events (event shape observables such as sphericity are discussed in more detail in Chapter X). These findings, reported in Fig. 2.10, suggest that the dependence on  $N_{ch}$  is solely influenced by the UE, rather than jets. As event multiplicity grows larger, excited  $\Upsilon$  states become relatively less likely to be measured compared to the ground state.

These results indicate the need for a better understanding of  $\Upsilon$  hadronization and the role UE may play in it. They also raise the question of whether the ground state is enhanced rather than the excited states being suppressed. Additionally, the effects of the mass differences must also be considered. However, the fact that low-sphericity, jet-dominated events have the same ratios as high-sphericity, UE-dominated events at low  $N_{ch}$  argues against these ideas.

An important caveat to note is that hadronic decays (which are dominant) of the heavy  $\Upsilon$  states may result in tens of produced  $N_{\text{ch}}$ . Therefore, even minor discrimination against the excited states could hypothetically be correlated with a substantial but trivial increase in the accompanying  $N_{\text{ch}}$ . To the author's knowledge, there are currently no available phenomenological descriptions of the observed behavior, which further limits potentially groundbreaking interpretations.

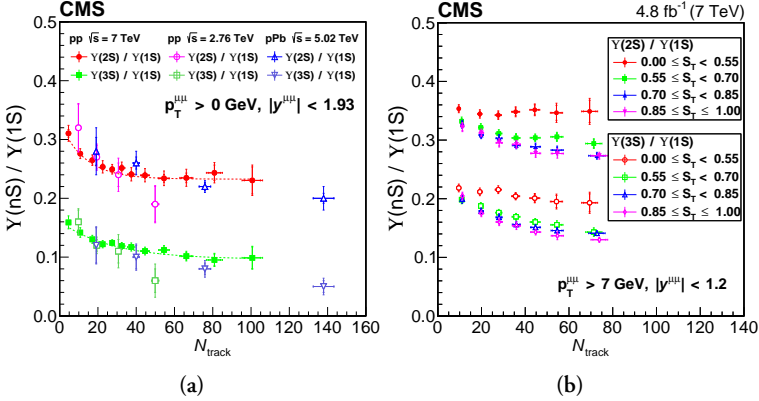


Figure 2.10: TBA

## Other QGP signatures

Jet quenching

### 2.3.1 Role of multiplicity

The observations made above highlight the significance of studying the role of multiplicity  $N_{\text{ch}}$ . In contrast to AA collisions, high-multiplicity events in pp collisions do not arise from a mere increase in the amount of colliding matter, as the values of  $N_{\text{part}}$  and  $N_{\text{coll}}$  are fixed:

$$N_{\text{part}} = 2, \quad N_{\text{coll}} = 1. \quad (2.4)$$

Additionally, due to the relatively constant initial system volume, high- $N_{\text{ch}}$  pp events may exhibit energy densities that exceed the threshold for QGP formation, given that the highest  $N_{\text{ch}}$  values are similar to those observed in peripheral AA collisions, where QGP formation is observed.

Clearly, the picture is more complex and despite its simplicity as an event activity classifier,  $N_{\text{ch}}$  poses challenges when it comes to relating data to theory since it cannot be directly linked to the initial state, and multiplicities in different events may originate from entirely different processes.

To address these issues and gain a better understanding of the evolution between low and high multiplicities and the potential for QGP formation, this dissertation focuses on transverse spherocity  $S_O^{(p_T=1.0)}$  and underlying event activity  $R_T$  measurements. They may offer a deeper insight into the relevant degrees of freedom involved.

## 2.4 Phenomenological models

### 2.4.1 Pythia

Pythia is a Monte Carlo event generator used in particle physics to simulate high-energy particle collisions, based on perturbative QCD. The program uses a modular structure to simulate different aspects of the collision process and includes the simulation of the hard scattering, multiple parton interactions, initial and final state QCD radiation, and hadronization. Recently, Pythia has also incorporated the implementation of Angantyr, a new model for the simulation of collisions of nuclei.

A pp collision event, as simulated by Pythia, can be seen in the illustration in Fig. 2.11.

TBA Explain in more detail!!

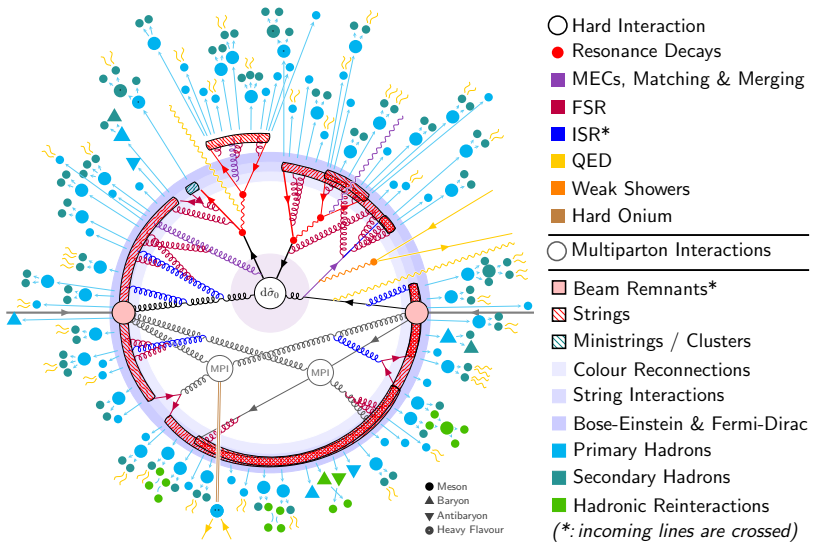


**Figure 2.11:** TBA

## String interactions and Ropes

Two paragraphs

### 2.4.2 Epos LHC

Description of Epos in two paragraphs



## **Part II**

# **Experimental Setup and Methodology**



# Chapter 3

## Large Hadron Collider

*This chapter is currently unfinished and needs a lot of work.*

### 3.1 European Organisation for Nuclear Research

CERN, located near Geneva, Switzerland, is an esteemed scientific institution dedicated to the study of particle physics, nuclear physics, and related fields. Established in 1954 by a consortium of European countries, it currently has 23 member states and collaborates with over 50 countries worldwide. Its research endeavors focus on advancing our understanding of the fundamental particles and forces that govern them.

One of the most significant and celebrated discoveries made by CERN is the Higgs boson, a particle that confers mass to other particles and is a crucial component of the Standard Model of particle physics. This discovery was made in 2012 by the ATLAS and CMS experiments, two of the four main experiments at CERN's Large Hadron Collider (LHC), the world's largest and most powerful particle accelerator.

Apart from the LHC, CERN houses several research facilities, including the Proton Synchrotron and the Super Proton Synchrotron, that provide beams of particles for a wide range of experiments.

### 3.2 Large Hadron Collider (LHC)

The Large Hadron Collider (LHC) is a particle accelerator that utilizes a circular tunnel with a circumference of 27 kilometers to accelerate beams of protons or heavy

ions to high energies and collide them at four separate experimental locations. The LHC operates on the principle of accelerating these beams to nearly the speed of light through a series of superconducting magnets and then directing them to collide with each other at specific points along the circular path.

The LHC's superconducting magnets are cooled to temperatures close to absolute zero (-271.3 degrees Celsius) to maintain their superconducting state, allowing them to guide and focus the particle beams as they travel along the circular path. These magnets produce a strong magnetic field that keeps the particle beams on their circular trajectory and causes them to bend as they pass through the magnetic field. By adjusting the strength of the magnetic field, the LHC can control the curvature of the particle beams and ensure that they collide at the designated interaction points.

The LHC's acceleration process occurs in a series of stages, starting with a source of particles that are injected into a linear accelerator (LINAC). The LINAC accelerates the particles to an energy of a few million electronvolts (MeV) before passing them to a circular accelerator called a Booster. The Booster further accelerates the particles to an energy of 1.4 billion electronvolts (GeV) before injecting them into the Proton Synchrotron (PS).

The PS is a circular accelerator that increases the energy of the particles to 25 GeV before injecting them into the Super Proton Synchrotron (SPS). The SPS is a larger circular accelerator that further accelerates the particles to 450 GeV before finally injecting them into the LHC. Once inside the LHC, the particles are accelerated to their final energy and directed to collide at the designated interaction points.

The collisions at the LHC produce a shower of subatomic particles that are captured and analyzed by the LHC's four primary detectors: ATLAS, CMS, LHCb, and ALICE. These detectors are designed to measure the properties and trajectories of the particles produced by the collisions and provide valuable insights into the fundamental nature of matter and the universe.

Overall, the operational principle of the LHC is based on the precise control of the particle beams through a series of superconducting magnets and accelerators to produce high-energy collisions that enable cutting-edge research in particle physics.

The LHC tunnel is situated approximately 100 meters underground, in a tunnel that was previously used by the Large Electron-Positron Collider (LEP). It has a diameter of 3.8 meters and houses over 1,600 superconducting magnets. The collider operates for periods of several months at a time, with periods of downtime in between for maintenance and upgrades.

TBA Luminosity, bunches, Van der Meer scans

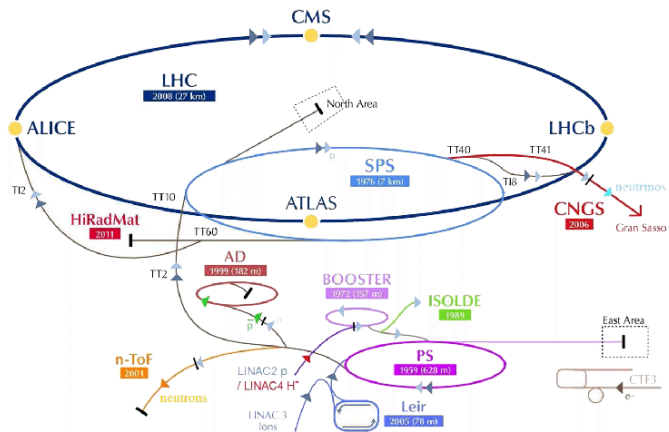


Figure 3.1: TBA.

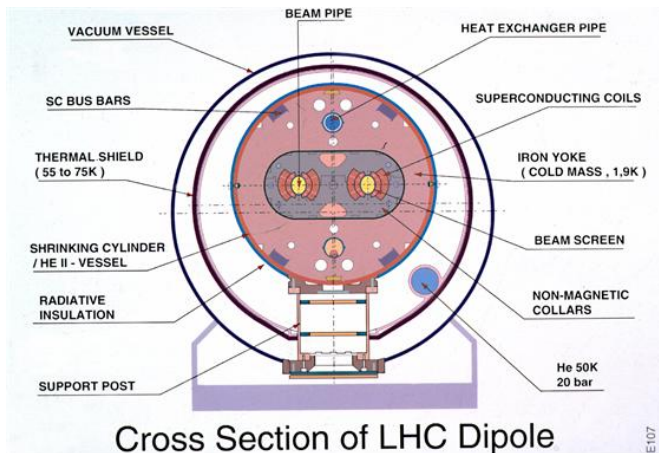


Figure 3.2: TBA.



## Chapter 4

# The ALICE Detector



## Chapter 5

# Events, Vertices, Tracks, and Particles

Lorem ipsum dolor sit amet, consectetuer adipiscing elit. Etiam lobortis facilisis sem. Nullam nec mi et neque pharetra sollicitudin. Praesent imperdiet mi nec ante. Donec ullamcorper, felis non sodales commodo, lectus velit ultrices augue, a dignissim nibh lectus placerat pede. Vivamus nunc nunc, molestie ut, ultricies vel, semper in, velit. Ut porttitor. Praesent in sapien. Lorem ipsum dolor sit amet, consectetuer adipiscing elit. Duis fringilla tristique neque. Sed interdum libero ut metus. Pellentesque placerat. Nam rutrum augue a leo. Morbi sed elit sit amet ante lobortis sollicitudin. Praesent blandit blandit mauris. Praesent lectus tellus, aliquet aliquam, luctus a, egestas a, turpis. Mauris lacinia lorem sit amet ipsum. Nunc quis urna dictum turpis accumsan semper.



## **Part III**

# **Author's measurements**



# Chapter 6

## Reconstruction of neutral strange particles with ALICE

Hadrons  $K_S^0$  and  $\Lambda$  ( $\bar{\Lambda}$ ) are unstable neutral primary particles that usually decay within the volume of the detector through the weak interaction. Their mean lifetimes are  $\sim 2.7 \text{ cm}/c$  and  $\sim 7.9 \text{ cm}/c$ , respectively.<sup>2</sup> Their dominant decay channels, which are also used for their measurement, are:



Because of how these hadrons' decay topologies appear in the detector (an undetectable neutral particle decaying into a V-shaped pair of detectable tracks), they are commonly nicknamed  $V^0S^1$ .

### 6.1 Analysed datasets

TBA Description of data, collection years, some QA Monte Carlo The Monte Carlo data are simulated using a physics event generator (in this measurement, Pythia 8) and a model describing the propagation of particles through the detector environment (GEANT).

---

<sup>1</sup>Not to be confused with V0A and V0C—the forward calorimeters in ALICE, or V0M—the related multiplicity estimator using the calorimeters' signal.

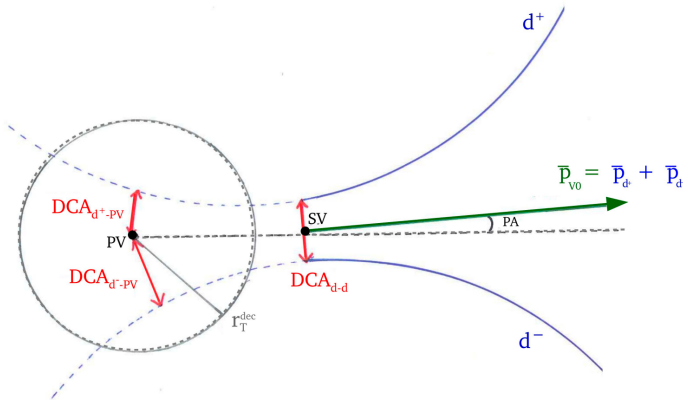


**Figure 6.1:** Typical topology of  $V^0$  decay. PV stands for primary vertex, SV for secondary vertex. p. 102

## 6.2 Identification of $V^0$ s using ALICE

A centrally developed ALICE algorithm, the ALICE  $V^0$  finder, is used to collect suitable  $V^0$  candidates from pairs of oppositely charged tracks with the relevant topology. This typical topology is illustrated in Fig. ?? Additional selection criteria (“cuts”) are further applied to suppress the background among those candidates. These include:

- cuts on kinematics of the mother and the daughters,
- constraints on the topology of the decay,
- constraints on the reconstruction quality of the daughter tracks,
- cuts on the specific ionisation energy loss of the daughters,
- rejection of contributions from pile-up using “fast detector” information,
- rejection of other competing  $V^0$  candidates based on their invariant mass.

The full list of used cuts is listed in Tab. 6.1.

## 6.3 Signal extraction

The  $V^0$  signal is separated from the background in distributions of  $M_{\text{inv}}$  in several  $p_T$  intervals using the so-called sideband method. Assuming the signal peaks around  $\Delta m_{V0} = M_{\text{inv}} - M_{V0} = 0$  and approximating the background in this region as linear, the subsequent procedure is followed:

**Table 6.1:** Cuts used in the identification of the  $K_S^0$ ,  $\Lambda$ , and  $\bar{\Lambda}$  particles.

Cut Variable	Cut Value for $K_S^0$ ( $\Lambda$ , $\bar{\Lambda}$ )
Topology	
$V^0$ pseudorapidity	$-0.8 < \eta < 0.8$
Transverse momentum	$1.0 < p_T < 25.0 \text{ GeV}/c$
$V^0$ DCA	$\text{DCA}^{d-d} < 1.0$
Pointing angle	$\cos \text{PA} > 0.97(0.995)$
Decay radius	$0.5 \text{ cm} < R_{xy}$
Daughter Tracks Selection	
DCA of daughters to PV	$\text{DCA}_{xy}^{\text{d-PV}} > 0.06 \text{ cm}$
TPC PID of daughters	$< 5\sigma$
Track pseudorapidity	$-0.8 < \eta < 0.8$
TPC crossed rows	$N_{\text{cr}} > 70$
TPC crossed rows to findable ratio	$N_{\text{cr}}/N_f > 0.8$
Candidate Selection	
Proper lifetime (transverse)	$(R_{xy} \times m_{(\Lambda, \bar{\Lambda})}/p_T < 30 \text{ cm})$
Competing mass	$> 4\sigma$

- the sideband regions are defined. The  $M_{\text{inv}}$  spectra are fitted in the  $-0.03 < M_{\text{inv}} < -0.03 \text{ GeV}/c^2$  interval using a  $\chi^2$ -fit with the distribution

$$f = [0] + [1] \cdot M_{\text{inv}} + [2] \cdot \mathcal{N}(\mu, \sigma_1^2) + [3] \cdot \mathcal{N}(\mu, \sigma_2^2), \quad (6.4)$$

where  $\mathcal{N}$  is a Gaussian distribution. This is done in all  $p_T$  bins and illustrated in Fig. 6.4.

- In each  $p_T$  bin, parameter  $\sigma$  is obtained as the RMS of  $[2] \cdot \mathcal{N}(\mu, \sigma_1^2) + [3] \cdot \mathcal{N}(\mu, \sigma_2^2)$ . To calculate the RMS, the distribution is sampled  $10^5$  times.
- Variables  $\mu_{V^0}$  and  $\sigma_{V^0}$  as functions of  $p_T$  are interpolated using  $\chi^2$  fit and the parametrisations:

$$\mu_{K_S^0}(p_T) = \begin{cases} [0] + [1] \cdot p_T + [2] \cdot p_T^2 & \text{if } p_T < 1.6 \text{ GeV}/c, \\ [3] & \text{if } p_T \geq 1.6 \text{ GeV}/c, \end{cases} \quad (6.5)$$

$$\mu_{\Lambda, \bar{\Lambda}}(p_T) = \begin{cases} [0] + [1] \cdot p_T + [2] \cdot p_T^2 & \text{if } p_T < 1.9 \text{ GeV}/c, \\ [3] + [4] \cdot p_T & \text{if } p_T \geq 1.9 \text{ GeV}/c, \end{cases} \quad (6.6)$$

$$\sigma_{V^0}(p_T) = [0] + [1] \cdot p_T + \frac{[2]}{p_T}. \quad (6.7)$$

The fitted parametrisations can be seen in Fig. 6.3.

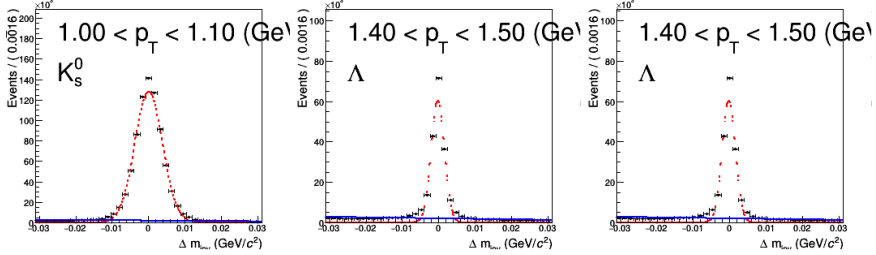


**Figure 6.2:** Determination of the signal peak mean and width using a fit of the Gaussian distribution for  $K_S^0$ ,  $\Lambda$ , and  $\bar{\Lambda}$  particles.

4. In each  $p_T$  bin, we define the signal region  $N$  as  $(\mu_{V0} - 6\sigma_{V0}; \mu_{V0} + 6\sigma_{V0})$  and the sidebands  $A$  and  $B$  as  $(\mu_{V0} - 12\sigma_{V0}; \mu_{V0} - 6\sigma_{V0})$  and  $(\mu_{V0} + 6\sigma_{V0}; \mu_{V0} + 12\sigma_{V0})$ . In these regions, we sum together the entries and acquire  $N, A, B$ . The choice of  $6\sigma_{V0}$  is rather liberal to avoid biases from incorrect determination of the  $\mu_{V0}$  or the imperfect description of the signal peak width  $\sigma_{V0}$
5. Since the background is assumed to be linear, the sum of the two sideband integrals is an accurate estimation of the background in the signal region. Particle yields  $Y$  and the corresponding statistical uncertainties  $\sigma_Y$  are calculated as

$$Y = N - A - B \quad (6.8)$$

$$\sigma_Y = \sqrt{N + A + B} , \quad (6.9)$$

due to the fact that the statistical uncertainties in the signal and sideband regions are fully uncorrelated. Illustrations of this step can be seen in Fig. ??.

### 6.3.1 Validation using simulations

The accuracy of the sideband method is tested with “MC closure”—in MC simulated data, the  $p_T$ -spectra acquired blindly from the  $V^0$  candidates are compared with  $p_T$ -spectra of identified  $V^0$ . The ratios can be seen in Fig. ?? and show a  $\sim 5\%$  effect at high- $p_T$ . This is caused by the fact that in ALICE MC simulations, the  $V^0$  mass peaks have somewhat longer tails than in data and thus the signal can enter the background regions. This has to be taken into account when defining reconstruction efficiency using MC data.

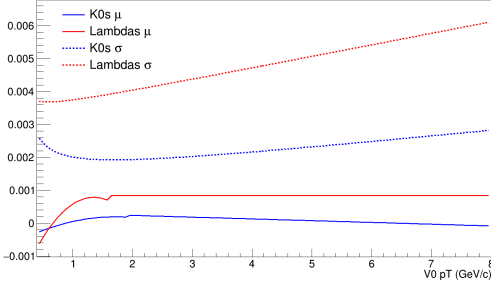


**Figure 6.3:** Parametrisation of the signal peak mean and width as a function of  $p_T$ .

### Alternative approach

Originally, methods involving a likelihood fit and an unbinned likelihood fit of two Gaussian distributions as well as other background descriptions were tested. However, although more sophisticated, these methods proved considerably less precise. This is due to the fact that the signal peaks cannot be accurately described by the two Gaussian distributions, particularly in highly populated  $p_T$  bins. That said, they are sufficient to determine the  $\sigma_{V^0}$  for above-stated purposes.

### Mass resolution of secondary $\Lambda$ and $\bar{\Lambda}$ particles

Approximately 20% of the  $\Lambda$  yields measured are produced as secondary particles coming from decays of the  $\Xi$  baryon in most cases – also called feeddown. Investigations of the simulated data revealed that the invariant mass of these secondaries suffers from a worse resolution (ca. 3 times higher  $\sigma$ ). Subsequently, this gives our signal extraction a ca. 75% efficiency for secondaries, and ca. 95% efficiency for inclusive  $\Lambda$  yields at intermediate  $p_T$ . This has to be taken into consideration when calculating corrections for the feeddown yields. This effect can be seen in Fig. 6.5.

## 6.4 Normalisation

The reconstructed  $K_S^0$ ,  $\Lambda$ , and  $\bar{\Lambda}$  yields  $Y(\eta, p_T)$  are normalised according to

$$\frac{d^2N^{\text{raw}}}{dydp_T} = \frac{1}{N_{\text{ev}}} \frac{1}{J} \frac{1}{\Delta\eta} \frac{1}{\Delta p_T} Y(\eta, p_T) \quad , \quad (6.10)$$

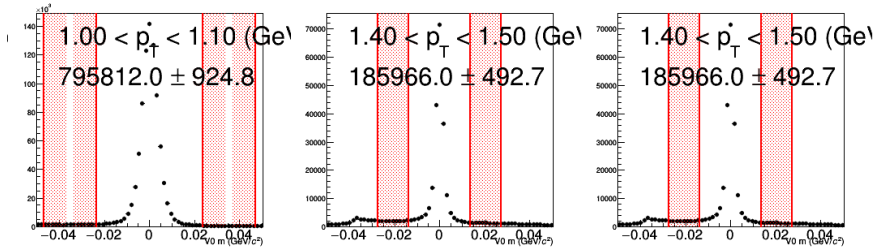


**Figure 6.4:** Visualisation of the sideband regions, from which the background is estimated, for  $K_S^0$ ,  $\Lambda$ , and  $\bar{\Lambda}$  particles.

where  $N_{\text{ev}}$  is the number of selected events,  $J$  the Jacobian of the  $\eta \rightarrow y$  transformation, and  $\Delta\eta$  and  $\Delta p_T$  the widths of the pseudorapidity and transverse momentum intervals, respectively.

TBA Jacobian

TBA Event loss correction

## 6.5 Corrections to the reconstructed production

To acquire results with scientific relevance, the raw yields of  $V^0$ s observed with ALICE need to be corrected for geometrical acceptance, detector effects, and, in the case of  $\Lambda$  ( $\bar{\Lambda}$ ), also for secondary contribution.

### 6.5.1 Secondary contribution correction

Only ca. 80% of the measured inclusive  $\Lambda$  and  $\bar{\Lambda}$  yields are produced directly in the pp collision or near-instantaneously in non-weak decays of resonances, as primary particles. The remainder is produced secondarily, as products of weak decays of heavier baryons. The dominant, and the only relevant, reactions are:

$$\Xi^- \rightarrow \Lambda \pi^- , \quad (6.11)$$

$$\Xi^0 \rightarrow \Lambda \pi^0 , \quad (6.12)$$

$$\Xi^+ \rightarrow \bar{\Lambda} \pi^+ , \quad (6.13)$$

$$\bar{\Xi}^0 \rightarrow \bar{\Lambda} \pi^0 . \quad (6.14)$$

For the  $K_S^0$ , the secondary production (such as from  $\phi$  mesons) is negligible.

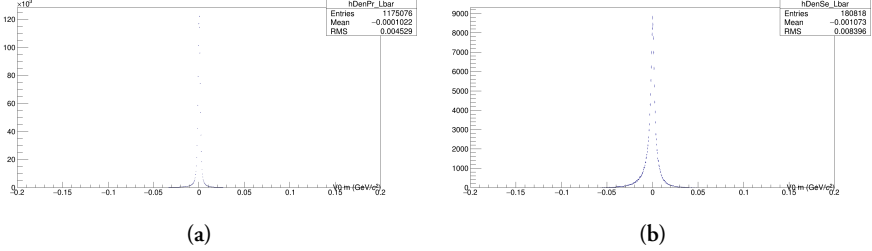


**Figure 6.5:** TBA.

The primary  $\Lambda$  yields can be estimated using the following equation,

$$\Lambda^{\text{raw}}(p_T^i) = \Lambda_{\text{measured}}^{\text{raw}} - \Lambda_{\text{secondary}}^{\text{raw}} \quad (6.15)$$

$$= \Lambda_{\text{measured}}^{\text{raw}} - \sum_j F_{ij}^{\Lambda} \int_{p_T^j} dN \frac{dN}{dp_T}(\Xi^-) \quad , \quad (6.16)$$

where  $F_{ij}$  is the so-called feeddown matrix giving the probabilities of a produced  $\Xi^-$  or  $\Xi^0$  particle in a  $p_T$  interval  $j$  decaying into reconstructed  $\Lambda$  in a  $p_T$  interval  $i$ , and  $\frac{dN}{dp_T}(\Xi^-)$  the measured  $\Xi^-$  spectra. This approach assumes that the  $\Xi^0$  decay contribution is identical to  $\Xi^-$  and is used because  $\Xi^0$  baryons are challenging to measure. For the  $\bar{\Lambda}$ , the equation is analogous but uses  $\Xi^+$ .

The feeddown matrix is calculated in ALICE MC simulations of MB events,

$$F_{ij}^{\Lambda} = 2 \cdot \frac{N_{\text{rec.}}(\Lambda)|_{p_T^{\Lambda}=i}^{p_T^{\Xi}=j}}{N_{\text{gen.}}(\Xi)|_{p_T^{\Xi}=j}} \quad , \quad (6.17)$$

where  $\Xi$  represent both  $\Xi^-$  and  $\Xi^0$ . There is an assumption that the probabilities, and thus, the matrix, do not depend on multiplicity of the event. It is taken into account in systematic uncertainties.

An alternative approach is constructing  $F_{ij}^{\Lambda}$  from charged  $\Xi$  solely, and then multiplying  $\Lambda_{\text{secondary}}^{\text{raw}}$  by two and was used to determine the systematic uncertainty.

As discussed previously, due to the worse mass resolution of secondary  $\Lambda$ , a  $M_{\text{inv}}$  cut of  $5\sigma_{V0}$  (determined in the sideband definition procedure). Since a large amount of the secondaries enter the background regions, a negative weight  $-1$  has to be applied to achieve the best MC closure validation. Other configurations ( $6\sigma_{V0}$  and  $-1$  weight,  $4\sigma_{V0}$  and  $0$  weight) were also tested.

The feeddown matrices  $F_{ij}^{\Lambda}$ ,  $F_{ij}^{\bar{\Lambda}}$  are displayed in Fig. 6.6.

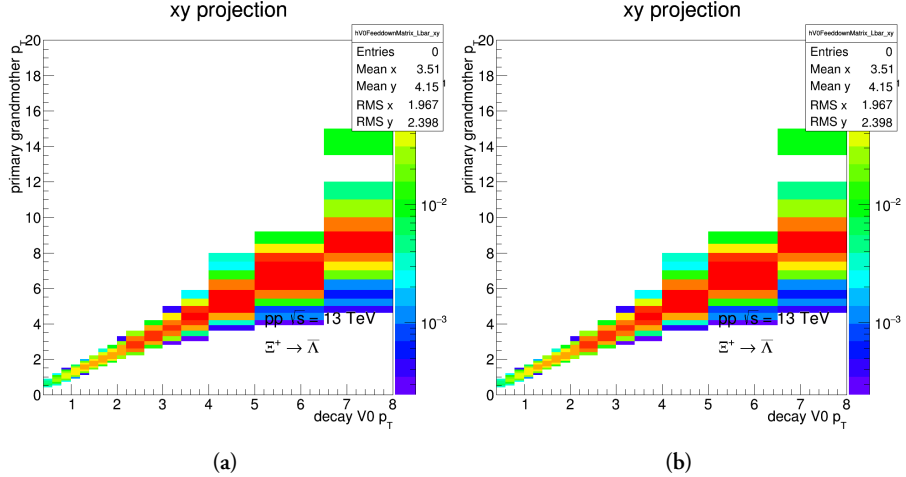


Figure 6.6: Feeddown matrices (a)  $F_{ij}^\Lambda$  and (b)  $F_{ij}^{\bar{\Lambda}}$  from  $\Xi$  baryons.

## $\Xi$ spectra

Fitting. TBA

### 6.5.2 Reconstruction efficiency

The total reconstruction efficiency, including the acceptance, for  $V^0$ s in our events with ALICE can be determined using the Monte Carlo simulated data. It is calculated as

$$\epsilon(p_T) = \text{acceptance} \times \epsilon_{\text{rec}} \quad (6.18)$$

$$= \frac{\# \text{ associated reconstructed } V^0\text{s}}{\# \text{ generated } V^0\text{s within } |\eta| < 0.8}, \quad (6.19)$$

in events that passed the selection criteria. The association is done by comparing the mother's and daughters' PDG ID as well as the MC generator label. Particles in the numerator have to satisfy all selection cuts. The reconstruction efficiency for  $K_S^0$ ,  $\Lambda$ , and  $\bar{\Lambda}$  is plotted in Fig. 6.8.

As mentioned before, in ALICE simulations, the  $M_{\text{inv}}$  resolution worsens with increasing  $p_T$ ; in high- $p_T$  bins, the simulated  $V^0$ s are sometimes reconstructed with higher  $M_{\text{inv}}$  than what is considered realistic. This would lead to a lower efficiency as those  $V^0$ s can fall out of the signal region, and an overestimation of the total measured spectra. For this reason, a  $4\sigma_{V^0}$  cut is required for the  $V^0$ s  $M_{\text{inv}}$  in the numerator.

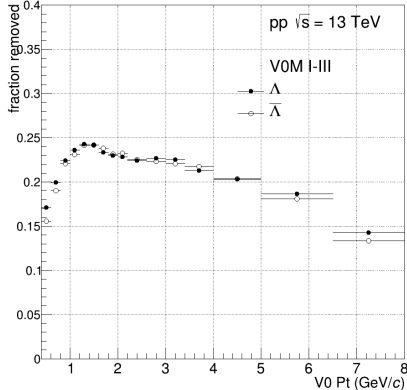


**Figure 6.7:** TBA.

Alternatively, one could use a cut of  $6\sigma_{V^0}$  and applying a negative weight  $-1$  in cases where it is not satisfied.

The reconstruction efficiency is defined in MB events, assuming the reconstruction in pp collisions does not largely depend on multiplicity, geometrical event classification, or event sub-structure. This assumption is taken into account in systematic uncertainties.

## 6.6 Transverse momentum spectra

Using the corrections on the normalised yields, one acquires the measured transverse momentum spectra, which are comparable with production cross sections and thus theoretical predictions.

$$\frac{d^2N}{dydp_T} = \epsilon(p_T) \times \frac{d^2N_{\text{primary}}^{\text{raw}}}{dydp_T} \quad (6.20)$$

### 6.6.1 Comparisons with previously published results

The acquired results were tested against previously published measurements of  $K_S^0$ ,  $\Lambda$ , and  $\bar{\Lambda}$  transverse momentum spectra at the ALICE experiment in MB as well as high-multiplicity (V0M I and V0M III) events in pp collisions at  $\sqrt{s} = 13$  TeV.

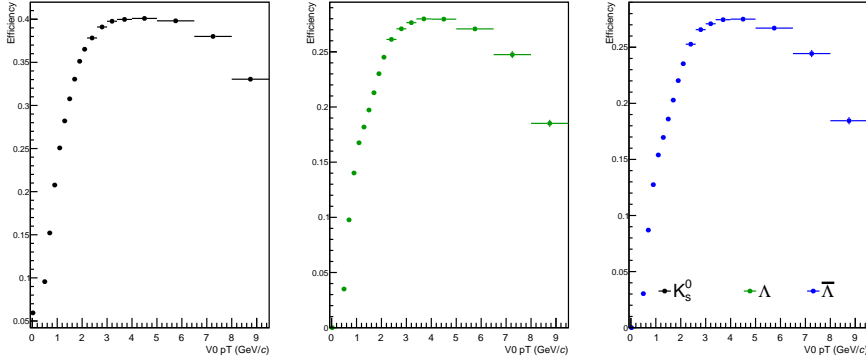


**Figure 6.8:** TBA.

$$K_S^0$$

The published  $K_S^0$  results were measured in kINT7 events. Thus, in order to compare on an equal footing, a trigger efficiency scaling factor  $\epsilon_{\text{trig}} = 0.7448$ , taken over from, was applied to this analysis.

The comparison of this analysis to the published results can be seen in Fig. 6.9a. In high-multiplicity events, the spectra are in a good agreement across the entire  $p_T$  range (most points lie within  $\sim 5\%$  difference). In MB events, there is a difference ( $\sim 10\%$ ) at the lowest  $p_T$  values. This is understood as a loss of signal in events with no reconstructed charged tracks and is usually corrected for. Since the correction plays a role only in MB – events which are of little interest to this thesis' work – it is not taken into account.

$$\Lambda + \bar{\Lambda}$$

The published  $\Lambda + \bar{\Lambda}$  results were measured in same events as this analysis, ( $\text{INEL} > 0$ ), therefore,  $\epsilon_{\text{trig}}$  was not applied. They are compared to this analysis in Fig. 6.9b and show a satisfactory agreement (most points lie within  $\sim 5\%$  difference).

## 6.7 Systematic uncertainties

Experimentally measured values always come with uncertainties – statistical and systematic. Whereas statistical uncertainties are caused by the limited number of measurements and can be decreased by increasing the statistical sample analyzed, system-

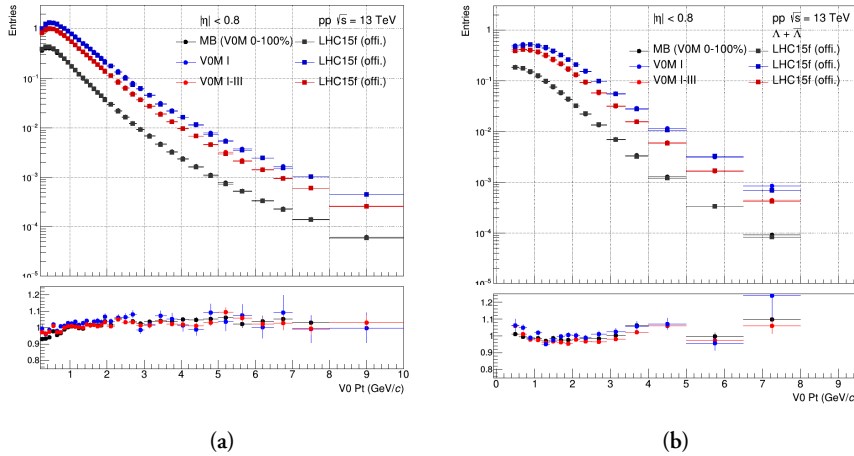


**Figure 6.9:** Cross-checks of this analysis'  $p_T$  spectra of (a)  $K_S^0$  and (b)  $\Lambda + \bar{\Lambda}$  in MB, VOM I, and VOM I-III events in pp collisions at against  $\sqrt{s} = 13$  TeV results previously published by ALICE.

atic uncertainties represent the imprecision or the bias of the experimental methodology itself. Calculation of statistical uncertainties is given directly from frequentist statistics. Definition of systematic uncertainties, however, is not always straightforward – one cannot simply re-do the measurement with several completely different experimental setups and data analysis techniques. Therefore, a lot of effort needs to go into identifying all possible sources of systematic uncertainties.

In this measurement, the following sources of systematic uncertainty were identified as relevant:

- **Variation of selection criteria**

In determining the reconstruction efficiency, it is assumed that in ALICE MC simulations, all observables used for the identification of  $V^0$ s and for assuring the quality of daughter tracks represent reality. Their inaccurate description, however, results in a bias. This bias is estimated by testing the sensitivity of the final results to varying the selection criteria on these observables.

- **Signal extraction method**

The biases of the sideband background estimation procedure are tested against increasing and reducing the signal and background regions, by varying the number of  $\sigma_{V^0}$ . Variations of 5 and 7  $\sigma_{V^0}$  were used.

- **Multiplicity dependence of  $\epsilon(p_T)$**

Studies of the reconstruction efficiency in pp collisions reveal a small, albeit

significant dependence on the collision final state. A constant uncertainty of  $\sim 2\%$  is applied on the spectra to account for this.

- **Feeddown correction**

Three sources of uncertainty on the contribution of secondary particles were identified – variation of the  $\Xi$  yields, multiplicity dependence of the feeddown matrix, and an alternative method.

- **Material budget**

This uncertainty reflects that implementing ALICE’s material composition in simulations comes with limitations. Previous studies in ALICE which varied parameters of the description of the apparatus showed that this effect corresponds to a constant 4% uncertainty on the measured spectra.

When testing the default method  $A$  against an alternative method  $B$ , one can implement the deviation of the ratio of their measured values  $\Delta = B/A$  from unity as an uncertainty. To ensure that this difference is statistically significant and not just an effect of a limited data sample, the deviation is considered only if it exceeds its own uncertainty, defined as

$$\sigma_\Delta = \frac{\sqrt{|\sigma_B^2 - \sigma_A^2|}}{A} , \quad (6.21)$$

where  $\sigma_A$  and  $\sigma_B$  are the uncertainties of the results from methods  $A$  and  $B$ , respectively.

### 6.7.1 Variation of selection criteria

To investigate the differences between description of variables in measured data and ALICE simulations, and determine sensible cut variations  $\lambda_i$ , raw yield loss  $F$  was studied. It was measured in MB events and defined as

$$F(\lambda) = 1 - \frac{Y(\lambda)}{Y(\lambda_0)} , \quad (6.22)$$

where  $Y(\lambda)$  is the raw yield as a function of the cut value  $\lambda$  and  $\lambda_{\text{LOOSEST}}$  the loosest variation (corresponding to the highest yield).

For most observables, the systematic effect can be estimated from alternative methods using  $\lambda_{\text{LOOSEST}}$  and  $\lambda_{\text{TIGHTEST}}$ . To ensure the stability and possible non-linearity, less strict  $\lambda_{\text{LOOSE}}$  and  $\lambda_{\text{TIGHT}}$  are also tested. If applicable it is reasonable to choose  $\lambda_i$  such that  $F(\lambda_i)$  does not exceed approximately 10%.

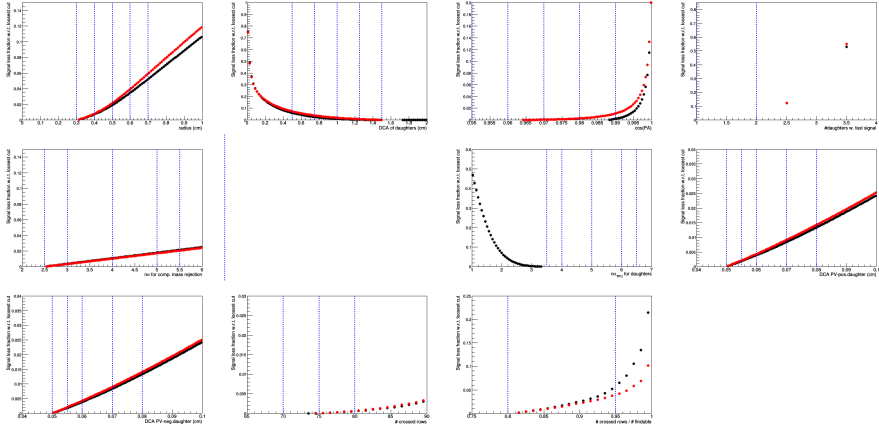


**Figure 6.10:** TBA

The  $F(\lambda)$  for the different selection criteria, and with the chosen  $\lambda_i$  are shown in Fig. 6.10, Fig. 6.11, and Fig. 6.12 for  $K_S^0$ ,  $\Lambda$ , and  $\bar{\Lambda}$ , respectively. The pile-up rejection cut, which requires “fast detector” information for at least one daughter is of a binary nature. So, its variation was tested by requiring a different amount of “fast detector” hits between the two daughters. The selected values of  $\lambda_i$  are summarised in Tab. 6.2.

**Table 6.2:** Cut variation parameters for the  $K_S^0$  ( $\Lambda$  and  $\bar{\Lambda}$ ).

Quality	loosest	loose	default	tight	tightest
radius	0.3	0.4	0.5	0.6	0.7
DCA between daughters	1.5	1.25	1.0	0.75	0.5
cos PA	0.95 (0.993)	0.96 (0.994)	0.97 (0.995)	0.98 (0.996)	0.99 (0.997)
pile-up removal cut	-	-	1	2	-
comp. mass number of $\sigma$	2.5	3.0	4.0	5.0	5.5
lifetime	-	(35.0)	(30.0)	(25.0)	-
TPC PID number of $\sigma$	6.5	6.0	5.0	4.0	3.5
DCA to PV of pos. track	0.05	0.055	0.06	0.07	0.08
DCA to PV of neg. track	0.05	0.055	0.06	0.07	0.08
TPC crossed rows	-	-	70	75	80
TPC find. ratio	-	-	0.8	0.95	-

## 6.7.2 Feeddown correction

As mention before, first, the  $\Xi$  spectra, from which the feeddown is calculated, are varied within their reported uncertainties. In both variations, the yields are then extracted using a fit. Second, similarly to  $\epsilon(p_T)$ , the assumption of no multiplicity

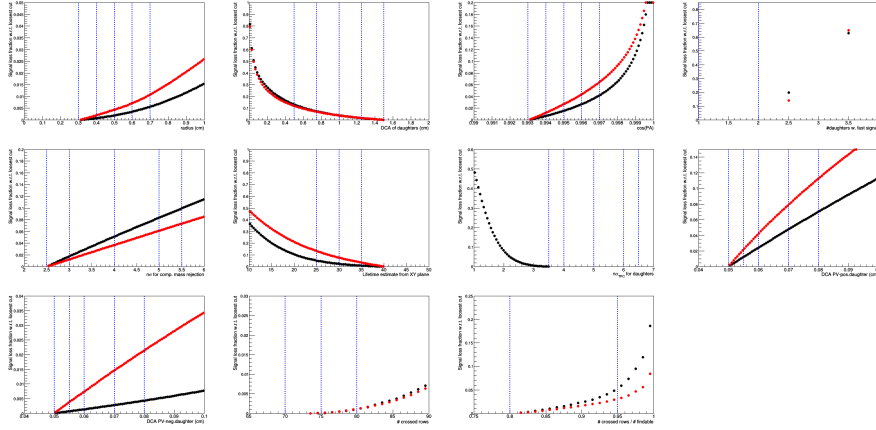


**Figure 6.11: TBA**

dependence of the feeddown matrix is accompanied by a constant uncertainty of 2% on the secondary yields (corresponding to ca. 0.6% uncertainty on the primary yields).

Lastly, an alternative method of estimating the feeddown just from charged  $\Xi$  baryons, and multiplying by a factor of two, was also tested and contributes a systematic uncertainty. It is considered significant and applied when  $|\Delta - 1| > \sigma_\Delta$ . The difference between the two methods can be seen in Fig. 6.13. It should be noted that whilst the secondary yields suffer from a rather large systematic uncertainty, the effect on the primary spectra is significantly smaller, as the uncertainties enter as  $\frac{1-B}{1-A}$  and the secondary yields do not exceed  $\sim 30\%$ .

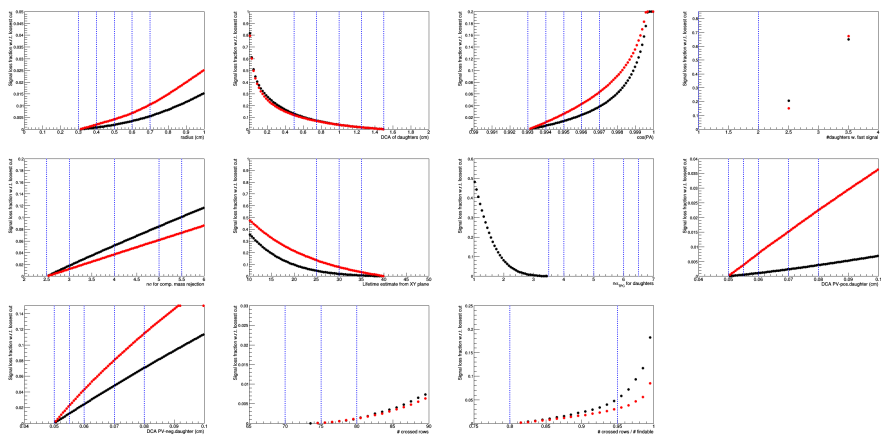


**Figure 6.12:** TBA

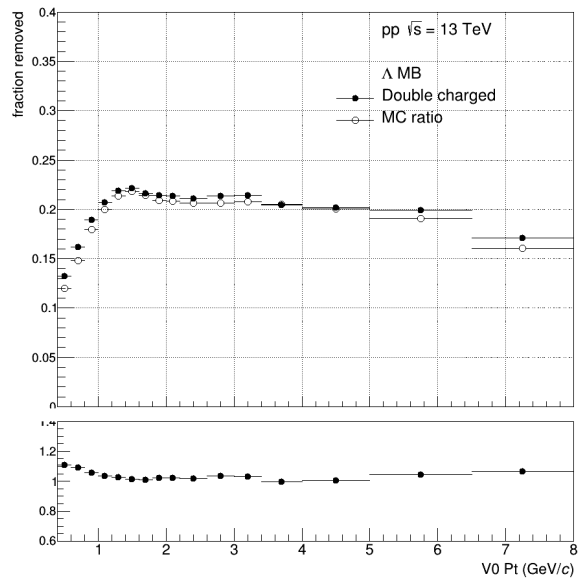


**Figure 6.13:** TBA



# Chapter 7

## Transverse Spherocity

In this chapter, measurements of  $K_S^0$ ,  $\Lambda$ , and  $\bar{\Lambda}$  are reported as a function of transverse spherocity  $S_O^{(p_T=1.0)}$ , a measure of the event's topology in the transverse  $xy$ -plane.

### 7.1 Transverse spherocity

#### 7.1.1 Motivation for studying event topology

As explained in Chapter X, there is overwhelming evidence that some phenomena associated with QGP, such as collective flow and strangeness enhancement, also arise in pp and p–A collisions at LHC energies and high event multiplicities. This challenges the conventional assumption that the hadron densities and densities of colour fields between partons are too low to interact with each other. Consequently, high-multiplicity pp (and p–A) collisions cannot be treated as a superposition of mostly independent parton-parton (or parton-hadron) scatterings and a more in-depth approach is required to fully understand these phenomena.

Event shape observables have been used historically in lepton experiments to study fundamental QCD properties such as the gluon spin? , and also at Tevatron and the LHC in events with very high  $p_T$  ( $\gtrsim 100$  GeV/c) jets to further test pQCD predictions? . There are various observables, including sphericity  $S_T$ , spherocity  $S_O$ , thrust  $T$ , F-parameter, and Ellis-Karliner angle, most of which are collinear- and infrared-safe and therefore moderately easily calculable? . An illustration of two events with different topologies and calculated values of selected observables can be seen in Fig. 7.1.

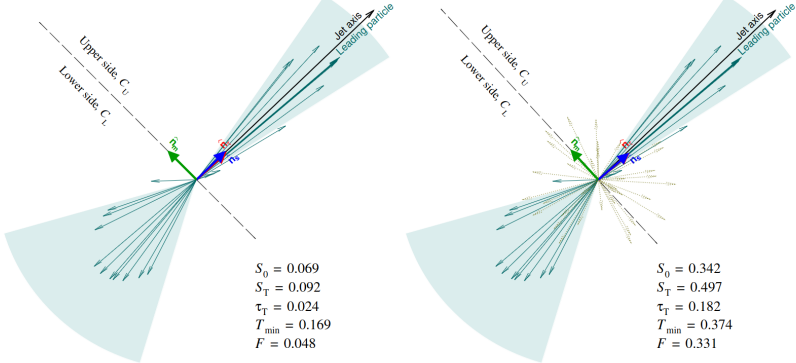


**Figure 7.1:** TBA.

With the discoveries of QGP phenomena in high-multiplicity collisions of small systems, event shape observables become attractive for different reasons. This is because pQCD (“hard”) processes are responsible for a significant fraction of particle production and are likely to impact the character of QGP phenomena in non-trivial ways. The role of non-perturbative (“soft”) processes is particularly interesting to study as their mechanisms are not fully understood and their interpretation relies on phenomenological models that require clear experimental measurements with high discriminatory power.

Event shape observables allow us to quantify events according to the dominant contributing processes. For instance, collisions with single large  $p_T$  transfer scatterings are likely to lead into events with two back-to-back, highly collimated showers, which create a pencil-like shape in the transverse plane. Conversely, collisions with multiple lower  $p_T$  transfer partonic interactions will exhibit a high degree of azimuthal isotropy. Therefore, event shape measurements help us gain a deeper understanding of high-multiplicity events and a better control over the magnitudes of the hard and soft contributions. Ultimately, these measurements may help determine whether QGP formation is necessary in small systems or uncover new physical behaviours.

### 7.1.2 $S_O$ and $S_O^{(p_T=1.0)}$ as experimental observables

Traditionally, spherocity  $S_O$  is defined as:

$$S_O = \frac{\pi^2}{4} \min_{\hat{n}} \left( \frac{\sum_i |p_{T,i} \times \hat{n}|}{\sum_i |p_{T,i}|} \right)^2 , \quad (7.1)$$

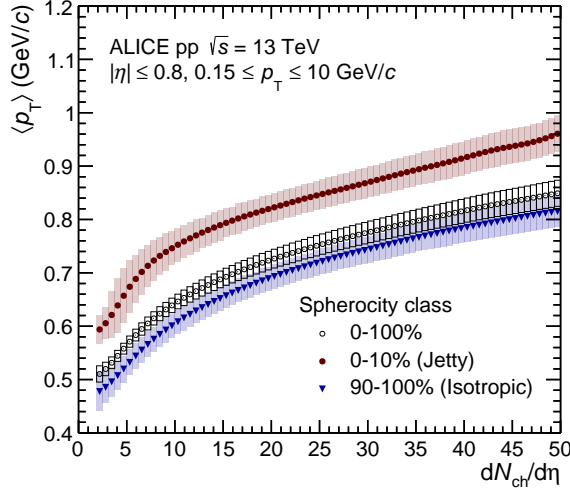


**Figure 7.2:** TBA.

where  $p_{T,i}$  represents the vector of transverse momentum of a particle  $i$  and  $\hat{n}$  is the event-dependent unit vector that minimises the sum. The sum runs over all charged particles in the event within the detector acceptance.

Previous ALICE measurements? studied characteristics of charged particles in pp collisions and discovered their strong dependence of  $\langle p_T \rangle$  on spherocity  $S_O$ , which validates the previously discussed motivation. This relationship is shown in Fig. 7.2. Additionally, phenomenological studies of  $S_O$  in Pythia 8 further demonstrate its classifying power by finding strong dependence of  $\langle n_{MPI} \rangle$  as well as the mean number of reconstructed jets  $\langle n_j \rangle$  on  $S_O$ ?? . These results can be seen in Fig. 7.3.

This work uses a modified definition of this observable, *unweighted* transverse spherocity  $S_O^{(p_T=1.0)}$ , defined as follows:

$$S_O^{(p_T=1.0)} = \frac{\pi^2}{4} \min_{\hat{n}} \left( \frac{\sum_i |\hat{p}_{T,i} \times \hat{n}|}{N_{trks}} \right)^2 , \quad (7.2)$$

where  $\hat{p}_{T,i}$  represents the *unit* vector of transverse momentum of a particle  $i$  and  $N_{trks}$  the number of charged particles entering the sum.

In this thesis, unless stated otherwise, the terms transverse spherocity and spherocity are both used to refer to this unweighted transverse spherocity  $S_O^{(p_T=1.0)}$ .

Applying the spherocity  $S_O^{(p_T=1.0)}$ , events in two geometrical limits can be studied:

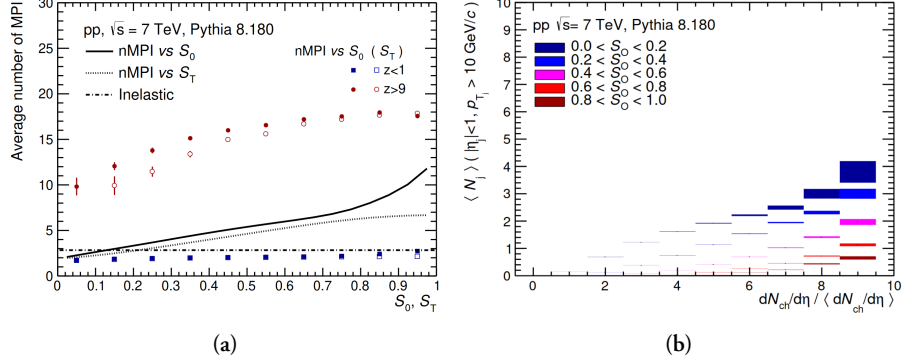


Figure 7.3: TBA.

- $S_O^{(p_T=1.0)} \rightarrow 0$  : the “jetty” limit. Pencil-like topology is selected. These events are dominated by hard pQCD processes. In this limit, with perfectly collimated back-to-back particles,  $\hat{n}$  coincides with them. Thus, the sum of vector products in Eq. 7.2 contains only zero values as  $\sin 0 = \sin \pi = 0$ .
- $S_O^{(p_T=1.0)} \rightarrow 1$  : the “isotropic” limit. Circular topology is selected. Such events are dominated by multiple softer non-perturbative processes<sup>1</sup>. In this limit of  $N \rightarrow \infty$  uniformly distributed unit vectors within  $(0, 2\pi)$ , the choice of  $\hat{n}$  becomes arbitrary and calculation of the sum in Eq. 7.2 leads to:

$$\frac{1}{N} \sum_{n=1}^N \left| \sin \frac{2\pi n}{N} \right| \approx \frac{1}{N} \int_0^N \left| \sin \frac{2\pi x}{N} \right| dx \quad (7.3)$$

$$= \frac{2}{N} \int_0^{N/2} \sin \frac{2\pi x}{N} dx = \frac{1}{\pi} \int_0^\pi \sin u du \quad (7.4)$$

$$= \frac{1}{\pi} [-\cos x]_0^\pi = \frac{2}{\pi} \quad (7.5)$$

and therefore  $S_O^{(p_T=1.0)} = 1$ .

Figure 7.4 illustrates how sphericity slowly approaches the circular limit value with increasing  $N$  compared to other event shape observables. This property makes sphericity favoured by experimentalists in these measurements, as it provides the highest discrimination power of isotropic events? .

---

<sup>1</sup>However, it is important to mention that anisotropic collective flow such as  $v_2$ , a non-perturbative phenomenon, reduces the event isotropy.

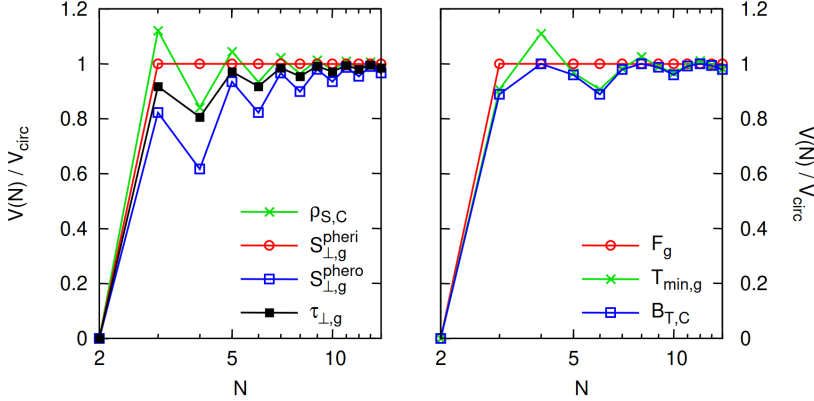


**Figure 7.4:** Graphs showing how rapidly the different event shape observables approach the circular limit  $V_{\text{circ}}$  corresponding to  $N \rightarrow \infty$ , based on the number of perfectly isotropically distributed particles  $N$ . Transverse spherocity, here denoted as  $S_{\perp,g}^{\text{sphero}}$ , exhibits the slowest rise, and never exceeds unity.?

### 7.1.3 Relationship between $S_O^{(p_T=1.0)}$ and $S_O$

In ALICE, only charged particles are considered when calculating spherocities. This introduces biases when measuring charged and neutral species of hadrons. For instance, even topologically identical events with dominant high- $p_T$  leading  $\pi^+$  and  $\pi^0$  can yield significantly different values of the traditional  $p_T$ -weighted spherocity  $S_O$ , despite being comparable in all relevant aspects. In contrast, unweighted spherocity  $S_O^{(p_T=1.0)}$  offers a more similar quantification of the two events, as shown in Fig. 7.5. However, it should be noted that this modified definition is only applicable to events with many tracks (i.e.,  $N_{\text{trks}} > 10$ ).

In addition, while not a large concern in high-multiplicity collisions? ,  $S_O^{(p_T=1.0)}$  also offers improved resolution compared to  $S_O$ , as the failure to reconstruct a high- $p_T$  track has a smaller impact. Overall,  $S_O$  and  $S_O^{(p_T=1.0)}$  exhibit similar values and interpretations, with a strong correlation between the two, as illustrated in Fig. 7.6.

### 7.1.4 Track and event selection

The measurements are carried out on MB events with  $\text{INEL} > 0$ , requiring at least one hit in the V0A or V0C scintillators and one charged particle reconstructed within  $|\eta| < 1$ . The primary vertex is reconstructed using hits in the SPD and is required to be within 10 cm of the interaction point. The fast read-out time of the SPD allows rejection of out-of-bunch pile-up. In-bunch pile-up is further removed by excluding events with multiple reconstructed vertices. The presented results are based on high-

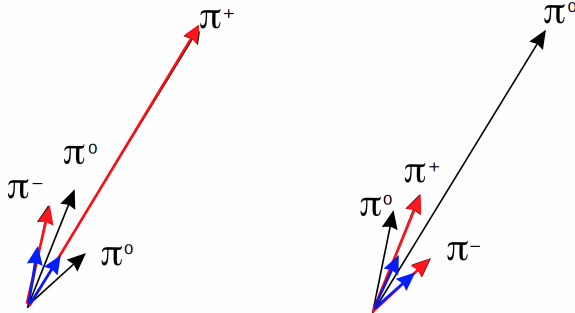


**Figure 7.5:** TBA.

multiplicity events, selected by the classifiers V0M (forward rapidity) and  $N_{\text{tracklets}}^{|\eta| < 0.8}$  (mid-rapidity), and require a minimum of 10 reconstructed tracks within  $|\eta| < 0.8$  and with  $p_T > 0.15 \text{ GeV}/c$ .

To ensure a high level of azimuthal acceptance uniformity, which is important for event shape measurements, the following, rather loose, selection criteria are employed:

1. The SPD is not used due to its holes, at the expense of a lower momentum resolution.
2. A track is required to have at least 50 clusters in the TPC and be matched to hits in the ITS to improve tracking precision and further reject pile-up.
3. DCA cuts are applied in both the longitudinal ( $|\text{DCA}_z| < 3.2 \text{ cm}$ ) and transverse ( $|\text{DCA}_{xy}| < 2.4 \text{ cm}$ ) planes to ensure that the reconstructed TPC track points to the primary vertex.

It should be noted that charged decay products of  $V^0$ s with low  $p_T$  ( $\lesssim 1 \text{ GeV}/c$ ) and small decay radius may enter and influence  $S_O^{(p_T=1.0)}$  determination.

### 7.1.5 Multiplicity selection and its interplay with $S_O^{(p_T=1.0)}$

Spherocity exhibits a twofold correlation with multiplicity that is not particularly informative. First, the definition of  $S_O^{(p_T=1.0)}$  results in higher values for events with more uniformly distributed particles, as shown in Fig. 7.4. Second, in models such as Pythia, high multiplicity is often associated with more MPI, which tend to lead to higher isotropy due to the increased number of emission sources. To gain a more nuanced understanding of the relationship between spherocity and multiplicity, the

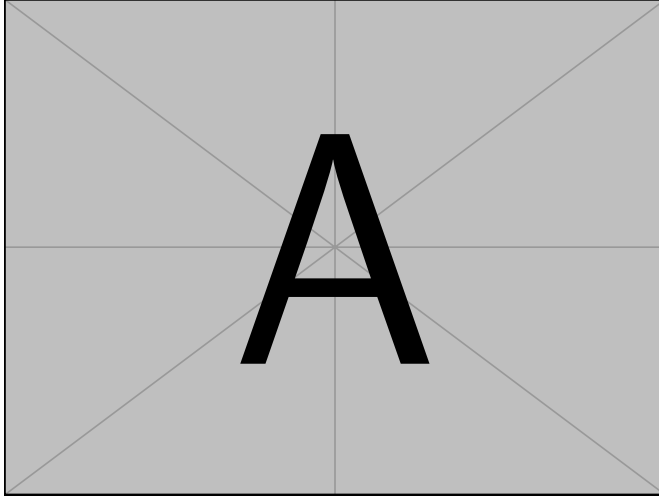


**Figure 7.6:** Correlation between the traditional transverse spherocity  $S_O$  and the unweighted transverse spherocity  $S_O^{(p_T=1.0)}$  employed in this measurement. The results are uncorrected for detector effects.

effect of  $S_O^{(p_T=1.0)}$  on measured particles was analysed in high-multiplicity events determined in two distinct rapidity regions, as described above. Specifically, the top 1% (10%) quantiles are used, denoted as V0M I and  $N_{\text{SPD}_{\text{Trkts}}} \text{ I}$  ( $V0M \text{ I-III}$  and  $N_{\text{SPD}_{\text{Trkts}}} \text{ I-III}$ ).

Figure 7.7 shows the effect of  $S_O^{(p_T=1.0)}$  on the pion yields and  $\langle p_T \rangle$ . Pions are measured in the high-multiplicity events and in top and bottom 10% and 1% quantiles of  $S_O^{(p_T=1.0)}$ . The result reveals that when measuring multiplicity in forward rapidity (V0M I), the effect of  $S_O^{(p_T=1.0)}$  causes a change of approximately 100% in the yields when going from jetty to isotropic limits, whereas the difference in  $\langle p_T \rangle$  is only ca. 10%. Conversely, when determining the multiplicity in mid-rapidity ( $N_{\text{SPD}_{\text{Trkts}}} \text{ I}$ ), the same region where the pion spectra are reconstructed, the change in the yields is only approximately 10% while the change in  $\langle p_T \rangle$  is ca. 25%.

For this reason, the following combinations of multiplicity and  $S_O^{(p_T=1.0)}$  selections are presented:

1.  $N_{\text{SPD}_{\text{Trkts}}} \text{ I}$  and  $S_O^{(p_T=1.0)}$  top and bottom 10% quantiles: This selection emphasises the impact of extreme event topologies on the QCD processes whilst minimising the effect of multiplicity dependence.
2.  $N_{\text{SPD}_{\text{Trkts}}} \text{ I-III}$  and  $S_O^{(p_T=1.0)}$  top and bottom 1% quantiles: This selection shows the effect of even more extreme event topologies but with overall less and somewhat varying multiplicity.

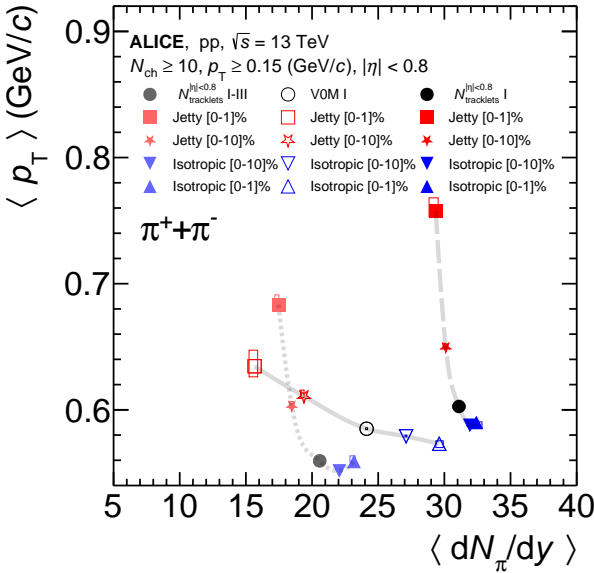
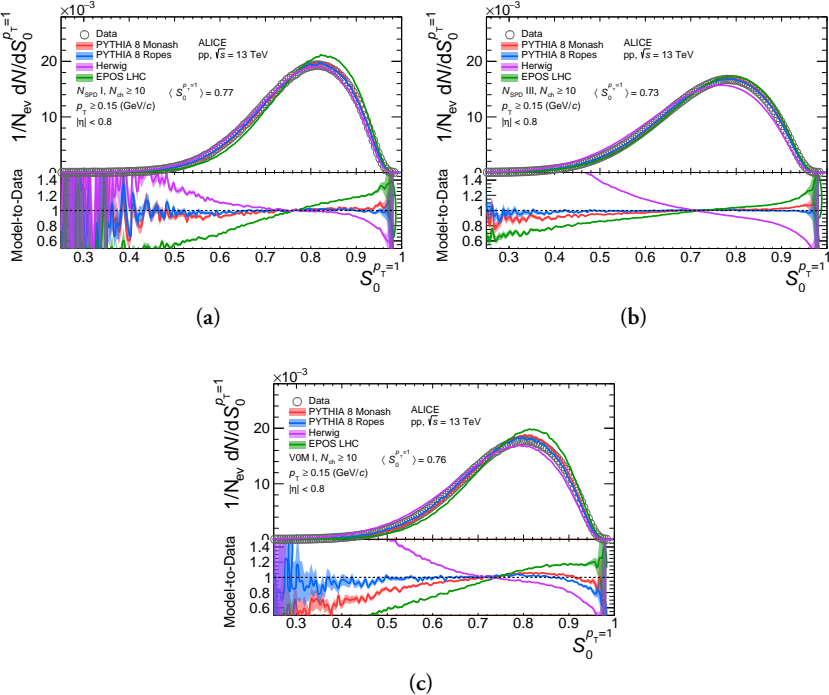


Figure 7.7: TBA.

3. V0M I and  $S_O^{(p_T=1.0)}$  top and bottom 10% quantiles: This selection highlights the effect of extreme event topologies with highly varying mid-rapidity multiplicity. It also allows for a comparison with  $N_{\text{SPD}_{\text{Trkts}}}^{|\eta|<0.8}$  I-III and  $S_O^{(p_T=1.0)}$  1% selection, as the mid-rapidity multiplicity and the  $\langle p_T \rangle$  variations are more similar.

The mid-rapidity multiplicities in the different high-multiplicity classes are reported in Tab. 7.1. The measured  $S_O^{(p_T=1.0)}$  distributions in  $N_{\text{SPD}_{\text{Trkts}}}^{|\eta|<0.8}$  I,  $N_{\text{SPD}_{\text{Trkts}}}^{|\eta|<0.8}$  I-III, and V0M I-III are shown in Fig. 7.8. They are treated with Bayesian unfolding to account for reconstruction effects. They are also compared with theoretical predictions from Pythia 8 (Monash and Ropes tunes), EPOS LHC, and Herwig. Table ?? provides the  $S_O^{(p_T=1.0)}$  cut values associated with the quantile selections in data.



**Figure 7.8:** The measured and fully corrected  $S_0^{(p_T=1.0)}$  distributions for both (a)  $N_{SPD_{Trkts}}$  0–1%, (b) 0–10% and (c) V0M 0–1%. The curves represent different model prediction, where the shaded area represents the statistical uncertainty of the models.

**Table 7.1:** TBA.

Event class	$N_{SPD_{Trkts}}$ I	$N_{SPD_{Trkts}}$ I-III	V0M I
$\langle dN_{ch}/d\eta \rangle$	$33.01 \pm 0.55$	$21.57 \pm 0.32$	$26.02 \pm 0.35$

**Table 7.2:** Values of the different quantiles of the uncorrected  $S_0^{(p_T=1.0)}$  distribution used for the event selections in this analysis.

Event class	$N_{SPD_{Trkts}}$ I	$N_{SPD_{Trkts}}$ I-III	V0M I
Jetty			
$S_0^{(p_T=1.0)}_{0-1\%}$	< 0.487	< 0.408	< 0.433
$S_0^{(p_T=1.0)}_{0-10\%}$	< 0.624	< 0.561	< 0.589
Isotropic			
$S_0^{(p_T=1.0)}_{90-100\%}$	> 0.892	> 0.871	> 0.882
$S_0^{(p_T=1.0)}_{99-100\%}$	> 0.942	> 0.930	> 0.936

### 7.1.6 Comparison of $V^0$ production with MC generators

Further on in this chapter, the results of  $K_S^0$ ,  $\Lambda$ , and  $\bar{\Lambda}$  as a function of  $S_O^{(p_T=1.0)}$  are presented and compared with predictions from phenomenological models Pythia 8, EPOS LHC, and Herwig obtained from MC simulations. To mitigate the effect of reconstruction on the experimental results and make the comparison with these predictions as comparable as possible, the following strategies were employed based on findings using the ALICE MC simulations:

- The results were compared using the same quantiles of the  $S_O^{(p_T=1.0)}$  distributions in both the MC and the data, instead of relying on the experimental  $S_O^{(p_T=1.0)}$  ranges determined by specific cut values. This approach reduced the effects of  $S_O^{(p_T=1.0)}$  resolution.
- In the MC simulations, the  $S_O^{(p_T=1.0)}$  calculations included neutral particles  $K_S^0$ ,  $\Lambda$ , and  $\bar{\Lambda}$ , despite their neutral charge. This helped minimize differences between the true and reconstructed/corrected MC results, possible due to the potential contribution of charged  $V^0$  daughters to the  $S_O^{(p_T=1.0)}$  calculation.

Any discrepancies that still persisted between the true and reconstructed/corrected transverse momentum spectra were accounted for as systematic uncertainties.

## 7.2 Systematic uncertainties

The systematic uncertainties associated with the  $p_T$  spectra of  $K_S^0$ ,  $\Lambda$ , and  $\bar{\Lambda}$  were evaluated separately for  $N_{\text{SPD}_{\text{Trkts}}}$  I and V0M I events with no  $S_O^{(p_T=1.0)}$  selection, as well as for the top and bottom 10% isotropic and jetty quantiles, using the methodology described in Section ???. The relative systematic uncertainties obtained from these configurations were also applied to the  $N_{\text{SPD}_{\text{Trkts}}}$  I-III and V0M I-III event classes with different jetty/isotropic quantiles.

### 7.2.1 Variations in alternative methods

Figures 7.9, 7.10, and 7.11 illustrate the variations resulting from alternative cut values, extraction parameters, or feeddown methods in V0M I,  $S_O^{(p_T=1.0)}$ -unbiased events for  $K_S^0$ ,  $\Lambda$ , and  $\bar{\Lambda}$ , respectively. The maximal deviations, contributing to the final systematic uncertainties, are also shown.

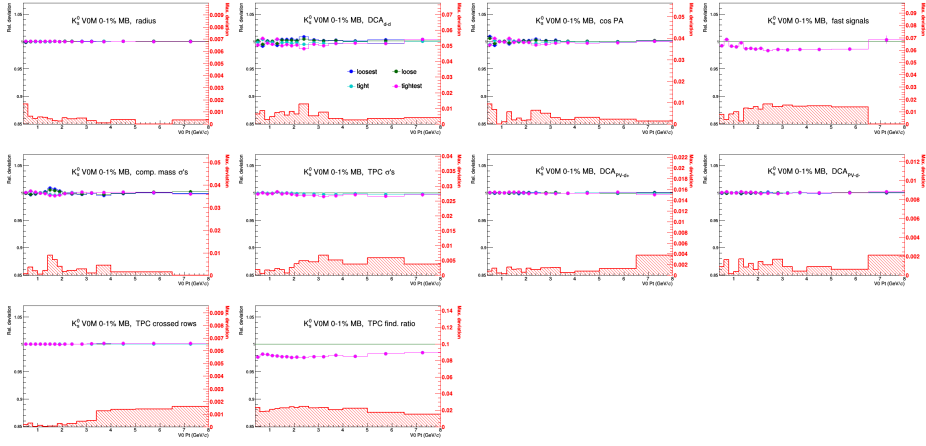


**Figure 7.9: NEEDS TO BE REDRAWN IN CONSISTENT STYLE WITH RT CHAPTER:** Deviations of the corrected spectra w.r.t. the different cut variations used for the  $K_S^0$ . The maximum deviation is added in quadrature to the total, if it's larger than  $\sigma_{RB}$  (depicted as errorbars) from unity.

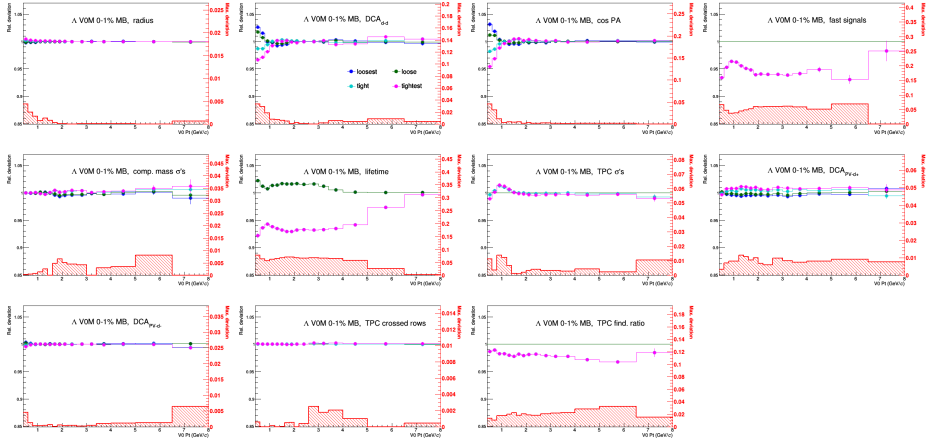


**Figure 7.10: NEEDS TO BE REDRAWN IN CONSISTENT STYLE WITH RT CHAPTER:** Deviations of the corrected spectra w.r.t. the different cut variations used for the  $K_S^0$ . The maximum deviation is added in quadrature to the total, if it's larger than  $\sigma_{RB}$  (depicted as errorbars) from unity.

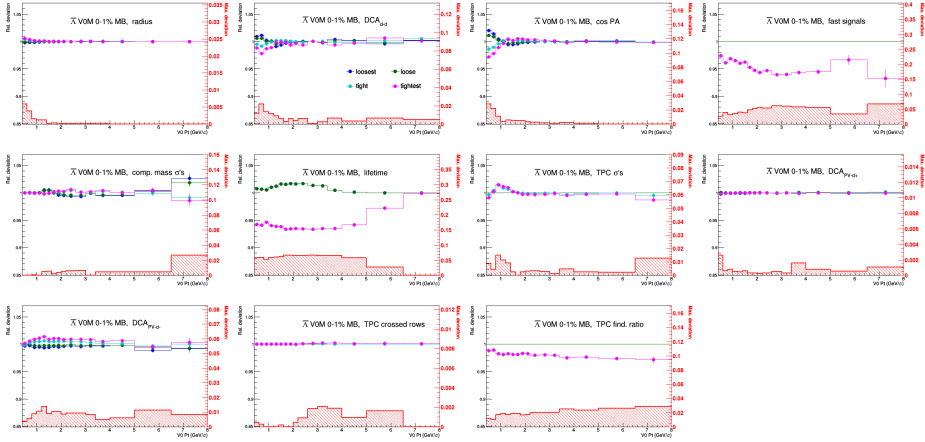


**Figure 7.11:** NEEDS TO BE REDRAWN IN CONSISTENT STYLE WITH RT CHAPTER: Deviations of the corrected spectra w.r.t. the different cut variations used for the  $K_S^0$ . The maximum deviation is added in quadrature to the total, if it's larger than  $\sigma_{RB}$  (depicted as errorbars) from unity.

## 7.2.2 Experimental bias

*TBA One paragraph about the experimental bias uncertainty*

## 7.2.3 Correlation of uncertainties with $S_O^{(p_T=1.0)}$

Correlations of several systematic uncertainties with respect to the  $S_O^{(p_T=1.0)}$  selection are expected. Since the ratios of jetty/isotropic results to  $S_O^{(p_T=1.0)}$ -unbiased ones provide important insights, it is necessary to study and account for these correlations.

*TBA One paragraph add formulae and add methodology.*

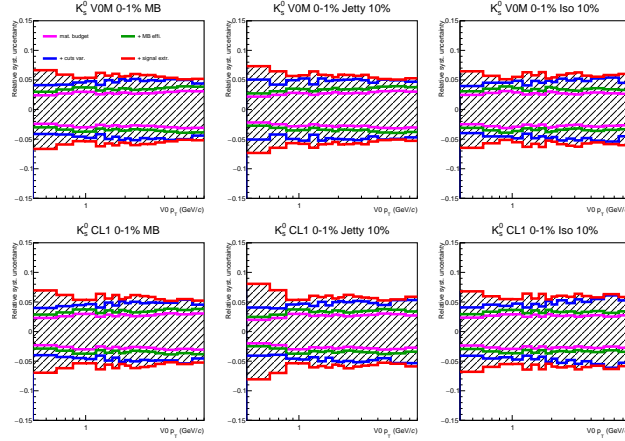
The systematic uncertainty associated with the material budget is fully correlated, while assuming the reconstruction efficiency is independent of multiplicity leads to an uncorrelated uncertainty. This assumption would lead to a factor of  $\sqrt{2}$  in the ratios of jetty/isotropic to  $S_O^{(p_T=1.0)}$ -unbiased for this uncertainty. However, in ALICE, this assumption is generally considered too conservative by ALICE, and thus this factor is dropped. The same approach is used for the uncertainty associated with the multiplicity independence of the feeddown matrix. Detailed results can be found in Appendix ??.

## 7.2.4 Summary

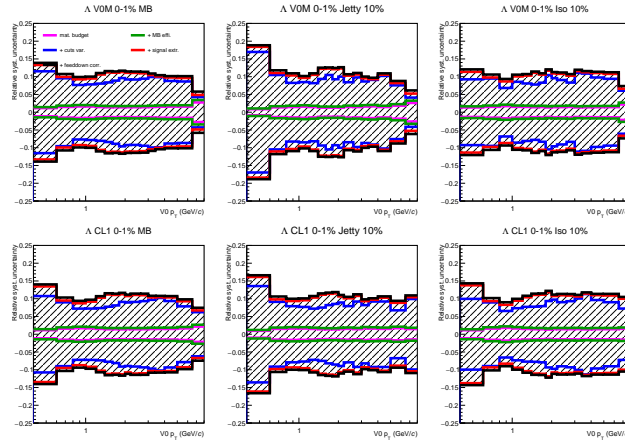
The total systematic uncertainties are reported in Tab. 7.3 and visualised in Fig. 7.12.  
*Add brief description of the biggest sources.*

**Table 7.3:** The most relevant systematic uncertainties for the long-lived particles  $K_S^0$  and  $\Lambda(\bar{\Lambda})$  as a function of  $S_O^{(p_T=1.0)}$ . “HM” in this table represents the  $S_O^{(p_T=1.0)}$ -unbiased spectra. Uncertainties are  $p_T$ -dependent, and the ranges listed represents the minimum-maximum values presented in the final spectra (see text for details).

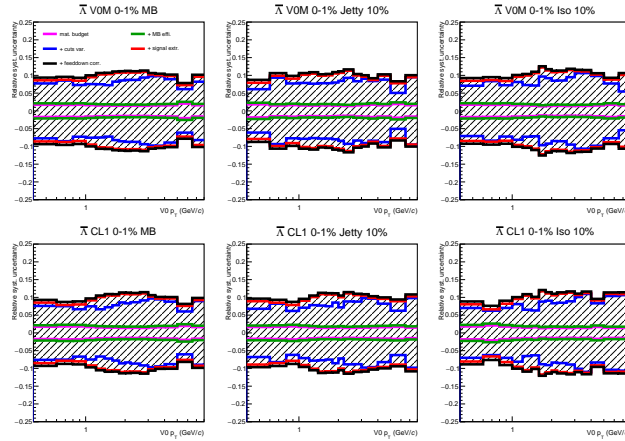
Topology:	Jetty	Iso	HM	Jetty/HM	Iso/HM
$K_S^0$					
Selection cuts	3%	3–4%	3–4%	Negl.	1%
Track pile-up	1%	1–3%	1%	0–2%	0–2%
Signal extraction	1–3%	1–3%	1–3%	Negl.	Negl.
Efficiency	2%	2%	2%	2%	2%
Material budget	4%	4%	4%	—	—
Experimental bias	4%	1%	—	4%	1%
Total uncertainty	7%	6–7%	5–6%	5%	2–3%
$\Lambda(\bar{\Lambda})$					
Selection cuts	1–5%	2–6%	4–5%	0–1%	0–3%
Track pile-up	4–5%	5%	3–5%	0–1.5%	0–1%
Signal extraction	2–6%	2–6%	2–6%	0–2%	0–1%
Feed-down correction	1.0–1.5%	1.0–1.5%	1.0–1.5%	Negl.	Negl.
Efficiency	2%	2%	2%	2%	2%
Material budget	4%	4%	4%	—	—
Experimental bias	4%	1%	—	4%	1%
Total uncertainty	8–10%	8–9%	7–9%	5%	3–4%



(a)



(b)



(c)

**Figure 7.12: NEEDS TO BE REDRAWN IN CONSISTENT STYLE WITH RT CHAPTER:** Total relative systematic uncertainty and individual contributions for the  $K_0^0$ ,  $\Delta$ , and  $\bar{\Delta}$ .

### 7.3 Transverse momentum spectra vs. $S_O^{(p_T=1.0)}$

The corrected spectra in V0M and  $N_{\text{SPD}_{\text{Trkls}}}$  high-multiplicity events and the dependence on spherocity for the  $K_S^0$  and  $\Lambda + \bar{\Lambda}$  can be seen in Fig. 7.13 and Fig. 7.14, respectively. The trends observed in the spectra are consistent between  $K_S^0$  and  $\Lambda$  and indicate a significant hardening (softening) in the low (high) spherocity selection, relative to the inclusive high-multiplicity event class. These trends are also well captured by all included model predictions, although the absolute values are not described well in XX by YY. TBA re-do plots with MC lines!

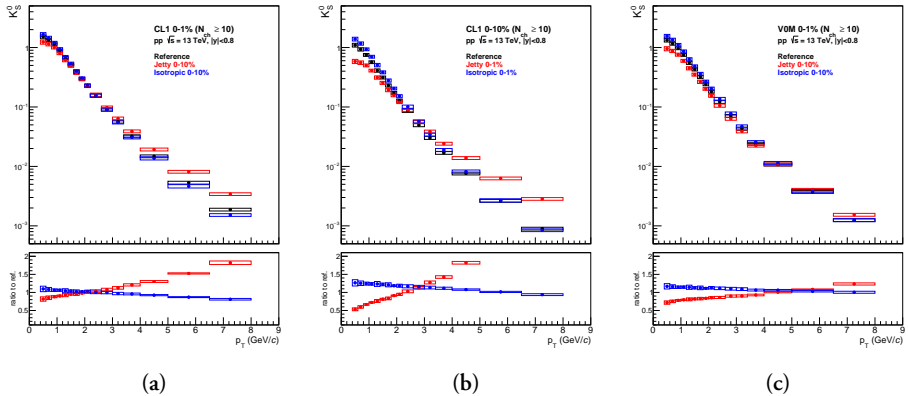


**Figure 7.13:** NEEDS edits: Corrected and normalised  $p_T$ -spectra of the  $K_S^0$  particle in high-multiplicity V0M 0-1% (top left, bottom left), CL1 0-1% (top middle, bottom right), and CL1 0-10% (top right) events, shown as black points. The bottom (jetty) and top (isotropic) 1% or 10% of spherocity events are also shown as red and blue points. The ratios of isotropic/jetty spectra to the high-multiplicity spectra are shown in the bottom panels.

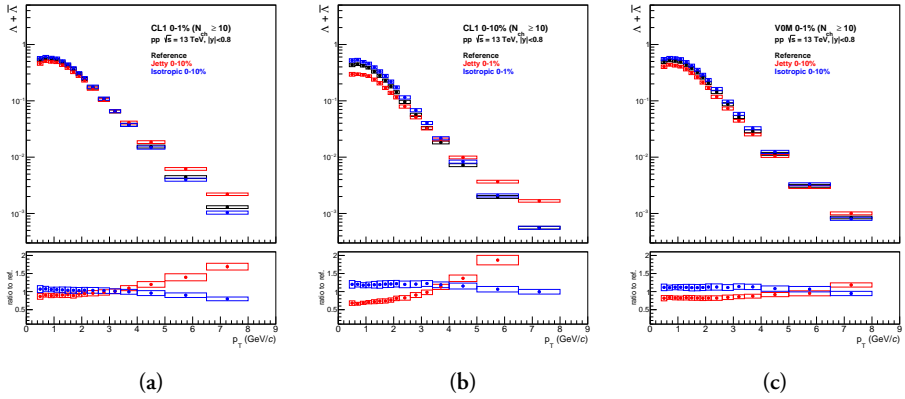


**Figure 7.14:** NEEDS edits: Corrected and normalised  $p_T$ -spectra of the  $\Lambda + \bar{\Lambda}$  particles in high-multiplicity V0M 0-1% (top left, bottom left), CL1 0-1% (top middle, bottom right), and CL1 0-10% (top right) events, shown as black points. The bottom (jetty) and top (isotropic) 1% or 10% of spherocity events are also shown as red and blue points. The ratios of isotropic/jetty spectra to the high-multiplicity spectra are shown in the bottom panels.

### 7.3.1 Ratios of neutral kaons to charged kaons

To verify the robustness of  $S_O^{(p_T=1.0)}$  as an event observable, the  $p_T$  spectra of neutral and charged kaons are compared in the  $N_{\text{SPD}_{\text{Trkts}}}$  I and V0M I classes. The ratios exhibit no dependence on  $S_O^{(p_T=1.0)}$  and are consistent with unity, according to expectations. The slight depletion of  $K_S^0$  in the  $N_{\text{SPD}_{\text{Trkts}}}$  I class is interpreted as the multiplicity selection bias due to requiring a large number of charged tracks at mid-rapidity, and is also reproducible by simulations. The ratios are shown in Fig. 7.15.

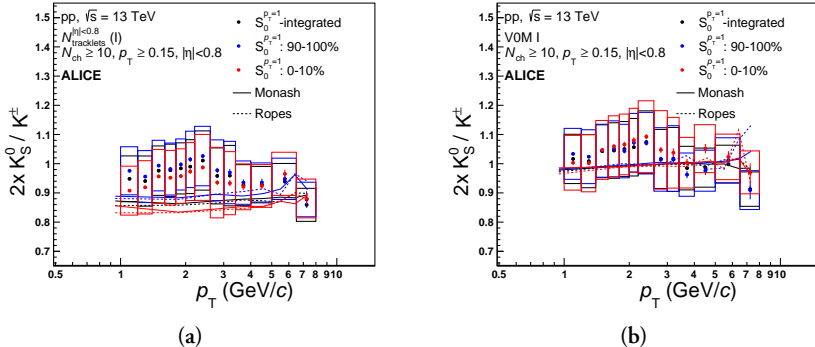


**Figure 7.15:** NEEDS edits: Ratios of neutral to charged kaons.

## 7.4 Mean transverse momenta and integrated yields

The  $\langle p_T \rangle$  and particle yields  $\langle dN_{\text{ch}}/dy \rangle$  in different  $S_O^{(p_T=1.0)}$  bins for the  $N_{\text{SPD}_{\text{Trkts}}} \geq 1$  class are reported in Fig. 7.16. The measured values of  $\langle p_T \rangle$  quantify the observations in the spectra: there is a significant  $p_T$ -hardening in jet-like events, consistently seen in both  $K_S^0$  and  $\Lambda$ . Furthermore, the  $\langle p_T \rangle$  of the inclusive high-multiplicity events is consistent with that of the isotropic subsample. This result suggests that the average high-multiplicity events and  $S_O^{(p_T=1.0)}$ -selected isotropic events are dominated by similar underlying physics processes.

Furthermore, the  $S_O^{(p_T=1.0)}$ -integrated event class is not simply the arithmetic average of the jetty and isotropic subsamples. This implies that jetty events are rare outliers of a much more homogeneous group of high-multiplicity events, which will be further focused on in the next sections.

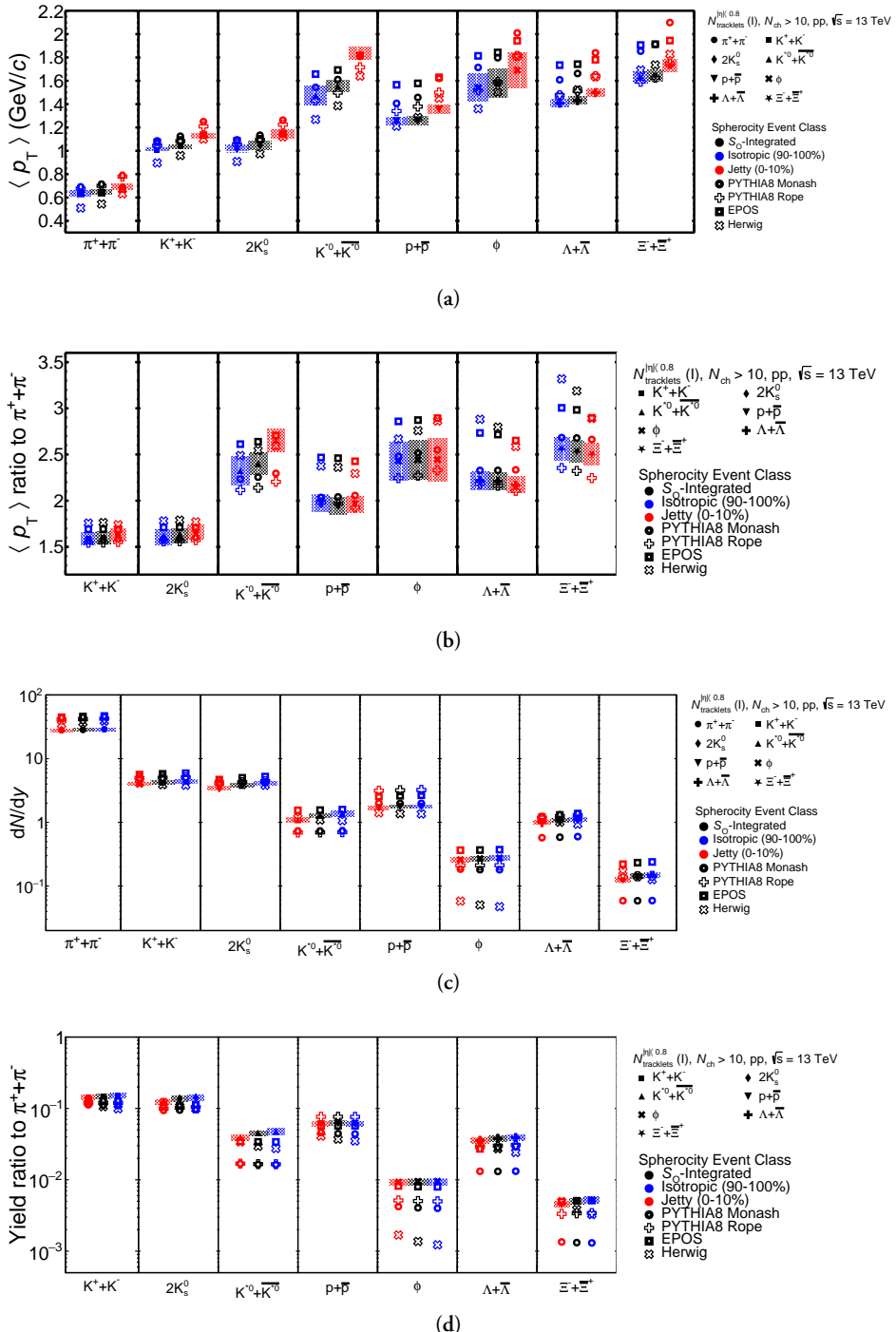


Figure 7.16: CROP TO SHOW ONLY  $\pi$ ,  $K_S^0$ ,  $\Lambda$ .

The results indicate that not only charged pions but also neutral  $K_S^0$  and  $\Lambda$  show little variation in multiplicity between the different  $S_O^{(p_T=1.0)}$  extremes in the  $N_{\text{SPD}_{\text{Trkts}}}$  I class, although more so for the latter two. This could be because of their smaller correlation with  $S_O^{(p_T=1.0)}$  as they are neutral, or it may suggest strangeness enhancement. The models generally provide good agreement with the measured  $\langle p_T \rangle$  of  $K_S^0$ , while the results for  $\Lambda$  are best described by the Pythia Ropes model. The yields for  $K_S^0$  are also largely consistent with the models presented, whereas the Pythia Monash model does not match the  $\Lambda$  yields.

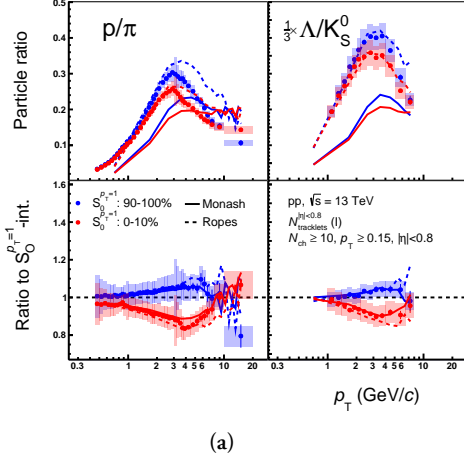
## 7.5 Ratios to pions

*Potentially leave out as the message there is redundant? Otherwise include in 2 paragraphs + definition and motivation.*

## 7.6 Baryon-to-meson ratio

The baryon-to-meson ratio  $(\Lambda^0 + \bar{\Lambda}^0)/(2K_S^0)$  was investigated in this study, as it is a common observable used to measure the effects of radial flow, as discussed in Section X. The results for the  $N_{\text{SPD}_{\text{Trkts}}}$  I class are shown in Fig. 7.17 and juxtaposed with the  $p/\pi$  ratios. The ratios reveal a significant increase when transitioning from jetty to isotropic events, indicating that the production of heavier  $\Lambda$  is systematically more suppressed in jetty events than  $K_S^0$ . Although the increase in the ratio is consistent with the typical signatures of radial flow, the results do not show the depletion at low  $p_T$  or the shift of the peak to higher  $p_T$ , which are also its characteristic features.

*Potentially also show the VOM results.*



(a)

**Figure 7.17:** Results on the baryon-to-meson ratios in the  $N_{\text{SPD}_{\text{Trkts}}} \text{ I class}$ . TBA

## 7.7 Ratio of integrated yields vs. $S_O^{(p_T=1.0)}$

The main contribution of this study is the investigation of strangeness production as a function of  $S_O^{(p_T=1.0)}$ . Yields of the  $\Lambda$  baryon were determined in  $N_{\text{SPD}_{\text{Trkts}}} \text{ I}$  and V0M I classes in the following intervals of  $S_O^{(p_T=1.0)}$ : 0 – 1%, 1 – 5%, 5 – 10%, 10 – 20%, 20 – 80%, 80 – 90%, 90 – 95%, 95 – 99%, and 99 – 100%. The integration was done in the measured  $p_T$  range rather than extrapolated. The  $S_O^{(p_T=1.0)}$ -dependent  $\Lambda$  yields are then divided by  $S_O^{(p_T=1.0)}$ -dependent pion yields as a reference. The effects of not extrapolating were studied and found to be unimportant, and while the extrapolation confirms the physics message of the default method, it also increases systematic uncertainties.

The results, together also with  $p(|S| = 0)$  and  $\Xi(|S| = 2)$  are reported in Fig. 7.18. For the  $N_{\text{SPD}_{\text{Trkts}}} \text{ I}$  events, there is a clear strangeness- and/or mass-dependent enhancement with increasing  $S_O^{(p_T=1.0)}$ . It is important to emphasize that in this event class, the  $N_{\text{ch}}$  multiplicity is basically fixed. Therefore, these effects are results of the different underlying dynamics of the collisions, specifically the varying hardness of involved scatterings, rather than merely an effect of increased  $N_{\text{ch}}$ .

Conversely, the V0M I events show no such dependence, and jetty and isotropic events appear to produce the same relative amount of strangeness. This goes against intuition that varying  $N_{\text{ch}}$  between jetty ( $N_{\text{ch}} \rightarrow 16$ ) and isotropic events ( $N_{\text{ch}} \rightarrow 3$ , according to Fig. 7.7) should introduce an effect, in accordance with traditional stud-

ies of strangeness enhancement in pp collisions as a function of  $N_{\text{ch}}$ . This observation is not fully understood, but it suggests that the decrease in strangeness in jetty events due to the decrease in  $N_{\text{ch}}$  and slight increase in  $\langle p_T \rangle$  is counterbalanced by some other factors of the collision.

Finally, the results were compared with MC predictions, and only Pythia Ropes accurately captures the observed trends and, to some extent, the magnitudes.

*Maybe also show the  $N_{\text{SPD}_{\text{Trkts}}}$  III result, although it is redundant.*

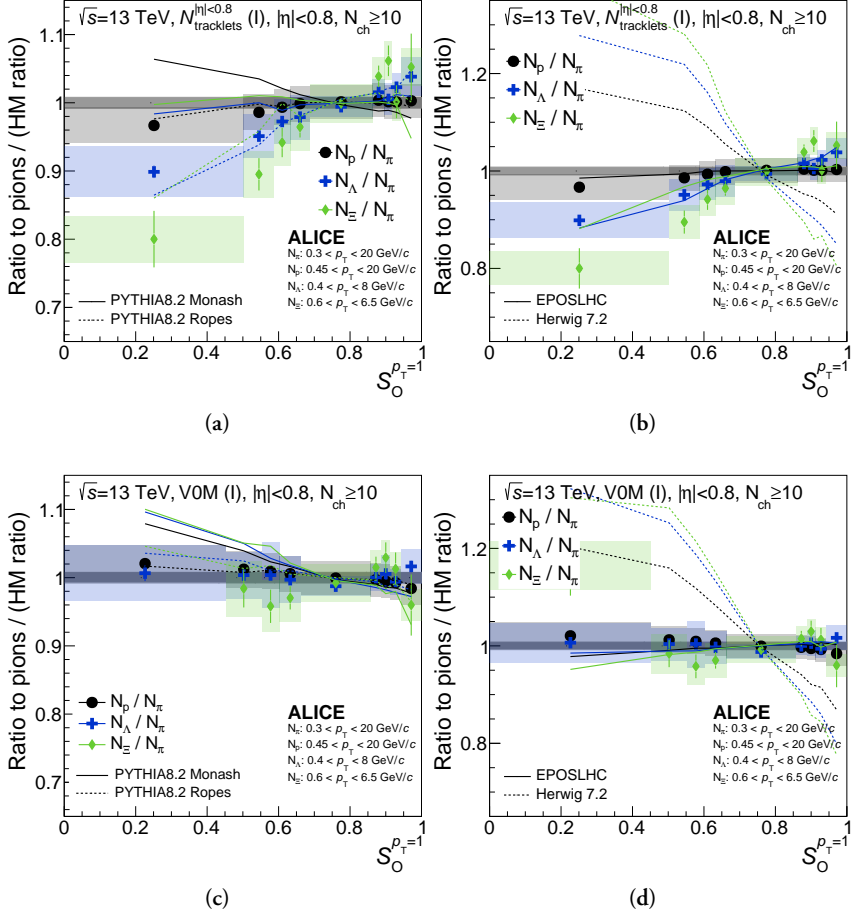


**Figure 7.18:** Double-ratios of integrated yields with respect to pions as a function of  $S_O^{(p_T=1.0)}$  in the  $N_{\text{SPD}_{\text{Trkts}}}$  I and V0M I events. Statistical and total systematic uncertainties are shown by bars and boxes, respectively. The curves represent different model predictions of the same measurement: (a),(c) Pythia Monash and Ropes, (b),(d) EPOS LHC and Herwig.



# Chapter 8

## Underlying Event Activity

In this chapter, measurements of  $K_S^0$ ,  $\Lambda$ , and  $\bar{\Lambda}$  are reported as a function of underlying event activity classifiers  $R_T$ ,  $R_{T,\min}$ , and  $R_{T,\max}$ . These observables quantify the magnitude of underlying event and are an experimental proxy of the  $n_{\text{MPI}}$ .

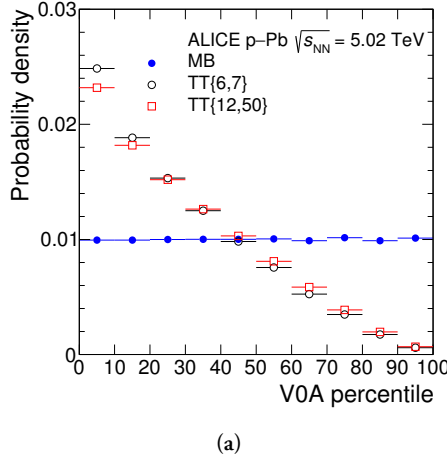
### 8.1 Motivation for studying event sub-structure

#### 8.1.1 Underlying event

As discussed in Chapter X, the underlying event, also interchanged with the concept of jet pedestal in some literature, is composed of particles that are not directly related to the primary hard scattering and its related fragmentation. It can be studied to extract accurate information about the hard scattering process by subtracting it in precision measurements of jet properties. Moreover, since it is a manifestation of the proton substructure and the parton interactions, it can give us insight into the parton dynamics in the nonperturbative QCD region.

#### 8.1.2 Hard process–multiplicity bias

Studying QGP phenomena in small systems as a function of event activity is challenging due to selection biases that arise when analyzing the data. It is known that selecting events with large momentum transfer leads to a bias towards higher multiplicities (and underlying event), and conversely, selecting events with higher multiplicities (and UE) enhances the hard processes. This bias can be understood in several



(a)

**Figure 8.1:** TBA

ways. Firstly, a hard process tends to occur with lower impact parameters, which in turn leads to higher particle multiplicities. Secondly, an event with  $n$  partonic interactions has  $n$  chances of containing a hard process. Lastly, harder processes fragment into more particles, further contributing in higher event activity. As an example, Figure 8.1 shows how the requirement of a high  $p_T$  track can skew the forward-rapidity centrality distribution to lower values (higher event activity), as observed in a result from ALICE.

### 8.1.3 Azimuthal regions and transverse activity

The selection bias of hard processes on UE becomes saturated at high  $p_T$ , where the impact parameter bias is fixed and stochastic effects become comparable. This saturation effect can be observed when studying particle production in three topological regions defined with respect to the highest momentum track, which serves as a proxy for the axis of the primary scattering process. The three regions are defined as follows:

1. Towards (also known as "Near"), where  $|\phi - \phi^{\text{leading}}| < \frac{\pi}{3}$ ,
2. Away, where  $|\phi - \phi^{\text{leading}}| > \frac{2\pi}{3}$ , and
3. Transverse, where  $\frac{\pi}{3} < |\phi - \phi^{\text{leading}}| < \frac{2\pi}{3}$ .

Here,  $\phi^{\text{leading}}$  is the azimuthal angle of the leading track. This definition is illustrated in Figure 8.2.

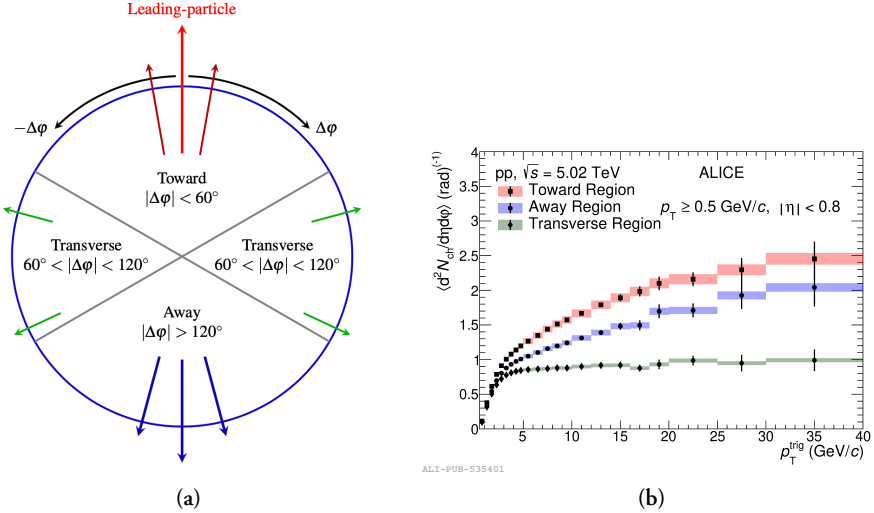


**Figure 8.2:** TBA

Studying particle multiplicity (or sum of their  $p_T$ ) in these regions as a function of the transverse momentum of the leading track  $p_T^{\text{leading}}$  reveals that in the regions Towards and Away, the multiplicity continues to increase with the hardness of the primary process. These regions contain the leading and the recoil jet, respectively. In contrast, in the Transverse region, the multiplicity (further denoted as  $N_T$  in this thesis but  $N_{\text{ch}}^{\text{trans}}$  is also used in cited literature) reaches a plateau at around  $5 \text{ GeV}/c$ . In this region, the underlying event becomes independent of the strength of the primary process, and the selection bias is minimized. Notably, this phenomenon is universal regardless of the system size or collision energy. As an example, measurements from ALICE are shown in Fig. 8.2.

## 8.2 $R_T$ as an experimental observable

The magnitude of the underlying event can be measured using the self-normalized ratio:

$$R_T = \frac{N_T}{\langle N_T \rangle}, \quad (8.1)$$

which is often referred to as the underlying event activity, transverse activity, or relative transverse activity in various literature, and also in this thesis. This observable and its uses were suggested in Ref.?

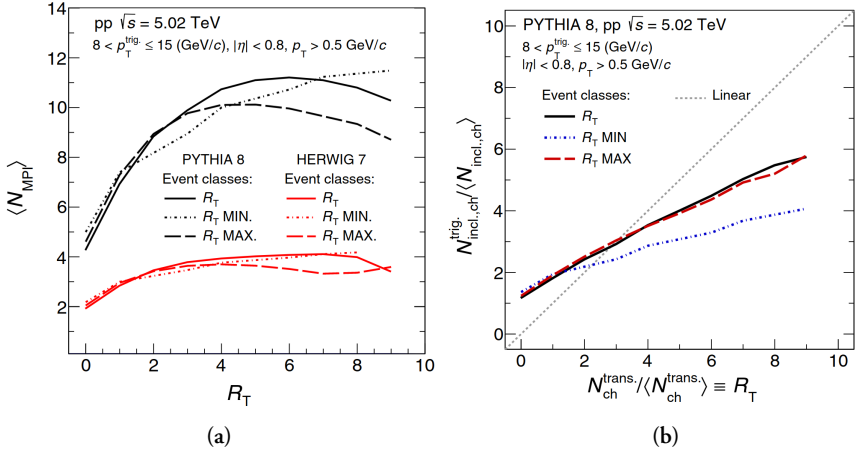


**Figure 8.3:** TBA

By applying  $R_T$ , two limits of events can be studied:

- $R_T \rightarrow 0$ : the “ee” limit, where events with minimal UE are selected. These events are dominated by a single hard scattering and can be compared to LEP fragmentation models.
- $R_T \rightarrow \infty$ : the “AA” limit, where events with very high transverse activity are selected, which can come from many MPIs and/or from transverse jets. These events may exhibit collective features similar to AA collisions.

### 8.2.1 Proxy to $n_{\text{MPI}}$

As could be intuitively expected,  $R_T$  serves as an experimental proxy for  $\langle n_{\text{MPI}} \rangle$ . Phenomenological models that incorporate MPIs provide an illustration of this relationship. As shown in Fig. 8.3, Pythia 8 predicts a strong dependence of  $\langle n_{\text{MPI}} \rangle$  on  $R_T$  until  $R_T \lesssim 5$ . Similarly, Herwig 7 predicts a dependence until  $R_T \lesssim 3$ , albeit weaker. Pythia’s prediction for the relationship between  $R_T$  and the event multiplicity, which is affine, is also shown in the figure.

### 8.2.2 Extension to $R_{T,\text{min}}, R_{T,\text{max}}$

To separate the soft and hard components of the underlying event – namely, the MPIs from wide-angle ISR/FSR – the definition of  $R_T$  can be extended. The two transverse

sub-regions can be further classified as Transverse-min or Transverse-max, based on which sub-region has fewer or more particles. Softer contributions from MPIs will enter both sub-regions, whereas the effects of harder radiation should be captured in the Transverse-max sub-region. This makes Transverse-min more sensitive to particle production from MPIs.

Analogously, the following underlying event activity classifiers can be defined:

$$R_{T,\min} = \frac{N_{T,\min}}{\langle N_{T,\min} \rangle} , \quad (8.2)$$

$$R_{T,\max} = \frac{N_{T,\max}}{\langle N_{T,\max} \rangle} , \quad (8.3)$$

where  $N_{T,\min}$  and  $N_{T,\max}$  are the particle multiplicities in the Transverse-min and Transverse-max sub-regions, respectively. This approach follows measurements developed at UE studies at Tevatron<sup>?</sup> and have been suggested to use in searches for QGP phenomena in small systems based on investigations in phenomenological models<sup>?</sup>.

According to Pythia 8, as shown in Fig. 8.3,  $R_{T,\min}$  and  $R_{T,\max}$  follow different relationships with  $\langle n_{\text{MPI}} \rangle$ . Whereas  $\langle n_{\text{MPI}} \rangle$  starts falling as a function of  $R_{T,\max}$  (due to the inclusion of mini-jets) at  $R_{T,\max} \approx 5$ , it continues rising as a function of  $R_{T,\min}$  across the entire range. Furthermore, compared to  $R_T$ ,  $R_{T,\min}$  also shows some degree of decorrelation with event multiplicity.

### Charged particle $p_T$ spectra

Phenomenological models also reveal a significantly different evolution of transverse momentum spectra of inclusive charged particles based on  $R_{T,\min}$  and  $R_{T,\max}$ , as shown in Fig. 8.4. For the highest reported ranges of  $R_{T,\max}$  and  $R_T$ , a significant hardening of the spectrum is observed in both Pythia 8 and Herwig 7, similarly to multiplicity studies<sup>?</sup>, indicating a strong auto-correlation. In contrast,  $R_{T,\min}$  exhibits a Cronin-like enhancement at intermediate  $p_T$  and a plateau at  $p_T \gtrsim 6 \text{ GeV}/c$ , even in the highest  $R_{T,\min}$  bin.

#### 8.2.3 Track and event selection

The event selection follows the same criteria as the  $S_O^{(p_T=1.0)}$  measurement discussed in Section 7.1.4, which conform to the standard analysis of light flavour hadrons versus multiplicity in pp collisions conducted in ALICE. The INEL  $> 0$  events, which require at least one hit in either V0A or V0C scintillators and a track reconstructed within  $|\eta| < 1$ , are used. The SPD is used for the reconstruction of primary vertex,

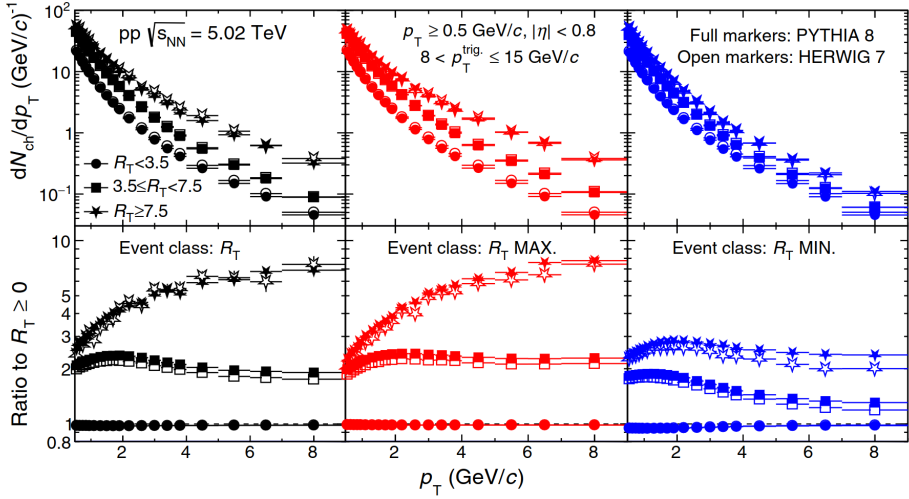


**Figure 8.4:** TBA

which is further required to have  $|\Delta z| < 10$  cm to reject out-of-bunch pile-up. To remove in-bunch pile-up, events with multiple reconstructed vertices are excluded.

Events are required to have a leading track with reconstructed momentum  $5 < p_T^{\text{leading}} < 40 \text{ GeV}/c$ <sup>1</sup>. These values were chosen to access the plateau in transverse activity and isolate the UE while retaining a large data sample. Maintaining a high momentum and spatial resolution of the leading track is crucial in this measurement. However, this can be compromised at high  $p_T$  when a significant portion of the track curvature can fall between two sectors of the TPC. To address this issue, geometrical cuts are used, as discussed in Section ??.

For both the leading particle as well as the particles entering  $N_T$  and  $R_T$  calculations, tracks are required to be within  $|\eta| < 0.8$  and have  $p_T > 0.15 \text{ GeV}/c$ , and must satisfy the following:

1. “Hybrid tracks”, described in more detail in Section ??, are used for both leading and  $N_T$  tracks to ensure a high level of azimuthal acceptance uniformity. These tracks consist of high-quality “global track” requirements, including the SPD information, which leads to azimuthal non-uniformity, and “complementary track” cuts, a looser set requiring only ITS and TPC in cases where the first are not satisfied.
2. For the leading track, strict  $p_T$ -dependent DCA cuts are applied in the trans-

---

<sup>1</sup>Note that  $p_T$  spectrum is falling very steeply, at an approximately exponential rate, making the upper bound negligibly restrictive compared to the lower bound.

verse direction ( $|DCA_{xy}| < 0.0182 + \frac{0.0350}{p_T^{1.01}}$  cm,  $p_T \in [\text{GeV}/c]$ ), to ensure good momentum resolution and that the track is a primary one.

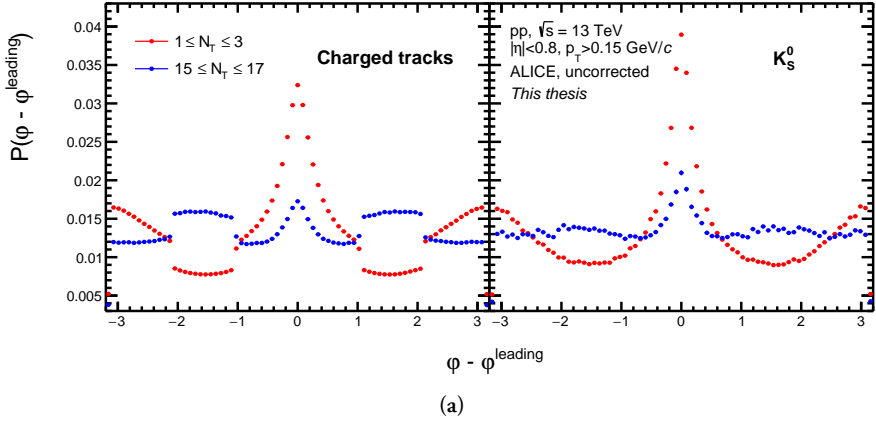
3. For the  $N_T$  tracks, a DCA cut ( $|DCA_{xy}| < 0.06$  cm) is required to avoid biases in  $V^0$  measurements, as explained in the text below.

### 8.2.4 $R_T$ measurements of neutral particles vs. charged particles

The  $V^0$ s are neutral particles and thus, they cannot be leading tracks nor enter  $N_T$  ( $N_{T,\min}$ ,  $N_{T,\max}$ ) and  $R_T$  ( $R_{T,\min}$ ,  $R_{T,\max}$ ) calculations. This has several implications:

1.  $V^0$ s suffer much less from auto-correlation biases than  $\pi/K/p$ , which can be seen in azimuthal distributions and in  $K_S^0/K^\pm$  ratios. Requiring high/low  $N_T/R_T$  can lead to an increase/decrease of charged particles in the Transverse region due to selecting fluctuations in addition to the UE scaling. However, this effect is significantly smaller for neutral  $V^0$ s. This behaviour is shown in Fig. 8.5. It is important to bear this caveat in mind when comparing  $p_T$  spectra and yields of  $\pi/K/p$  and  $V^0$ s.
2. While  $N_T$  is always at least 1 for  $\pi/K/p$  in the Transverse region, for  $V^0$ s it can be equal to 0. Similar logic applies to the Transverse-min/max sub-regions and  $N_{T,\min}/N_{T,\max}$ .
3. The maximum  $p_T$  measurable for  $\pi/K/p$  in the Toward region is limited to  $p_T < 5 \text{ GeV}/c$ , at which point the trigger requirement would lead to a trivial increase. For  $V^0$ s, however, this limitation does not apply and their measured  $p_T$  range does not need to be restricted.
4. The charged daughters of  $V^0$ s could sometimes enter  $N_T$ , leading to significant biases at low  $p_T$  in the Toward and Away regions of  $K_S^0/K^\pm$  ratios.

In this thesis, the behaviour described in the last point was rectified by making  $N_T$  track candidates and  $V^0$  daughter tracks two disjunct sets. This was achieved by applying the  $|DCA_{xy}| > 0.06$  cm cut, used in the  $V^0$  reconstruction as discussed in Section ??, in opposite ways. This reduces the  $N_T$  track candidates by less than 5%. The effect of this solution can be seen in Fig. 8.6.



(a)

Figure 8.5: TBA, maybe move to chapter about tracks.

### 8.3 Bayesian unfolding procedure

The  $V^0$ s measurements are conducted as a function of the number of measured tracks  $N_T^m$  within the detector acceptance. The measured multiplicity  $N_T^m$  includes a fraction of the true primary charged-particle multiplicity  $N_T^t$  not lost due to acceptance, efficiency, or track selection, as well as contributions from secondary particles or particles smeared into the measurement's kinematic acceptance due to detector resolution (i.e., from  $p_T < 0.15 \text{ GeV}/c$ ). These effects fluctuate on an event-by-event basis and thus there is no unique correlation between  $N_T^m$  and  $N_T^t$ . This means that events with true multiplicity  $N_T^t$  can be measured with different  $N_T^m$ , contributing to  $V^0$  measurements in multiple  $N_T^m$  bins. Therefore, each spectrum contains particles from events with many true multiplicities  $N_T^t$ .

This thesis uses a Bayesian unfolding procedure, as discussed in Ref.?, to convert  $V^0$ s measurements as a function of  $N_T^m$  into measurements as a function of  $N_T^t$  and thus correct for the mentioned effects.

#### 8.3.1 One-dimensional unfolding

The measured multiplicity distribution  $n_{\text{ev}}(N_T^m)$  can be mathematically represented as the result of convolving (or “folding”) the true multiplicity distribution produced by the collisions,  $n_{\text{ev}}(N_T^t)$ , with the detector’s response function. The response matrix  $S_{mt}$ , which represents the conditional probability  $P(N_T^m|N_T^t)$  of an event with multiplicity  $N_T^t$  being measured with multiplicity  $N_T^m$ , can be obtained from MC simulations of the apparatus. Using this matrix, also shown in Fig. 8.9,  $n_{\text{ev}}(N_T^m)$  can

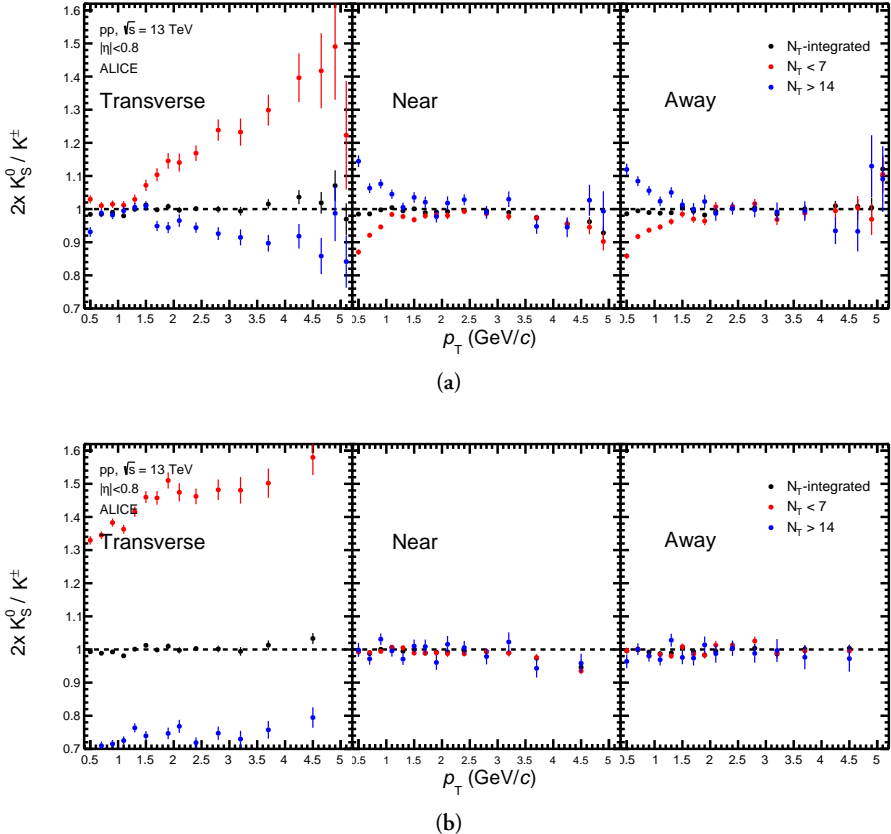


**Figure 8.6:** TBA

be expressed in terms of  $n_{\text{ev}}(N_T^t)$  as follows:

$$n_{\text{ev}}(N_T^m) = \sum_t S_{mt} \cdot n_{\text{ev}}(N_T^t) \quad , \quad (8.4)$$

To obtain the true multiplicity distribution from the measured distribution, the inverse of  $S_{mt}$  could be used, hypothetically, as shown below:

$$n_{\text{ev}}(N_T^t) = \sum_m S_{mt}^{-1} \cdot n_{\text{ev}}(N_T^m) \quad . \quad (8.5)$$

However, the inverse  $S_{mt}^{-1}$  may have multiple or zero solutions, making this approach unfeasible. Alternatively,  $S_{mt}^{-1}$  could be obtained directly from MC simulations, just like the detector response. However, this matrix would then strongly depend on the generated  $N_T^t$  distribution and be significantly model-dependent, as physics generators vary in their  $N_T^t$  predictions. In contrast, the detector response is mostly affected

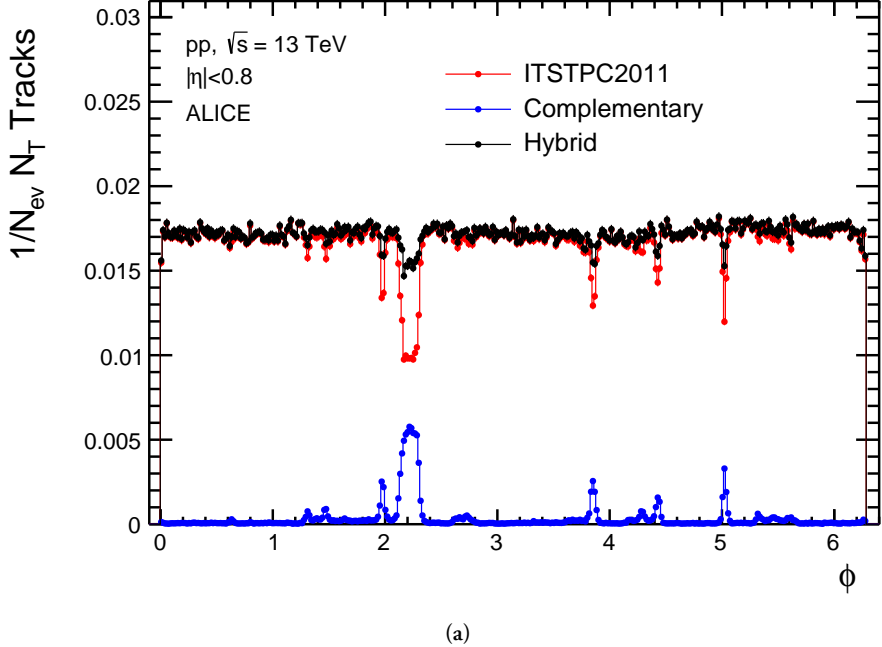


**Figure 8.7:** TBA, maybe move to chapter about tracks.

by the accuracy of the particle propagation simulations, which is a lot more understood. Therefore, an iterative numerical procedure based on Bayes' theorem is used to obtain the unfolding matrix  $M_{mt}$ , which represents the conditional probabilities  $P(N_T^t | N_T^m)$ .

In this application, Bayes' theorem can be expressed in terms of  $N_T^m$  and  $N_T^t$  as follows,

$$P(N_T^t | N_T^m) = \frac{P(N_T^m | N_T^t) P(N_T^t)}{P(N_T^m)} , \quad (8.6)$$

where  $P(N_T^t)$  and  $P(N_T^m)$  are probability distributions for an event occurrence with  $N_T^t$  and  $N_T^m$ , respectively. Assuming that  $P(N_T^t)$  is known,  $P(N_T^m)$  can be calculated as follows:

$$P(N_T^m) = \sum_t P(N_T^m | N_T^t) P(N_T^t) . \quad (8.7)$$

Therefore, using Eq. 8.6, the conditional probability in the unfolding matrix can be written as follows:

$$P(N_T^t | N_T^m) = \frac{P(N_T^m | N_T^t) P(N_T^t)}{\sum_{t'} P(N_T^m | N_T^{t'}) P(N_T^{t'})} . \quad (8.8)$$

However,  $P(N_T^t)$  (the “prior”) is initially unknown and must be arbitrarily chosen. The unfolding matrix can be calculated using this prior, and the unfolded distribution can be obtained as follows:

$$\hat{n}_{\text{ev}}(N_T^t) = \sum_m P(N_T^t | N_T^m) n_{\text{ev}}(N_T^m) . \quad (8.9)$$

This unfolded multiplicity can subsequently be used to update the prior as follows:

$$\hat{P}(N_T^t) = \frac{\hat{n}_{\text{ev}}(N_T^t)}{\sum_{t'} \hat{n}_{\text{ev}}(N_T^{t'})} , \quad (8.10)$$

starting a new iteration. The updated  $\hat{P}(N_T^t)$  is closer to the true  $P(N_T^t)$  than the initial guess because the arbitrarily chosen prior is constrained by the  $n_{\text{ev}}(N_T^m)$  observable, which contains information about  $P(N_T^t)$ .

Multiple approaches can be taken to choose the prior: a uniform distribution, the  $N_T^t$  distribution generated by a model, or the  $N_T^m$  distribution acquired from data. In this thesis, the prior choice was found to not play a role.

#### TBA: Normalisation

The  $\chi^2/\text{ndf}$  is calculated to determine the validity of the correction and the stopping point for the iterative process. It is calculated by comparing the  $N_T^t$  distribution – known a priori in the simulations – and the unfolded  $\hat{n}_{\text{ev}}(N_T^t)$  distribution, where ndf refers to the number of data points in the distribution. The process is stopped when  $\chi^2/\text{ndf}$  reaches a minimum value or the iterations take a maximum number of steps  $n_{\text{iter}}$ . This is imposed to avoid overfitting and overestimation of statistical uncertainties. The  $n_{\text{iter}}$  values are reported in Tab. 8.1. The entire iterative process is summarised in a diagram shown in Fig. 8.8.

The used response matrix, as well as the resulting unfolding matrix, can be seen in Fig. 8.9. The method still exhibits some degree of model dependence due to the generation of the response matrix. Previous studies in ALICE have compared the response matrix for  $N_T$  acquired from Pythia 8 and from EPOS LHC MC simulations, which revealed that the effect is less than 1%. This effect is taken into consideration as a source of systematic uncertainty.

**Table 8.1:** TBA.

Unfolding observable	$N_T$	$N_{T,\text{min}}$	$N_{T,\text{max}}$
$n_{\text{iter}}$	20 (max.)	10	18

Bayes' Theorem

$$P(N_T^t | N_T^m) = \frac{P(N_T^m | N_T^t) P(N_T^t)}{P(N_T^m)}$$

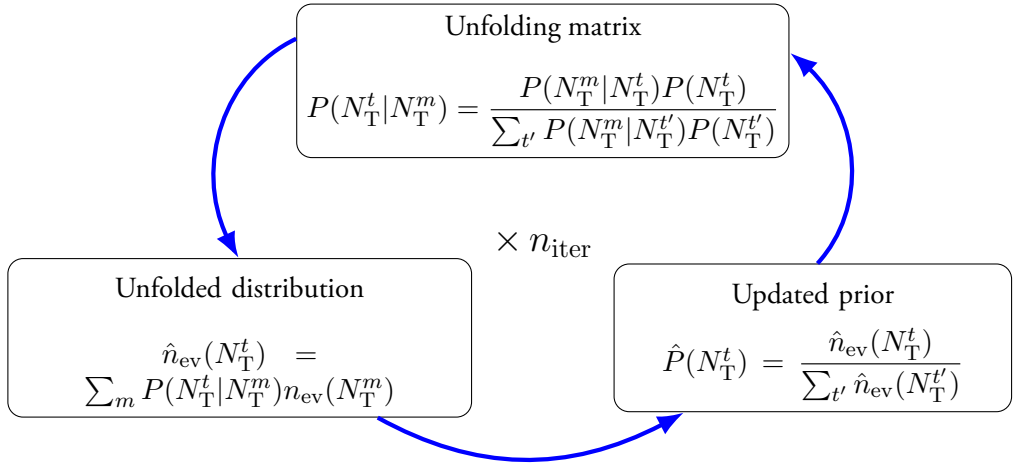


Figure 8.8: Diagram showing the Bayesian unfolding

### 8.3.2 Propagation of statistical uncertainties

TBA, One paragraph and then refer to literature

### 8.3.3 Unfolding of $K_S^0$ , $\Lambda$ , and $\bar{\Lambda}$ $p_T$ spectra

In the unfolding treatment of the  $\Lambda$  and  $\bar{\Lambda}$ , the particle and the anti-particle  $p_T$  spectra were combined to reduce statistical uncertainties and increase the method's robustness. For the Toward and Away regions, the spectra can be unfolded in a similar fashion to the  $N_T$  activity, assuming that they are completely decoupled from the production in the Transverse region. This implies mere reshuffling of  $V^0$ 's in individual  $p_T$  bins between different events, based on the unfolding recipe established above. Closure tests using MC simulations were conducted to compare the unfolded  $p_T$  spectra as a function of unfolded-reconstructed  $N_T$  to the generated  $p_T$  spectra as a function of generated  $N_T$ — and showed the plausibility of this approach. The closure tests are presented in Fig. 8.10, indicating mostly consistent results within 5%, with the deviations observed more in the  $R_T$  extremes.

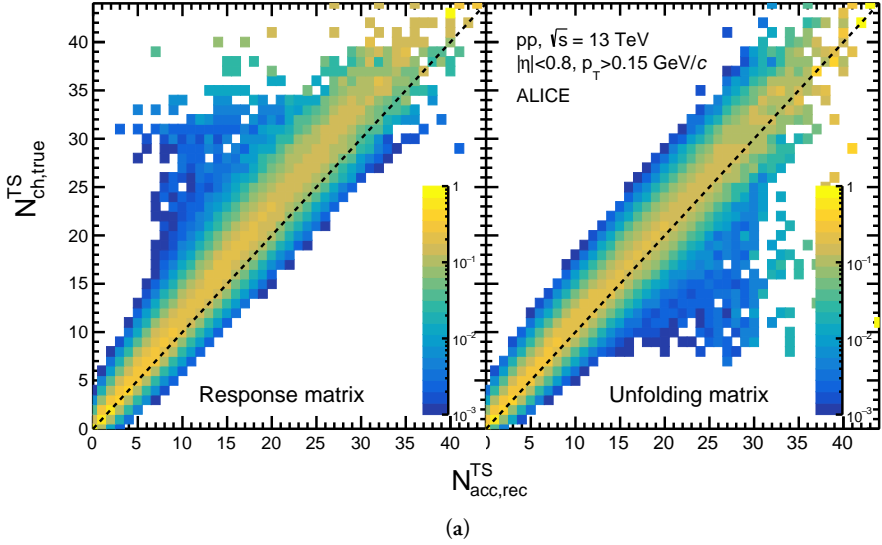


**Figure 8.9:** TBA

For the treatment of the Transverse regions, two approaches were considered:

1. Similarly to how this unfolding method was applied in other multiplicity and  $N_T$  measurements in ALICE for charged tracks, one assumes correlations between the  $p_T$  spectra and the event activity. This approach requires multiplying the response matrix with number of tracks in each column, modifying the unfolding matrix to make it  $p_T$ -dependent, and applying different unfolding recipes to  $V^0$ 's based on their  $p_T$ , which approximates reshuffling on a particle-by-particle basis.
2. Given the fact that the  $N_T$  tracks and the  $V^0$  daughters were made two disjunct sets in this measurement by separating them with a  $|DCA_{xy}|$  boundary, one may assume complete de-correlation between the  $V^0$   $p_T$  spectra and the measured  $N_T$ . Subsequently, the Transverse region would be treated like the Toward and Away.

In this study, both approaches were tested and the second method was chosen for the measurement. Although the first method generally produced somewhat better non-closure discrepancies, the second method is more logically sound. Additionally, modifying the response matrix in the first method resulted in an empty zeroth bin by construction. As a consequence, events with  $N_T = 0$  but  $N_{K_S^0, \Lambda} > 0$  could not be treated since the unfolding matrix cannot recover this scenario. While this is

not a limitation in charged particle analyses since such cases cannot occur, it posed a problem here.

The closure tests for the Transverse region are shown in Fig. 8.10, but it should be noted that they exhibit somewhat larger deviations (up to 10%) in the most extreme bins of  $R_T$  compared to the Toward/Away regions. One possible explanation for this is the simplicity of the unfolding method used here, as well as the fact that the closure tests were conducted on Pythia simulations, which can exhibit correlated particle production in phase space, leading to somewhat of a coupling between  $N_T$  and  $V^0$ s.

Unfolding of the  $V^0$ s spectra in the Transverse-min and Transverse-max regions as a function of  $N_{T,\min}$  and  $N_{T,\max}$ , respectively, was performed in an identical manner. Although the results close well in MC tests in the central  $R_{T,\min}/R_{T,\max}$  intervals, deviations of up to around 20% are observed in the most extreme bins, as depicted in Fig. 8.10. This is likely due to low statistics samples, the simplicity of the method, and the fact that the individual  $R_{T,\min}/R_{T,\max}$  intervals cover even smaller ranges of  $N_{T,\min}/N_{T,\max}$ , making the process highly sensitive to fluctuations.

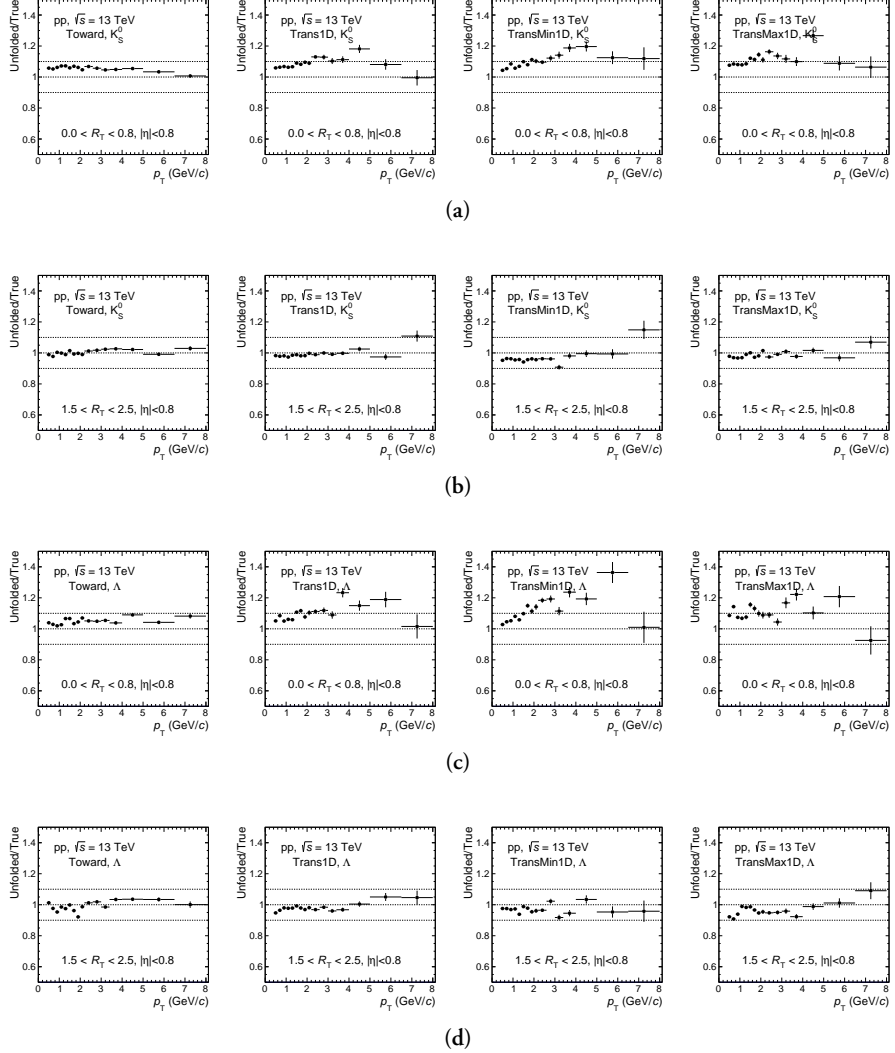


**Figure 8.10:** NEEDS EDIT: Closure tests for the Toward, Transverse, Transverse-min, and Transverse-max regions in selected  $R_T$  intervals for  $K_S^0$  and  $\Lambda$ .

## 8.4 $R_T$ , $R_{T,\min}$ , $R_{T,\max}$ distributions

The unfolded  $N_T$ ,  $N_{T,\min}$ , and  $N_{T,\max}$  distributions were self-normalised to obtain the  $R_T$ ,  $R_{T,\min}$ , and  $R_{T,\max}$  distributions, respectively. They are shown in Fig. 8.11 and compared with predictions from Pythia 8 (Monash tune and Ropes tune) as well as EPOS LHC. The different quantiles corresponding to the  $R_T/R_{T,\min}/R_{T,\max}$  ranges used in this measurement are also highlighted. It should be noted that since

$N_T, N_{T,\min}, N_{T,\max} \in \mathbb{N}_0$ , the  $R_T/R_{T,\min}/R_{T,\max}$  distributions are not continuous observables.

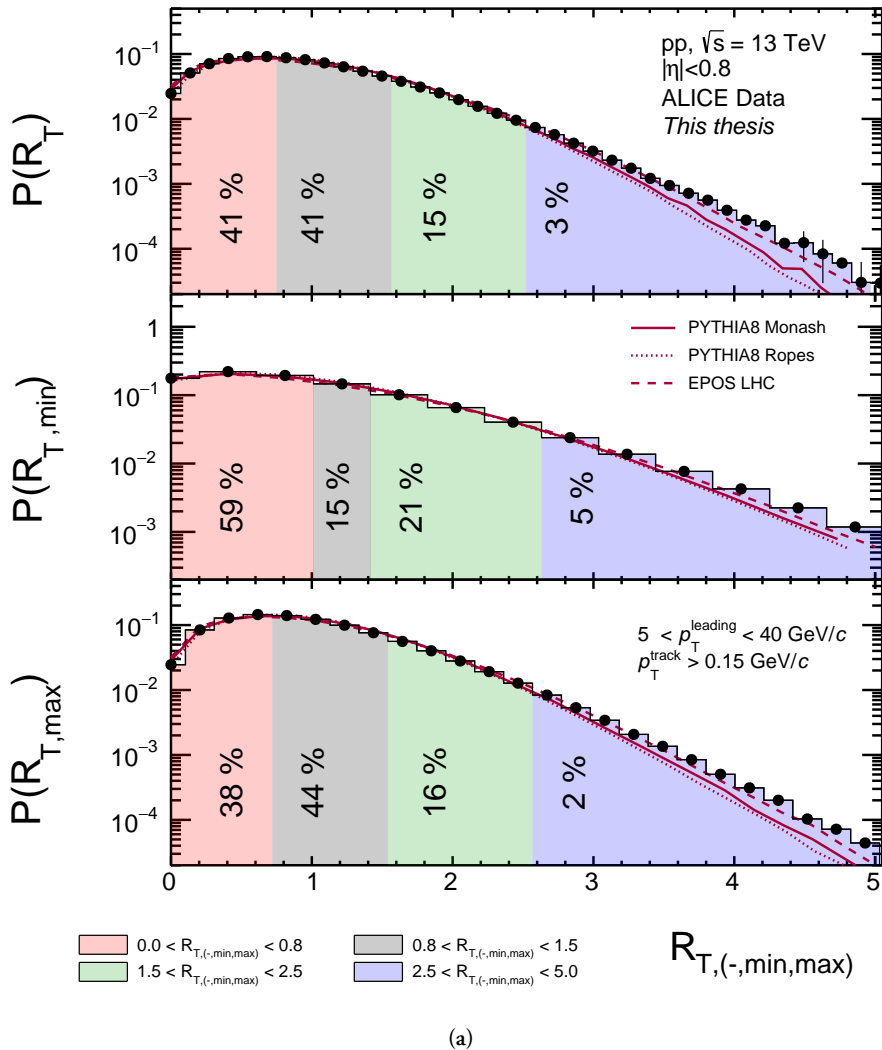


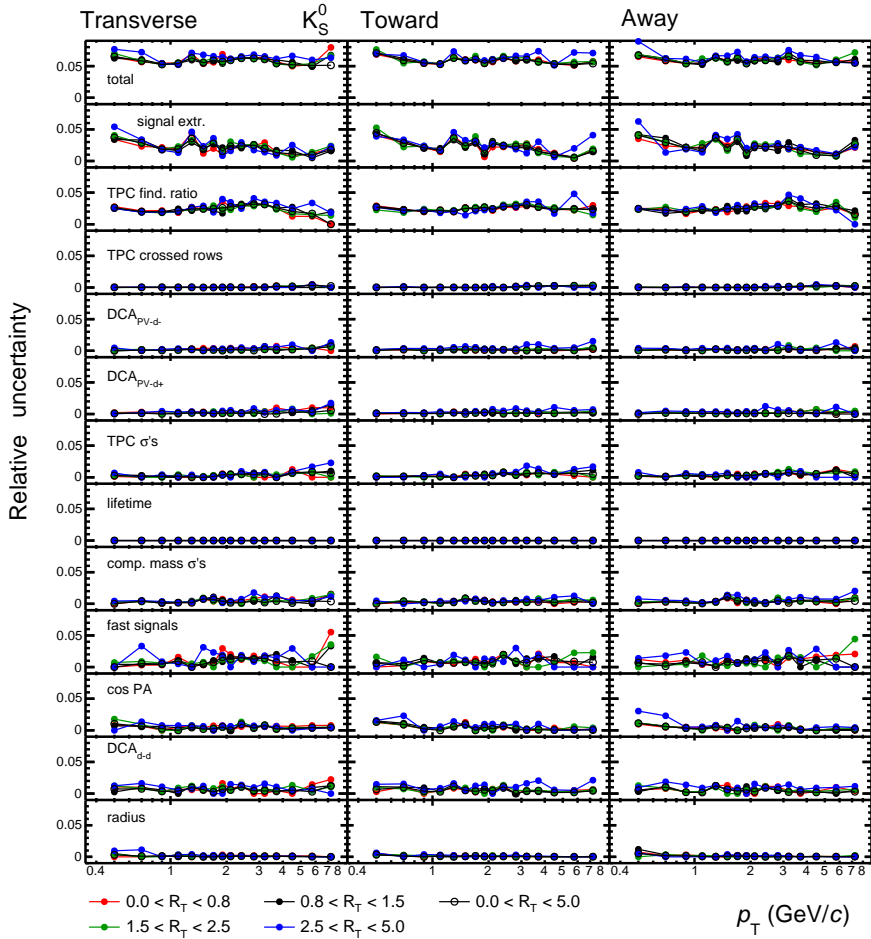
Figure 8.11: TBA

## 8.5 Systematic uncertainties

The systematic uncertainties on the  $p_T$  spectra were determined individually for each  $R_T$  interval and azimuthal region, following the procedures described in Section ??.

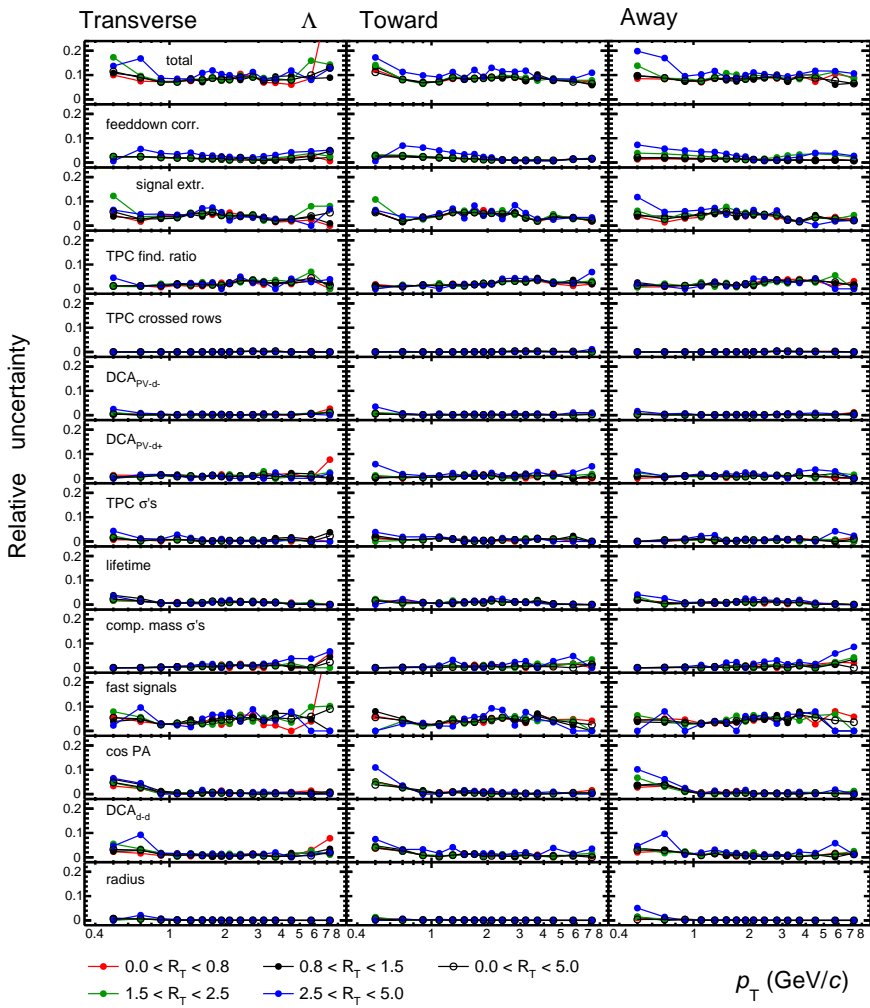
They are reported in Fig. 8.12, Fig. 8.13, and Fig. 8.14 for the  $K_S^0$ ,  $\Lambda$ , and  $\bar{\Lambda}$ , respectively. As there are no reasons to believe they should differ, they are then also applied in the  $R_{T,\min}$  and  $R_{T,\max}$  measurements.

*TBA One paragraph comment on the largest ones and make the style consistent with the spherocity chapter.*



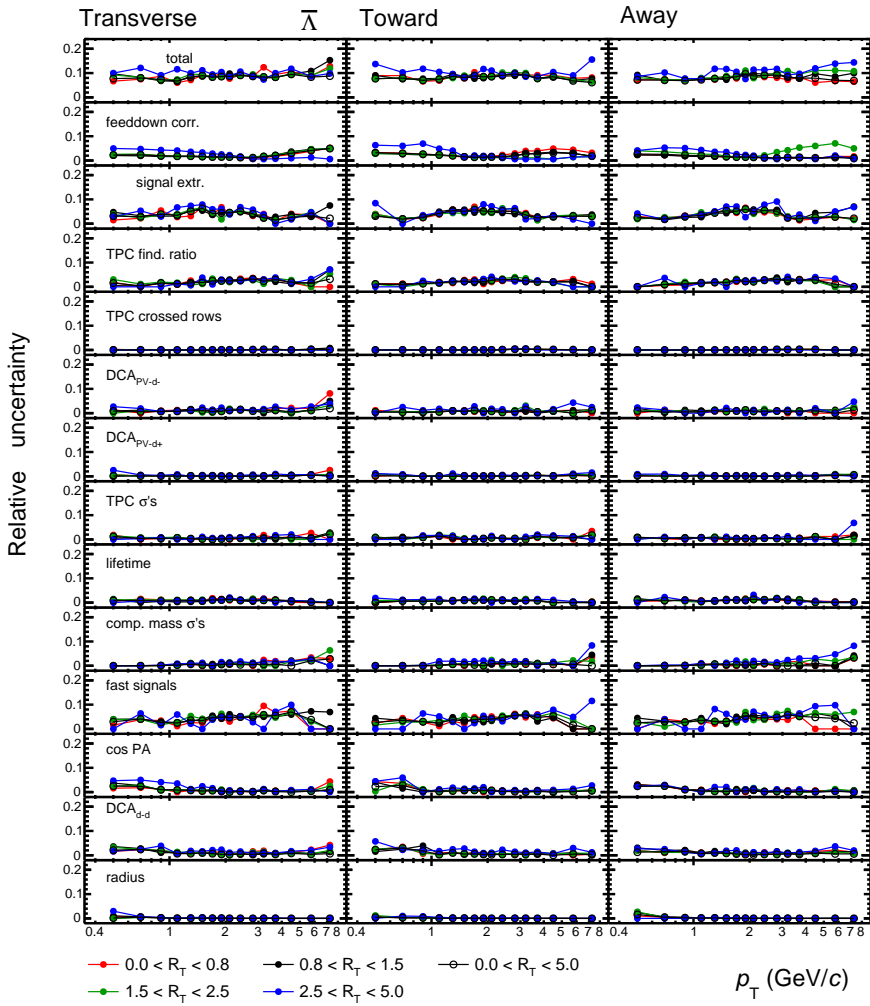
(a)

Figure 8.12: TBA.



(a)

Figure 8.13: TBA.



(a)

**Figure 8.14:** TBA.

### 8.5.1 Uncertainties from the unfolding procedure

*This text needs some editing.*

The deviations between the generated  $p_T$  spectra and the reconstructed, corrected, and unfolded  $p_T$  spectra were used to determine the systematic uncertainties associated with the unfolding procedure. To isolate the effect of unfolding from other

reconstruction effects, the “non-closures” in each  $R_T/R_{T,\min}/R_{T,\max}$  interval were divided by the non-closure in the  $R_T/R_{T,\min}/R_{T,\max}$ -integrated bin.

The unfolding systematic uncertainties exhibited a large amount of correlation between  $K_S^0$  and  $\Lambda$ . This correlation was expected, as the  $V^0$  species should unfold in similar patterns. Therefore, the systematic uncertainty on the baryon-to-meson ratio was also calculated independently to avoid these correlations and reduce the systematic uncertainty on those results.

Moreover, in the most extreme bins, the non-closures sometimes exhibited unrealistic deviations from unity due to limited statistics and fluctuations. To address this issue, a smoothing procedure was applied by fitting the resulting uncertainties with first- and second-order polynomials. The results are shown in Fig. 8.15.

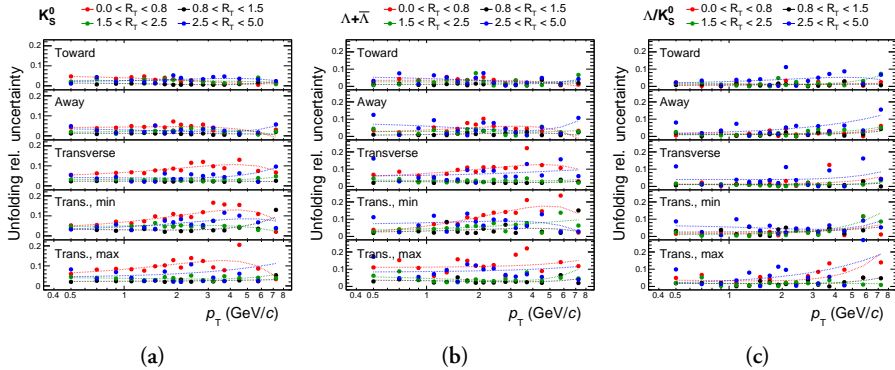


**Figure 8.15:** TBA.

### 8.5.2 Uncorrelated uncertainties

*One paragraph that the treatment and definition of uncorrelated uncertainties with respect to  $R_T$  was done in the same fashion as in the  $S_O^{(p_T=1.0)}$  chapter.*

## 8.6 Description of regions and mean transverse momentum

After unfolding, the average transverse momenta ( $\langle p_T \rangle$ ) of  $K_S^0$  and  $\Lambda$  were studied in the Toward, Away, Transverse, Transverse-min, and Transverse-max regions as a function of  $N_T$ ,  $N_{T,\min}$ , and  $N_{T,\max}$ . To guide the focus of the analysis, according

to MC paradigms as well as previous UE measurements, the following expectations were considered based on the origin of the particles:

1. *Toward and Away regions*: particles from jet fragmentation and underlying event.
2. *Transverse region*: particles from UE, which includes contributions from softer MPIs and harder wide-angle initial- and final-state radiation.
3. *Transverse-min region*: particles from UE, where the softer MPI contribution dominates.
4. *Transverse-max region*: particles from UE biased towards higher amounts of harder ISR/FSR.

The choice of the independent observable is then expected to focus on the effects of:

1. *Toward and Away regions*: for all  $N_T$ ,  $N_{T,\min}$ , and  $N_{T,\max}$ , the relative contributions of UE and jet fragmentation.
2. *Transverse(-min,max) regions*: for  $N_T$ , the magnitude of the inclusive UE, for  $N_{T,\min}$ , the magnitude of the softer-MPIs-enhanced MPI, and for  $N_{T,\max}$ , the magnitude of the harder-ISR/FSR-biased UE.

Fig. 8.16 shows the  $K_S^0 \langle p_T \rangle$  results for different configurations. In the Toward and Away regions, the dependence on  $N_T$ ,  $N_{T,\min}$ , and  $N_{T,\max}$  appears comparable, exhibiting a "jet peak" at low  $N_T$  and a flow-like boost from the underlying event at high  $N_T$  values. In the Transverse, Transverse-min, and Transverse-max regions,  $\langle p_T \rangle$  steeply increases with  $N_T$ , with an ordering in terms of absolute values, although the slopes are similar. These results suggest that the choice of particle region does not have a significant impact on its dynamical properties.

Additionally, the increase in  $\langle p_T \rangle$  with  $N_{T,\max}$  is much steeper in the Transverse-max region compared to the Transverse-min region's increase with  $N_{T,\min}$ , indicating that the choice of independent variable plays the more important role. Together with the choice of particle region, it has the potential to isolate distinct behaviors between the two activity extremes.

Given these findings, this dissertation focuses on the following measurements: Toward/Away/Transverse versus  $R_T(N_T)$ , Transverse-min versus  $R_{T,\min}(N_{T,\min})$ , and Transverse-max versus  $R_{T,\max}(N_{T,\max})$ .

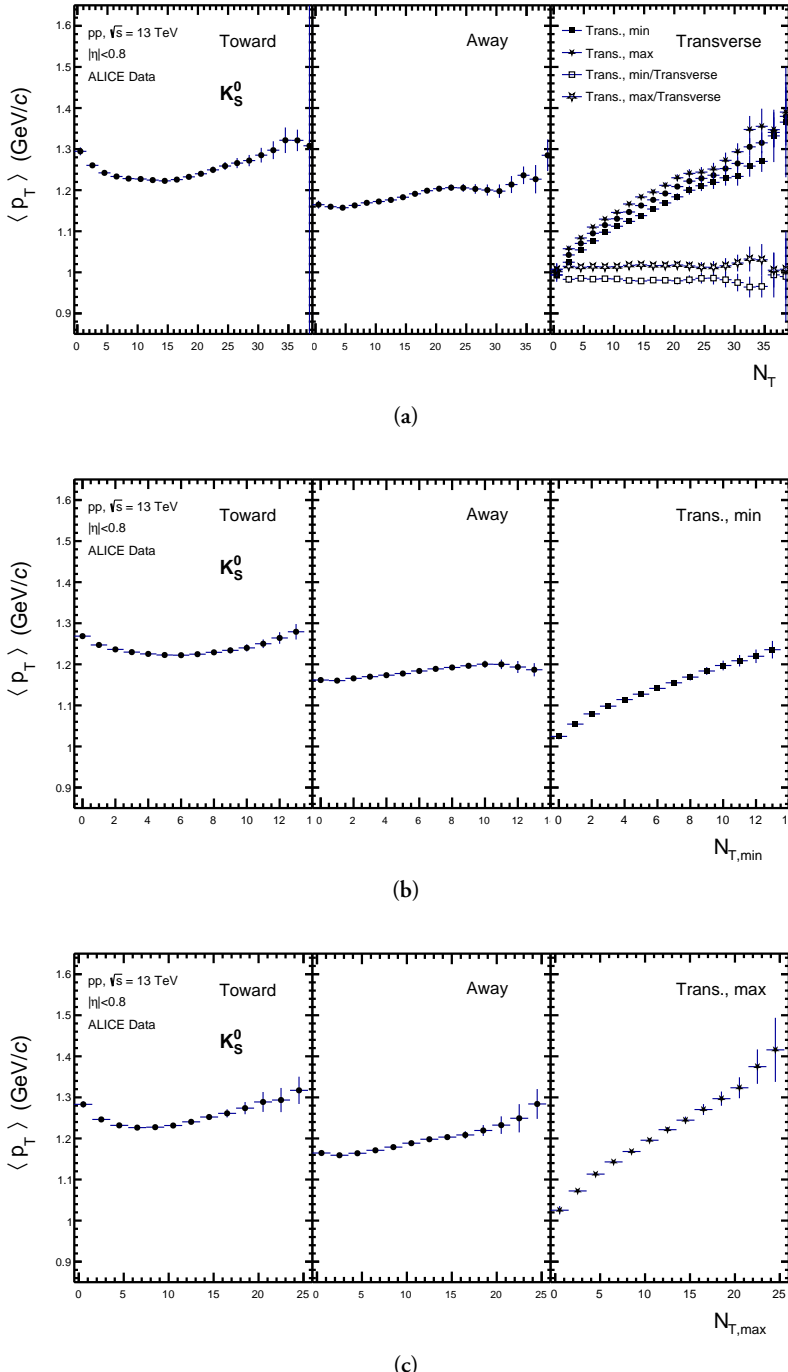


**Figure 8.16:** Mean transverse momentum for  $K_S^0$  as a function of  $N_T$ ,  $N_{T,\min}$ ,  $N_{T,\max}$  in the different azimuthal regions. The x-axis ranges were chosen such that they represent comparable quantiles of the distributions of their variables, to facilitate a more direct comparison. Only statistical uncertainties are presented and biases on  $\langle p_T \rangle$  from the unfolding treatment were not considered.

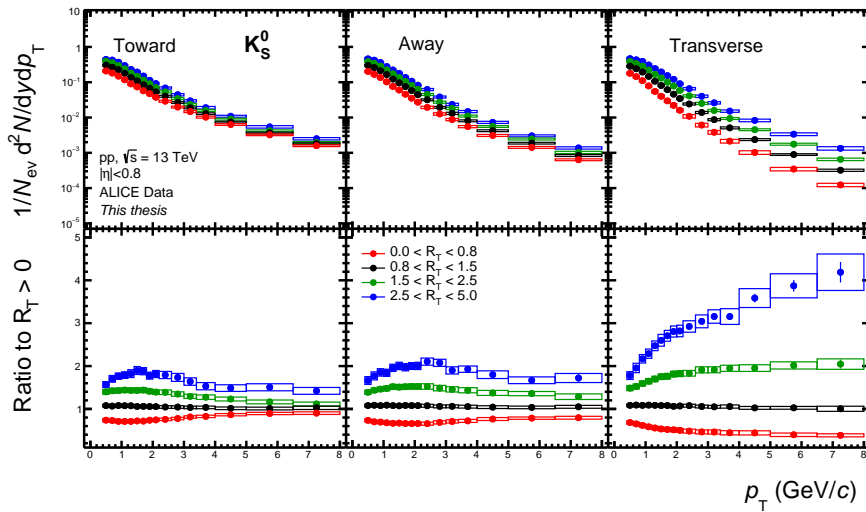
## 8.7 Transverse momentum spectra

The measured  $p_T$  spectra for  $K_S^0$  and  $\Lambda$ , after applying all corrections and accounting for systematic uncertainties, are presented in Fig.8.17 and Fig.8.19, respectively. In addition, these spectra are compared with model predictions in Fig.8.18 and Fig.8.20.

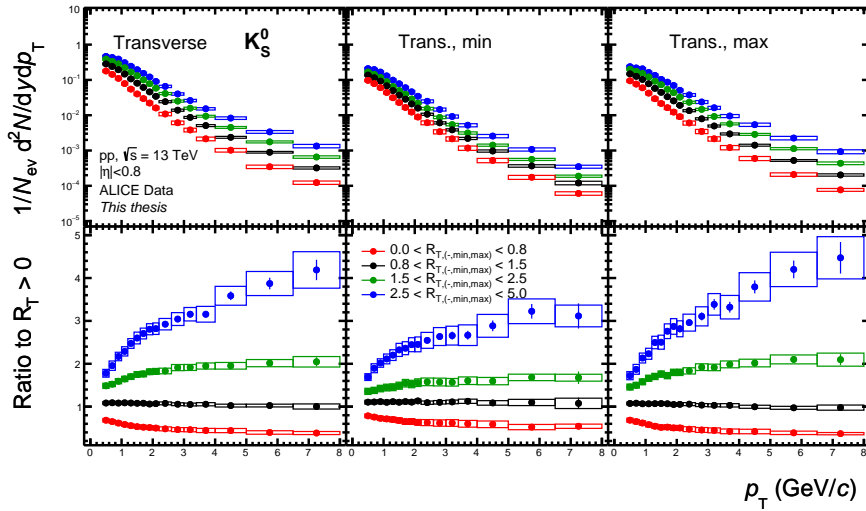
In the Toward and Away regions, there is a dependence at intermediate  $p_T$ , followed by a convergence "to a jet" at high  $p_T$ . This suggests that high-momentum particles solely originating from jets are independent of the UE, as expected. The Transverse region exhibit an increase and hardening with increasing  $R_T$ , indicating that events with higher UE activity are more likely to contain higher- $p_T$  particles. This trend is similar to studies of charged particles at mid-rapidity as a function of  $N_{ch}$  measured at mid-rapidity, where the auto-correlation bias is an important factor in interpretation.

The behavior of the Transverse-max region is similar to that of the Transverse region, indicating the selection of harder wide-angle ISR/FSR. However, the Transverse-min region seems to plateau, suggesting that at higher  $p_T$ ,  $R_{T,min}$  does not impact the particle  $p_T$  spectral shapes.

When compared with MC predictions including Pythia Monash, Pythia Ropes, and EPOS LHC, all models reproduce the data qualitatively very well, although quantitative differences can be noticed. It is also interesting to remember Pythia and Herwig predictions for inclusive charged particles shown in Fig. 8.4, which shows *TBA*.

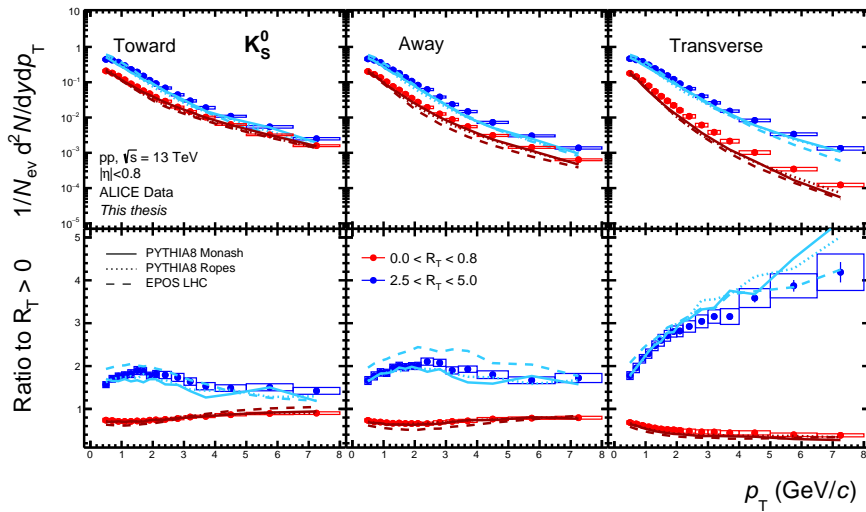


(a)

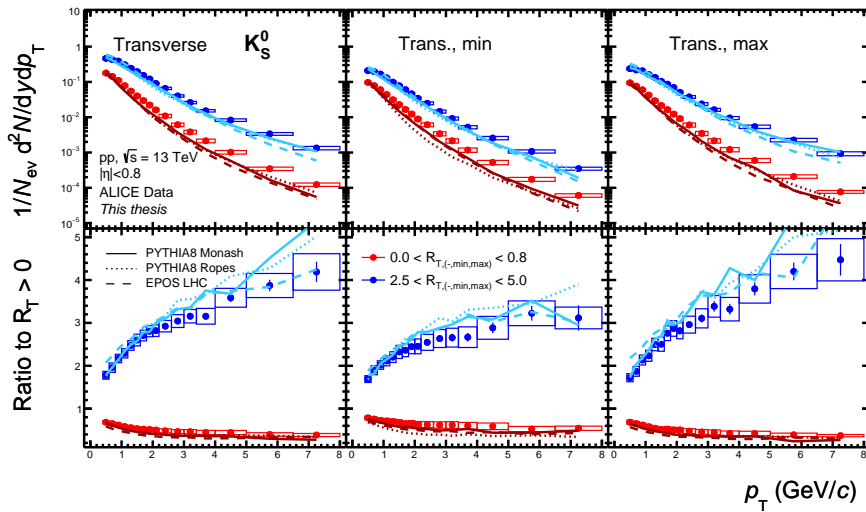


(b)

**Figure 8.17:** The measured and fully corrected  $S_O^{(p_T=1.0)}$  distributions for both (a)  $N_{\text{SPD}_{\text{Trkts}}} 0\text{--}1\%$ , (b)  $0\text{--}10\%$  and (c) VOM  $0\text{--}1\%$ . The curves represent different model prediction, where the shaded area represents the statistical uncertainty of the models.

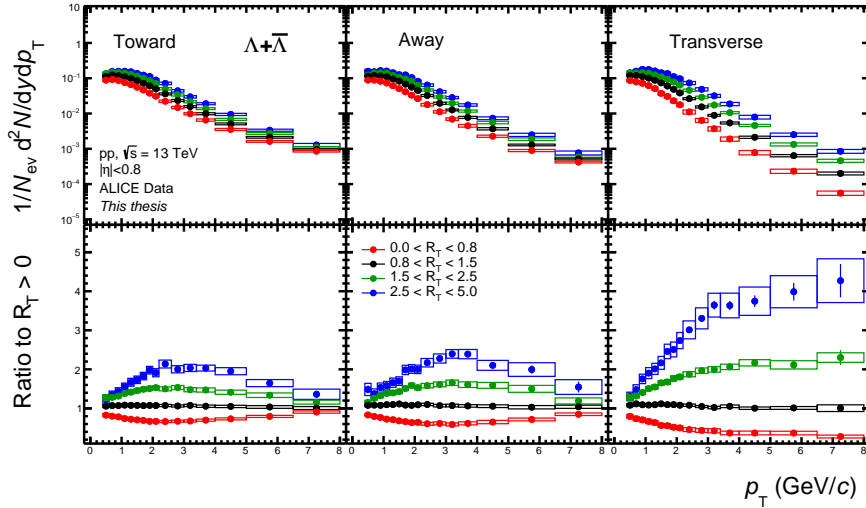


(a)

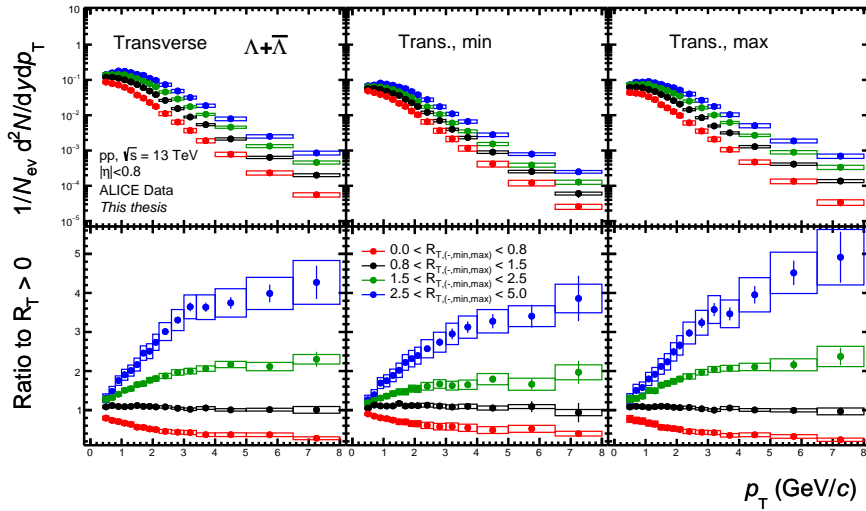


(b)

**Figure 8.18:** The measured and fully corrected  $S_O^{(p_T=1.0)}$  distributions for both (a)  $N_{\text{SPD}_{\text{Trkts}}} 0\text{--}1\%$ , (b)  $0\text{--}10\%$  and (c) VOM  $0\text{--}1\%$ . The curves represent different model prediction, where the shaded area represents the statistical uncertainty of the models.

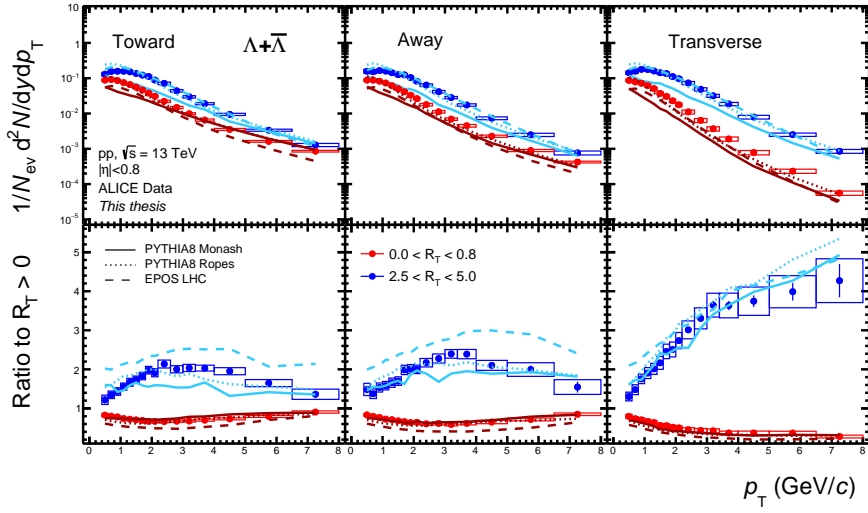


(a)

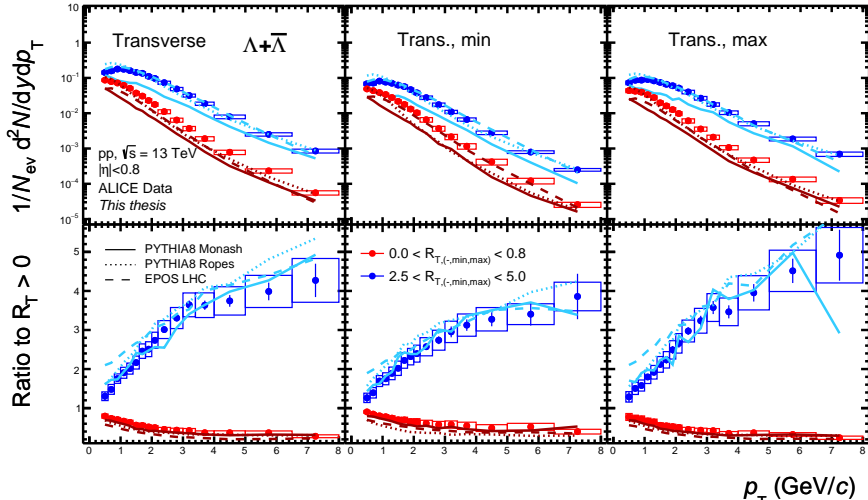


(b)

**Figure 8.19:** The measured and fully corrected  $S_O^{(p_T=1.0)}$  distributions for both (a)  $N_{\text{SPD}_{\text{Trkts}}} 0\text{--}1\%$ , (b)  $0\text{--}10\%$  and (c) VOM  $0\text{--}1\%$ . The curves represent different model prediction, where the shaded area represents the statistical uncertainty of the models.



(a)



(b)

**Figure 8.20:** The measured and fully corrected  $S_O^{(p_T=1.0)}$  distributions for both (a)  $N_{SPD_{Trkts}}$  0–1%, (b) 0–10% and (c) VOM 0–1%. The curves represent different model prediction, where the shaded area represents the statistical uncertainty of the models.

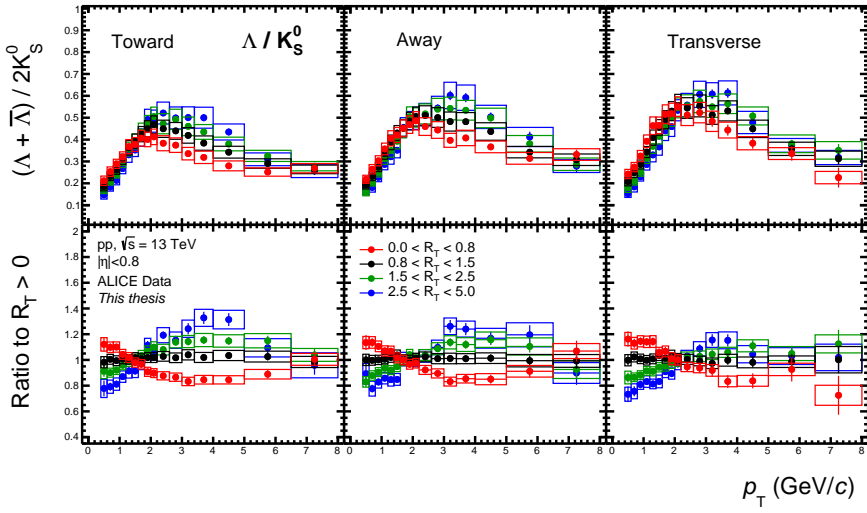
## 8.8 Baryon-to-meson ratio

To investigate the observable most directly linked to radial flow studies, the baryon-to-meson ratios, the  $(\Lambda^0 + \bar{\Lambda}^0)/(2K_s^0)$  results are presented in Fig.8.21, and model predictions are compared in Fig.8.22.

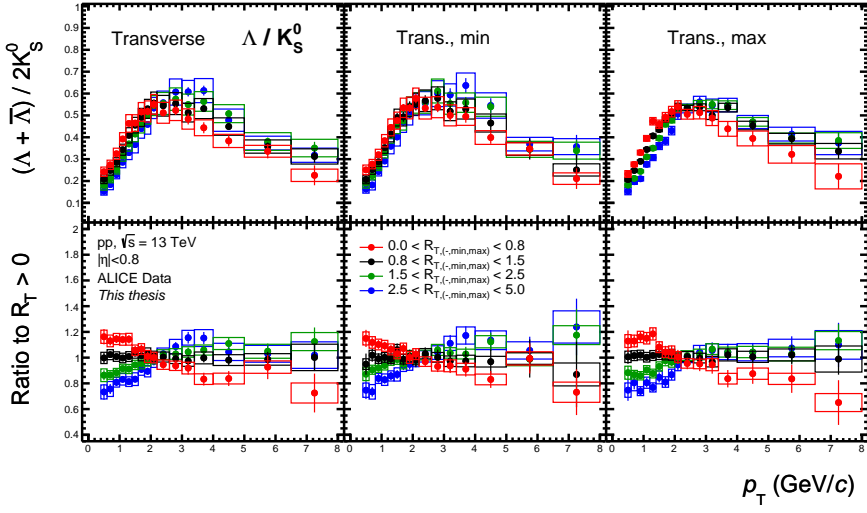
Noteworthily, the biggest dependence on UE activity can be observed in the Toward and Away regions. Although this may not be immediately intuitive, as one may naively expect these regions to be dominated by jets and thus insensitive to softer phenomena like radial flow, there is a somewhat straightforward interpretation. In this region,  $R_T$  controls the amount of interplay between jet-related and UE-related production. Indeed, ALICE measurements of  $(\Lambda^0 + \bar{\Lambda}^0)/(2K_s^0)$  ratios inside reconstructed jet cones and outside of them reveal a drastic difference, further suggesting that the difference in production regime plays a significant role here, rather than flow-like behavior due to increased  $n_{\text{MPI}}$ .

In contrast to the  $S_O^{(p_T=1.0)}$  findings, the Transverse region exhibits typical radial flow patterns: enhancement of the ratio at intermediate  $p_T$ , corresponding depletion at low  $p_T$ , and an overall shift of the peak by about  $1 \text{ GeV}/c$ . The Transverse-min and Transverse-max regions appear to behave very similarly, with small hints of the Transverse-min exhibiting a slightly bigger effect than the Transverse-max, although the results suffer from significant statistical uncertainties. Therefore, more precise measurements are needed to confirm this observation.

Based on the selected models, the Pythia Ropes predictions are the most consistent with the data, whereas EPOS LHC exhibits a much larger dependence on  $R_T$ , and Pythia Monash significantly underestimates the ratios. The latter two models also demonstrate smaller variations of  $(\Lambda^0 + \bar{\Lambda}^0)/(2K_s^0)$  across different regions than the experimental data. Nevertheless, all the model predictions are generally consistent with describing the ratios in the  $R_T$ -integrated case. Overall, these results suggest that mechanisms that account for interactions between MPI, such as the Pythia Ropes model's implementation of increasing tension strength of many overlapping strings, are a step in the right direction.

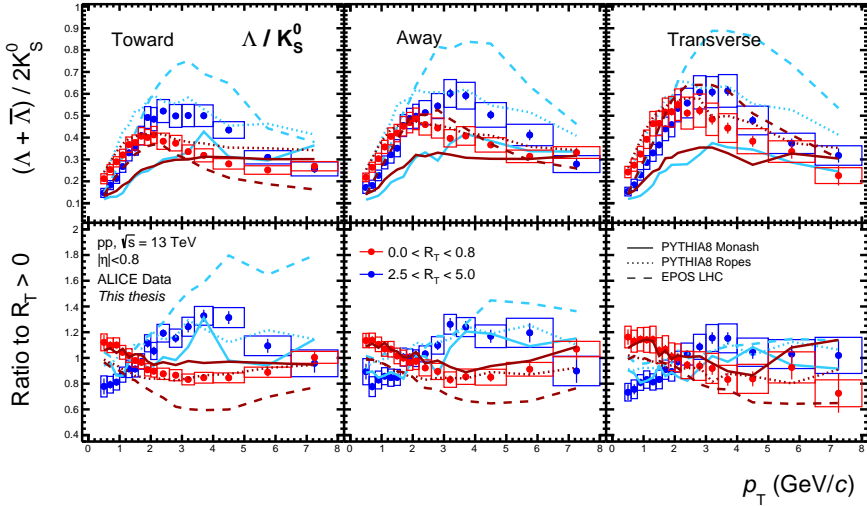


(a)

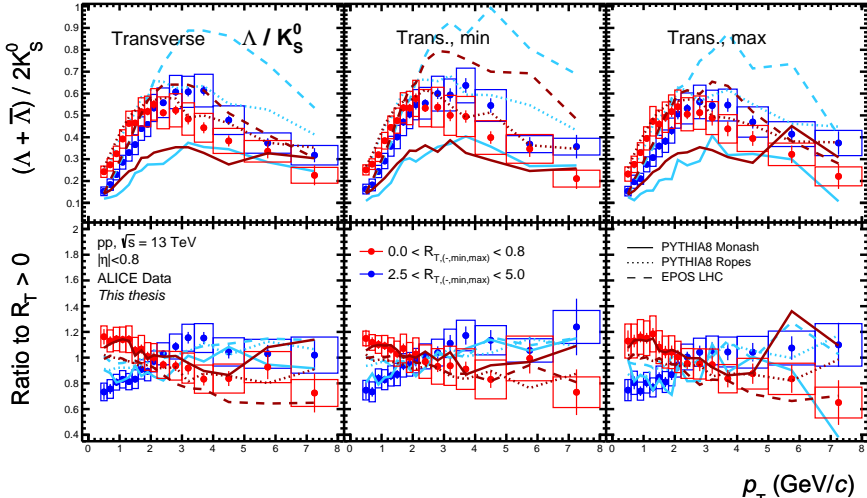


(b)

**Figure 8.21:** The measured and fully corrected  $S_O^{(p_T=1.0)}$  distributions for both (a)  $N_{SPD_{Trkts}} = 0-1\%$ , (b)  $0-10\%$  and (c) VOM  $0-1\%$ . The curves represent different model prediction, where the shaded area represents the statistical uncertainty of the models.



(a)



(b)

**Figure 8.22:** The measured and fully corrected  $S_O^{(p_T=1.0)}$  distributions for both (a)  $N_{SPD_{Trkts}} = 0-1\%$ , (b)  $0-10\%$  and (c) VOM  $0-1\%$ . The curves represent different model prediction, where the shaded area represents the statistical uncertainty of the models.

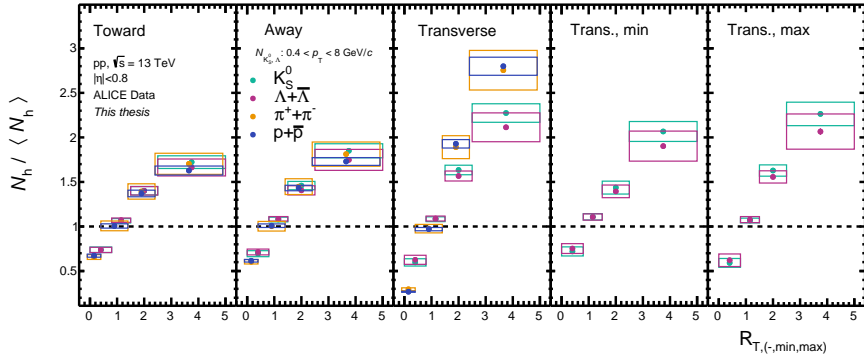
## 8.9 Integrated yields

Finally, in Fig. 8.23, the integrated yields of  $K_S^0$  and  $\Lambda$  are shown as a function of  $R_T$ ,  $R_{T,\min}$ , and  $R_{T,\max}$ . The yields are self-normalised, similar to other multiplicity-dependent particle production measurements by ALICE. Using the same approach as in the  $S_O^{(p_T=1.0)}$  measurement, the reported  $p_T$  range is used to integrate the yields, rather than extrapolating. The yields are then compared to data on pions and protons, as well as model predictions.

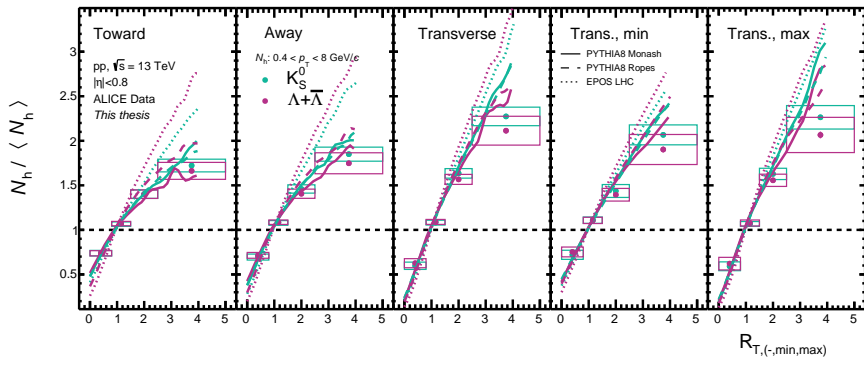
The yields of  $K_S^0$  and  $\Lambda$  increase with  $R_T$ , but at a slower rate than the underlying UE activity (same rate would correspond to  $y = x$ ). The increase of  $\Lambda$  with  $R_T$  appears to be somewhat faster than  $K_S^0$ . The largest increase in yields is observed in the Transverse and Transverse-max regions, with the Transverse-min region showing a slightly slower increase. In the Toward and Away regions, the increase in yields appears to be slower than linear.

When comparing the yields of charged particles, the effect of decoupling the neutral  $K_S^0$  and  $\Lambda$  from the  $N_T$  in the Transverse region is evident. There is also slight, albeit systematic evidence for strangeness enhancement in the Toward and Away regions, with  $K_S^0$  increasing slightly faster than  $\pi$  and  $\Lambda$  slightly faster than  $p$ . However, the uncertainties are significant, and strong conclusions cannot be drawn.

Based on the selected models, Pythia Monash and Pythia Ropes predict values that are consistent with the experimental data. EPOS LHC is also consistent in the Transverse regions but exhibits a faster rise with  $R_T$  than what is observed. In addition, it is less sensitive to the choice of regions compared to the other models.



(a)



(b)

**Figure 8.23:** TBA: Self-normalised yields of  $K_S^0$  and  $\Lambda$  as a function of  $R_T$ ,  $R_{T,\text{min}}$ ,  $R_{T,\text{max}}$  activity (which is also a self-normalised quantity).

## Chapter 9

# Discussion of Results and Conclusions

Lorem ipsum dolor sit amet, consectetuer adipiscing elit. Etiam lobortis facilisis sem. Nullam nec mi et neque pharetra sollicitudin. Praesent imperdiet mi nec ante. Donec ullamcorper, felis non sodales commodo, lectus velit ultrices augue, a dignissim nibh lectus placerat pede. Vivamus nunc nunc, molestie ut, ultricies vel, semper in, velit. Ut porttitor. Praesent in sapien. Lorem ipsum dolor sit amet, consectetuer adipiscing elit. Duis fringilla tristique neque. Sed interdum libero ut metus. Pellentesque placerat. Nam rutrum augue a leo. Morbi sed elit sit amet ante lobortis sollicitudin. Praesent blandit blandit mauris. Praesent lectus tellus, aliquet aliquam, luctus a, egestas a, turpis. Mauris lacinia lorem sit amet ipsum. Nunc quis urna dictum turpis accumsan semper.



# **Part IV**

# **Appendices**



# Appendix A

## List of Acronyms

Lorem ipsum dolor sit amet, consectetuer adipiscing elit. Etiam lobortis facilisis sem. Nullam nec mi et neque pharetra sollicitudin. Praesent imperdiet mi nec ante. Donec ullamcorper, felis non sodales commodo, lectus velit ultrices augue, a dignissim nibh lectus placerat pede. Vivamus nunc nunc, molestie ut, ultricies vel, semper in, velit. Ut porttitor. Praesent in sapien. Lorem ipsum dolor sit amet, consectetuer adipiscing elit. Duis fringilla tristique neque. Sed interdum libero ut metus. Pellentesque placerat. Nam rutrum augue a leo. Morbi sed elit sit amet ante lobortis sollicitudin. Praesent blandit blandit mauris. Praesent lectus tellus, aliquet aliquam, luctus a, egestas a, turpis. Mauris lacinia lorem sit amet ipsum. Nunc quis urna dictum turpis accumsan semper.



## Appendix B

# Mathematical Derivations

Lore ipsum dolor sit amet, consectetuer adipiscing elit. Etiam lobortis facilisis sem. Nullam nec mi et neque pharetra sollicitudin. Praesent imperdiet mi nec ante. Donec ullamcorper, felis non sodales commodo, lectus velit ultrices augue, a dignissim nibh lectus placerat pede. Vivamus nunc nunc, molestie ut, ultricies vel, semper in, velit. Ut porttitor. Praesent in sapien. Lore ipsum dolor sit amet, consectetuer adipiscing elit. Duis fringilla tristique neque. Sed interdum libero ut metus. Pellentesque placerat. Nam rutrum augue a leo. Morbi sed elit sit amet ante lobortis sollicitudin. Praesent blandit blandit mauris. Praesent lectus tellus, aliquet aliquam, luctus a, egestas a, turpis. Mauris lacinia lorem sit amet ipsum. Nunc quis urna dictum turpis accumsan semper.



## Appendix C

# Complementary Material

Lorem ipsum dolor sit amet, consectetuer adipiscing elit. Etiam lobortis facilisis sem. Nullam nec mi et neque pharetra sollicitudin. Praesent imperdiet mi nec ante. Donec ullamcorper, felis non sodales commodo, lectus velit ultrices augue, a dignissim nibh lectus placerat pede. Vivamus nunc nunc, molestie ut, ultricies vel, semper in, velit. Ut porttitor. Praesent in sapien. Lorem ipsum dolor sit amet, consectetuer adipiscing elit. Duis fringilla tristique neque. Sed interdum libero ut metus. Pellentesque placerat. Nam rutrum augue a leo. Morbi sed elit sit amet ante lobortis sollicitudin. Praesent blandit blandit mauris. Praesent lectus tellus, aliquet aliquam, luctus a, egestas a, turpis. Mauris lacinia lorem sit amet ipsum. Nunc quis urna dictum turpis accumsan semper.



## **Appendix D**

# **Scientific Publications**

### **Author contributions**

#### **Paper I: Title paper 1**

I participated in developing the theory and wrote the simulation software. I participated in writing the manuscript.

#### **Paper II: Title paper 2**

I participated in developing the theory and writing simulation software. I participated in writing the manuscript.



# Paper I

S. Doctor and B. someone

An Exact Ewald Summation Method in Theory and Practice

*The Journal of Physical Chemistry A*, 2020, 124(19), pp. 3943-3946

Reproduced with permission from *J. Phys. Chem. A*

Copyright 2020 American Chemical Society.



# Hello, I am an article

Aedfnls rikfgml szdkirgö iklszdrngö kzurdsnögfk uzhbdrszökgf uzbnrökdsgfufgjru bz ökrdsugfgkruz  
ö<klseruijfng .-<jls <rnf.k jxzdbndnrtxökgku özdxnrikögjl dzxr



## Paper II

S. Doctor, B. someone, C. another and D. another

Grand canonical simulations of ions between charged conducting surfaces using exact  
3D Ewald summations

*Physical Chemistry Chemical Physics*, 2020, 22(24), pp. 13659-13665

Reproduced from *Phys. Chem. Chem. Phys.* with permission from the PCCP Owner  
Societies.



# Hello, I am another article

Sergt sdetrfty sdrtgt xtcdhgh dxtrggbs zdrtgt xfdth szdtfgh dxft



# References

- [1] Stewart K. Reed, Oliver J. Lanning, and Paul A. Madden. Electrochemical interface between an ionic liquid and a model metallic electrode. *The Journal of Chemical Physics*, 126(8):084704, 2007. doi: 10.1063/1.2464084.
- [2] ALICE Collaboration. The ALICE definition of primary particles.